**UNIVERSIDADE DE LISBOA**
**FACULDADE DE CIÊNCIAS**
DEPARTAMENTO DE FÍSICA


# Myocardial partial volume correction of internal left ventricular structures in emission tomography images

Mauro Santana Costa e Sousa

*Orientadores*

Dr. Kris Thielemans, Institute of Nuclear Medicine, University College London, London, UK

Prof Dr. Pedro Almeida, Instituto de Biofísica e Engenharia Biomédica, Departamento de Física da Faculdade de Ciências da Universidade de Lisboa, Lisboa, Portugal

MESTRADO INTEGRADO EM ENGENHARIA BIOMÉDICA E BIOFÍSICA

PERFIL: RADIAÇÕES EM DIAGNÓSTICO E TERAPIA

DISSERTAÇÃO

-2016-

**UNIVERSIDADE DE LISBOA**
**FACULDADE DE CIÊNCIAS**
DEPARTAMENTO DE FÍSICA


# Myocardial partial volume correction of internal left ventricular structures in emission tomography images

Mauro Santana Costa e Sousa

Dissertação Orientada por Doutor Kris Thielemans e Professor Doutor Pedro Almeida

Mestrado Integrado em Engenharia Biomédica e Biofísica

Perfil em Radiações em Diagnóstico e Terapia

2016

# *Acknowledgements*

I would like to express my appreciation towards my supervisor, Dr Kris Thielemans, who has been extremely supportive and for recognising the difficulties associated with the completion of this text. I would also like to thank Dr Brian Hutton for the wonderful opportunity of being able to take part of his team at the Institute of Nuclear Medicine, University College London Hospital. My thanks are also extended to my internal dissertation supervisor, Professor Dr Pedro Almeida, for his unconditional support, despite the distance.

My sincere appreciation goes to my colleagues at the Institute of Nuclear Medicine, Débora Salvado, Richard Manber, Hasan Sari, Beverley Holman, Alexandre Bousse, Kjell Erlandsson, Vesna Cuplov and Ottavia Bertolli, who have been always supportive and ready to help. A very especial thanks goes to Cristina Campi, Maria Zuluaga (UCL Centre for Medical Image Computing) for the kind input of their cardiac segmentation methods in this work. I also thank Simon Wan and John Dickson for the very useful discussions and input provided during this project.

I would like to express my special thanks to my fellow colleagues and professors at Institute of Biophysics and Biomedical Engineering, at University of Lisbon: Professor Dr Nuno Matela, Professor Dr Alexandre Andrade, Melissa Botelho, Rui Santos, Danielle Batista, David Soares and Nuno Silva; without whom my academic experience would not have been as rich.

To all the friends I met in London, António Ferreira, João Monteiro, Nino, Dona Maria José & family, Xaverito & family, my colleagues at IXICO and most importantly Sérgio & Lisete, I deeply appreciate all the encouragement towards helping me completing my thesis and all their help during the first months in London.

Last, but definitely not least, my greatest appreciation goes to my family, my mother, my brother, and my soon-to-be wife and son, André. This thesis is dedicated to you all, who sacrificed a lot for me to be able to complete my project and dissertation. For that and for your continuing support, I will be eternally grateful.

# *Resumo*

A imagiologia médica apresenta-se como sendo um conjunto de processos que levam à criação de representações visuais do interior do organismo para análise clínica e/ou auxílio em processos de intervenção médica.

Desde o seu aparecimento e aplicação prática que a imagiologia tem tido um impacto significativo na sociedade, permitindo a confirmação de condições patológicas, possibilitando a avaliação e planeamento de tratamentos, e o fornecimento de uma alternativa a métodos invasivos e, essencialmente, constituindo práticas que permitem o diagnóstico prematuro de patologias. Todos estes aspetos fazem com que a imagiologia médica contribua, em última instância, para a diminuição da taxa de mortalidade e para o aumento da esperança média de vida das populações.

No entanto, apesar dos mais de 100 anos de história desde o aparecimento das primeiras técnicas imagiológicas, existem ainda inúmeros desafios por ultrapassar no campo da imagiologia médica.

Uma das principais motivações é a otimização de processos de diagnóstico em fases prematuras de diagnóstico, o que possibilita um maior leque de ações terapêuticas, podendo fazer a diferença no resultado final do tratamento dos pacientes.

Esta necessidade, aliada ao facto de a maior causa de mortalidade a nível mundial ser devido a doenças cardiovasculares (Allender et al. (2008), Lloyd-Jones (2010)), justifica uma prioridade na investigação de metodologias que visem o diagnóstico de patologias do foro cardíaco num estado em que as ações preventivas e de tratamento permitam uma maior eficácia final para benefício do paciente.

Em particular, as modalidades de imagiologia médica podem distinguir-se entre métodos morfológicos (ou anatómicos) – que visam a obtenção de informação anatómica do organismo -, e métodos funcionais (ou de emissão), que têm por objetivo quantificar, de modo não invasivo, processos fisiológicos e metabólicos ocorrentes no organismo.

Porém, embora este último tipo de métodos apresente uma maior sensibilidade e especificidade na deteção de fenómenos fisiológicos, ao nível molecular, tal surge em detrimento da resolução espacial das imagens. Este fenómeno de degradação da resolução espacial, mais acentuado em imagens funcionais, é conhecido como o efeito do volume parcial. Apesar de ser um tópico sujeito a grande foco de investigação na área imagiológica médica, o efeito do volume parcial não tem, na prática, uma metodologia suficientemente versátil e eficaz de correção.

Os mecanismos de correção do efeito do volume parcial baseiam-se essencialmente na implementação de processos de restauração do desfoque de imagem, havendo uma redistribuição de atividade dos objetos de volta à sua localização original.

Relacionando esta desvantagem associada a imagens de emissão com aplicações cardíacas, é possível alcançar a derradeira motivação à qual este projeto está ancorado. Por um lado, metodologias de correção do efeito to volume parcial necessitam, na sua maioria e de forma a serem mais eficazes, de informação imagiológica funcional e morfológica, correspondentes. É de notar a complexidade associada a este género de processos, uma vez que incorrem num número de diferentes passos de processamento consecutivos, entre eles a segmentação de regiões de interesse, o co registro de imagens funcionais e anatómicas, e implementação do processo de correção propriamente dito, sendo que este pode ser efetuado sob o ponto de vista da imagem final ou durante a reconstrução de projeções tomográficas. Desta forma, é possível definir restrições geométricas que auxiliam no processo de compensação deste efeito.

Por outro lado, o coração possui estruturas intraventriculares, os músculos papilares e as trabéculas, que se caracterizam por serem protrusões das paredes miocárdicas ventriculares, de massa apreciável e que servem o propósito de ancorar as válvulas auriculoventriculares de forma a impedir a regurgitação sanguínea para as aurículas, durante a diástole auricular/sístole ventricular.

A questão em foco é que metodologias de correção do efeito do volume parcial aplicadas ao aparelho cardíaco utilizadas na bibliografia ignoram a atividade produzida por estruturas intraventriculares, considerando-as como pertencentes à "*blood pool"*, que se situa na cavidade ventricular, sendo que este passo é feito de forma a simplificar a rotina de correção, minimizando o número de estruturas cujo efeito do volume parcial se pretende corrigir, tomando apenas em consideração uma parede miocárdica e uma "*blood pool"*, na grande maioria dos casos.

O objetivo do projeto corrente foi a avaliação sobre se a melhor opção residiria na tomada de consideração destas estruturas intraventriculares como fontes independentes produtoras de efeito do volume parcial a um nível significativo, ou se o seu efeito de desfoque seria desprezável ao ponto deste ser mascarado pela atividade da "*blood pool"*.

De forma a testar esta ideia, projetámos um processo lógico dividido em três instâncias de complexidade crescente. A primeira abordagem consistiu num estudo exploratório caracterizado pela modelação de um sistema cardíaco, seguido por um procedimento de desfoque simples do mesmo, através da convolução do modelo com uma função de dispersão típica de um sistema de tomografia por emissão, e posterior avaliação do efeito de volume parcial produzido por estruturas intraventriculares. O objetivo desta abordagem foi o de determinar se o efeito de volume parcial produzido por estruturas intraventriculares seria significativo ou não, sendo que tal foi efetuado por comparação com o efeito correspondente produzido pela "*blood pool"*, referida na literatura como uma estrutura relevante no processo de desfoque imagiológico. Mediante a potencial determinação de que o efeito produzido pelas estruturas internas ventriculares seria efetivamente significativo e tendo em conta as simplificações efetuadas durante a criação do modelo, um estudo mais aprofundado deste efeito justificar-se-ia.

É neste sentido que surge a segunda abordagem ao problema, que consiste no aumento da natureza realística do processo de determinação do efeito de volume parcial produzido pelas estruturas intraventriculares, através da utilização do *STIR* (*Software for Tomographic Image Reconstruction*). O *STIR* é um programa que permite simular o processo de reconstrução de imagens tomográficas, dotando as mesmas de um padrão de desfoque e de ruído realistas. A determinação de uma potencial enfatização do efeito produzido por estruturas internas ventriculares justificaria um ainda maior aprofundamento do estudo deste efeito.

Neste contexto, surge a terceira e última instância deste estudo, que corresponde à levada a cabo de estratégias de correção de efeito do volume parcial propriamente ditas. O principal resultado produzido por este estudo seria a determinação do erro obtido ao recuperar a distribuição de

atividade original do modelo, não tomando em conta as estruturas intraventriculares como fontes independentes produtoras de desfoque, isto é, tomando apenas o miocárdio e a "*blood pool"* como regiões de interesse. O resultado final baseou-se na determinação de que, segundo as simplificações utilizadas na criação do modelo, as estruturas intraventriculares produziriam um efeito local significativo sobre a parede do ventrículo esquerdo, podendo efetivamente mascarar lesões hipo-activas ou adelgaçamentos patológicos da parede do ventrículo, em locais adjacentes à estrutura intraventricular em questão.

É de referir que o presente estudo constitui uma primeira aproximação à avaliação do efeito do volume parcial produzido por estruturas intraventriculares, sendo que até à data, não há conhecimento de um estudo semelhante.

Como conclusão final, e à luz das simplificações adotadas durante a execução deste estudo, não existem indícios que apontem para o facto de estas estruturas não serem relevantes, pelo menos a nível local. No entanto, há que compreender que, de forma a obter uma noção mais completa e precisa sobre a relevância destas estruturas intraventriculares, um estudo adicional terá de ser realizado de forma a comprovar a importância de estruturas internas ventriculares num ambiente clínico, e em particular, se estas devem ou não ser consideradas como independentes.

**Palavras-chave:** Efeito do volume parcial; Correção do efeito do volume parcial; Estruturas internas do ventrículo esquerdo; Músculos papilares

# *Abstract*

**Introduction:** In emission tomography, the system's limited spatial resolution leads to three-dimensional image blurring, a phenomenon called *partial volume effect* (PVE). This limited resolution gives rise to activity spillover between regions in the imaged object, resulting in significant changes in the measured image activity distribution, which is particularly evident in structures with small dimensions. Hence, precise quantification based on image activity values depends on a rigorously implemented partial volume correction (PVC) routine. In nuclear medicine images some PVC methodologies make use of corresponding morphological images in order to provide additional information which assist in the correction procedure. This approach is popular in cardiac emission data. However, in the current PVC literature, cardiac intra-ventricular structures (IVS), namely papillary muscles and *trabeculae carneae*, have been largely ignored, while they may potentially produce a significant influence in terms of activity spillover.

**Methods:** A progressively more complex set of simulation steps were involved in this study to investigate the partial volume effect of IVS. The first step involved the study of a simple blurring model using Matlab, which evolved into a model with a more realistic nature by using STIR (Software for Tomographic Image Reconstruction), which in turn evolved to the evaluation of an actual PVC methodology using C++ and Matlab scripts for PVC. A diastolic right and left ventricle model, designed according to a 17 segment division (Cerqueira et al. (2002)) was constructed, and the PVE originated from the IVS was assessed in all the individual segments of the left ventricle, throughout all the tested approaches. This IVS PVE influence was then compared to the blood pool's (BP) spillover, since the latter is an already well established effect studied in the current literature.

**Results:** The results obtained showed some agreement between the various simulation approaches utilized, showing that the total PVE produced by the overall IVS was comparative to that of the blood pool, but this could still be accounted for in PVC methodologies that do not consider IVS. However, the results consistently pointed to the fact that in local terms the IVS produces an effect that surpasses that of the BP, and PVC methodologies that do not take the IVS into account are not able to adequately recover the initial object's activity distribution, locally.

**Conclusion:** It was shown that the local PVE of the IVS over the left ventricle wall was significant, which can potentially have an effect in terms of masking or over emphasizing anomalous uptakes in regions of the myocardial wall that are in the vicinity of IVS.

# *Contents*

# *Table of Figures*

# *List of Tables*

# *List of Abbreviations*

| | |
|---|---|
| AHA | American Heart Association |
| APD | Avalanche photodiode |
| BGO | Bismuth Germanate |
| BP | Blood Pool |
| CM | Count Magnitude |
| CSF | Cerebrospinal Fluid |
| CT | Computed Tomography |
| CTA | Computed Tomography Angiography |
| DICOM | Digital Imaging and Communications in Medicine |
| ECG | Electrocardiography |
| FBP | Filtered Back-Projection |
| FDG | Fludeoxyglucose |
| FOV | Field of View |
| FT | Fourier Transform |
| FWHM | Full Width at Half Maximum |
| GE | General Electric |
| GM | Grey Matter |
| GTM | Geometric Transfer Matrix |
| IVS | Intraventricular Structure |
| iY | Iterative Yang |
| LOR | Line of Response |
| LSO | Lutetium Oxyorthosilicate |
| LV | Left Ventricle |
| MG | Muller-Gartner |
| MLEM | Maximum Likelihood Expectation Maximization |
| MRI | Magnetic Resonance Imaging |
| MTC | Multi-target Correction |
| OSEM | Ordered Subsets Expectation Maximization |
| PET | Positron Emission Tomography |
| PM | Papillary Muscle |
| PSF | Point Spread Function |
| PVC | Partial Volume Correction |
| PVE | Partial Volume Effect |
| RBV | Region Based Voxel-wise |
| RC | Recovery Coefficient |
| ROI | Region-of- Interest |
| RV | Right Ventricle |
| SNR | Signal-to-noise Ratio |
| SPECT | Single Photon Emission Computed Tomography |
| STIR | Software for Tomographic Image Reconstruction |
| SUV | Standard Uptake Value |
| TC | *Trabeculae Carneae* |

| | |
|---|---|
| TOR | Tube of Response |
| WM | White Matter |

# 1.*Introduction*

## 1.1. Project Framework

This dissertation was submitted for the purpose of fulfilling my Master's Degree in Biomedical Engineering and Biophysics – profile in Radiation in Diagnosis and Therapy, at the Faculty of Sciences of the University of Lisbon (FCUL).

The project that led to the writing of the thesis was performed under the scope of the LLP/Erasmus Programme, a European Union (EU) student mobility scheme that provides foreign exchange learning and internship options for EU students. The project was a collaboration between the Institute of Nuclear Medicine (INM), University College London (UCL), London, United Kingdom (UK), and the Institute of Biophysics and Biomedical Engineering (IBEB), FCUL, Lisbon, Portugal.

IBEB focuses on research and post-graduate teaching functions. In addition to Masters and PhD project supervision, IBEB has founded a BSc+MSc programme in Biomedical Engineering and Biophysics. The main research areas at the institute are distributed along 4 main thematic lines: Medical Imaging and Diagnosis; Brain Stimulation and Rehabilitation; Brain Dynamics and Connectivity and Cancer Therapy and Drug Delivery.

Regarding the Research Physics Group at INM, it mainly focuses on Medical Physics applied to Nuclear Medicine and Molecular Imaging. The research projects under way at the institute fall essentially under the scope of emission tomography. The areas of interest are optimized tomographic reconstruction for PET (Positron Emission Tomography) and SPECT (Single Photon Emission Tomography), motion and partial volume image corrections, and multi-modality image analysis applied to clinical research studies in Nuclear Medicine, in particular using combined PET-CT (PET coupled with Computed Tomography), SPECT-CT and PET-MRI (PET coupled with Magnetic Resonance Imaging).

This project consisted in assessing the partial volume effect (PVE) influence of internal ventricular structures (IVS) over the left ventricle wall, in order to ultimately ascertain whether these structures should be taken into account in Partial Volume Correction (PVC) methodologies applied to emission tomography, and in particular to PET. The thesis was performed under the external supervision of Dr Kris Thielemans, Senior Lecturer at UCL, and Professor Brian Hutton, Chair of Medical Physics in Nuclear Medicine and Molecular Imaging Science. The internal supervision role belonged to Professor Pedro Almeida, Director of IBEB and Associate Professor at FCUL.

## 1.2. Motivation

The Partial Volume Effect (PVE) consists in one of the main sources of biases in emission tomography imaging, particularly in cardiac applications. PVE is due to limited spatial resolution, and results in image quality degradation through blurring, hence affecting quantification accuracy. Spatial resolution is affected by the scanner resolution, object geometry, motion, voxel sampling and positron range, which further increase the PVE.

Therefore, PVC methodologies become necessary, especially in cardiac applications (Iida et al., 1991), where motion artefacts and temporally dynamic cardiac geometry may lead to incorrect clinical evaluations of myocardial perfusion (assessed mainly by $^{82}$Rb-chloride) and viability images (based on the glucose metabolism – $^{18}$F-FDG), by potentially masking myocardial abnormalities.

Some PVC methods require the usage of anatomical priors, which provide high spatial frequency information, used for stabilisation purposes in PVC algorithms. In these cases the anatomical information is often used in the form of regions of interest (ROIs) segmented from morphological images acquired from modalities such as MR and CT.

However, the current segmentation practice standards recommend to consider cardiac internal ventricular structures (IVS) as part of the ventricle cavity, instead of independent ROIs, contouring only the myocardial wall and not including these muscular protrusions. This is done in order to make segmentation practices more reproducible (see e.g. Cerqueira et al. (2002), Petitjean et al. (2011)). By not considering the IVS as independent structures, and hence by not considering their activity spillover on adjacent structures, potential masking of hypo-perfusion defects in near locations in the ventricle wall may occur.

A study regarding IVS influence in terms of PVE has never been performed to the best of our knowledge. The aim of this project was therefore to assess the IVS influence over the LV wall in terms of PVE, in order to ultimately ascertain whether IVS should be taken into account in PVC methodologies or not.

### 1.2.1. Layout of the Report

This report is divided in 7 Chapters.

Chapter 1 comprises the Introduction of the report, describing the main motivations that led to the execution of this project, as well as the general layout of the work to be presented.

Chapter 2 provides with information regarding the basic principles necessary to introduce the topics addressed in this study. The chapter starts by describing the basic PET principles, including the physical principle, data correction and image reconstruction, followed by a brief description of cardiac anatomy features, necessary to understand the specialized application of the studied PVE in the cardiac apparatus.

The history and overview of PVC methods is presented in Chapter 3, which is further subdivided into a selection of general PVC techniques section (section 3.1) and more specific cardiac applied and non-cardiac applied PVC approaches part (sections 3.2 and 3.3), often making adaptive use of PVC techniques presented in the previous sub-chapter (section 3.1). This main section

comprises a bibliographic review of all the major approaches explored in the context of cardiac PVC.

Chapter 4 comprises the Methods, and is further subdivided into four distinct parts. Section 4.1 describes the simple blurring approach in determining the PVE of IVS over the LV wall, in a created 3D model of the ventricular heart. Section 4.2 describes the possibility of exploring a slightly different research path, where the possibility of assessing the PVE on cardiac dog data was evaluated. Section 4.3 provides the description of the work planned in order to determine the influence of the IVS in terms of PVE using a more realistic approach, by the incorporation of typical reconstruction biases obtained with the usage of Software for Tomographic Image Reconstruction (*STIR*). Section 4.4 describes the implementation of PVC routines on the previously created model, which is the step in which this study culminated.

Chapter 5 (Results and Discussion) encompasses the outputs from the three main study levels, as well as relevant observations regarding these. Following a brief overview (section 5.1), sub-section 5.2 depicts the main findings of the simple blurring procedure. In sub-section 5.3 the results from the evaluation of using cardiac dog data were described. Sub-section 5.4 portrays the results from each step of the more realistic *STIR* approach, describing how the enhancing of the realistic nature of the model occurred, as well as the model validation and main quantification results. Section 5.5 provided with an overview of the main results obtained from the PVC implementation phase, including the evaluation of two available cardiac segmentation techniques.

Chapter 6 (Summary, Conclusions and Future Prospects) provides with the overall outcome of the study, which corresponded to the affirmation that the IVS present with a significant impact in terms of local blurring over the LV wall. A set of possible future study paths were defined, describing research possibilities that could potentially provide with an even more accurate assessment of IVS PVE importance, when selecting the most appropriate segmentation method to precede the PVC process.

Finally, Chapter 7 aims to inform about the impact of the study in terms of a resulting scientific conference oral presentation, as well as internal (INM-UCL) oral presentations.

The study's references can be found in section 8.

# 2.*Background*

## 2.1. Positron Emission Tomography

Positron emission tomography (PET) is a nuclear medicine imaging technique that is used to quantify physiological and biochemical processes *in vivo*. This technique is based on the labelling of radioisotopes, which is the main characterizing aspect of functional imaging. In this nuclear medicine technique the bio-distribution and kinetics of the labelled biomolecules are acquired in the form of images, through the detection of radioactive decay. This section will be dedicated to describing the background PET related concepts necessary to the execution of this work.

### 2.1.1. Basic PET Principles

The tracer principle is used to measure the physiological and biochemical processes of a single molecule in vivo, stating that a radioactive sample takes part in a metabolic reaction in a similar way as its non-radioactive correspondent. Therefore, PET is based on the labelling of biological molecules with positron emission radionuclides, administered to the patient before the imaging session, allowing for the measurement of the concentration of the radiotracer during a specific time period.

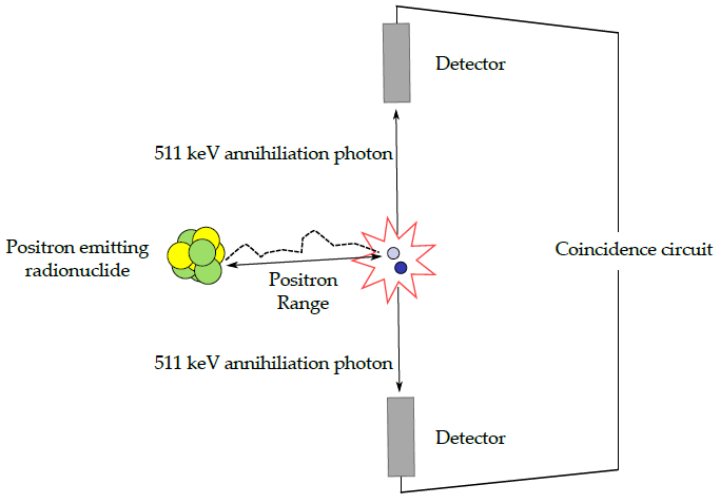


***Figure 2.1*** *- PET imaging principle: positron-electron annihilation and subsequent emission of two 511 keV photons in opposite directions, and respective photon coincidence detection by PET detectors (Weirich & Herzehog, 2012)*

The PET images are obtained based on the coincidence detection of the two annihilation-based photons that are produced following the same positron decay (Fig. 2.1). The process of positron decay is based on the emission of a positron particle ($\beta^+$) from a positron emission isotope. The emitted anti-particle travels for a small distance, typically in the millimetre range (positron range), before interacting with an electron from the surrounding environment, which leads to an annihilation reaction. The product of this interaction is the conversion of the mass of the positron-electron pair in two photons of $511\ keV$, emitted in opposite directions ($180^\circ$). The criteria to accept the coincidence detection as a legitimate emission from the radioisotope in study involve a defined energy window around the $511\ keV$ energy band and a defined time-window as well (e.g. $6\ ns$), in order for the so-called prompt event to be recorded. The PET components that allow for the coincidence event detection are detectors consisting in scintillation crystals (essentially lutetium oxyorthosilicate (LSO) or bismuth germanate (BGO)), which convert the $511\ keV$ photons into visible light. These crystals are coupled to an electric system which function lies in signal amplification - a photomultiplier (PMT) or an avalanche photodiode (APD) for example - which is followed by an analogue/digital converter at the end of the coincidence detection system (Fig. 2.1). Each coincidence event is associated with a line of response (LOR) or tube of response (TOR), which depends on the reconstruction model utilized (2D or 3D, respectively), coupling the two detectors reached by the two $511\ keV$ photons. The obtainment of an image is attained thanks to the reconstruction algorithm that makes use of the information provided by these LORs or TORs.

However, the detection system is not perfect, as it allows for a range of detection events that are not true, as illustrated in Fig. 2.2.

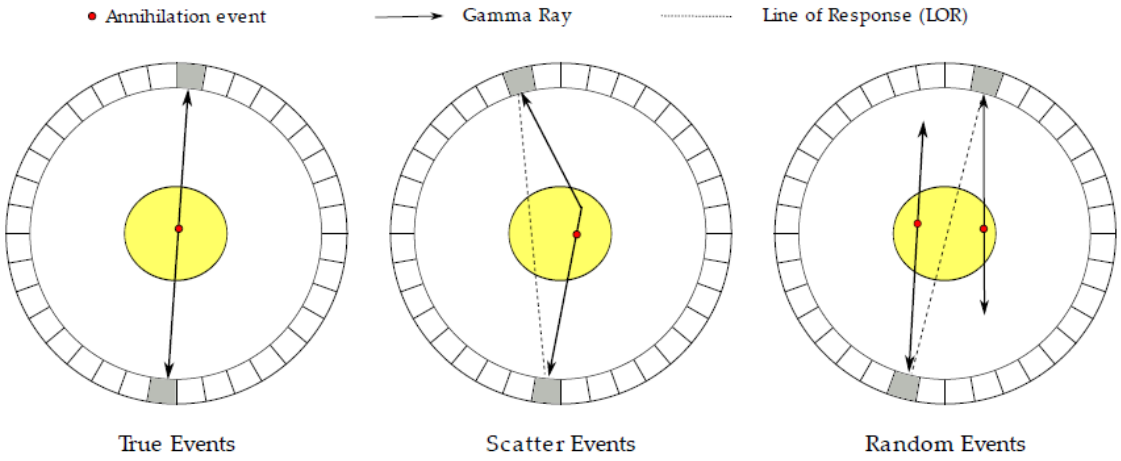


***Figure 2.2*** *- Different types of coincidences: Left) True event; Centre) Scatter event; Right) Random event (Weirich & Herzehog, 2012)*

Random and scattered coincidences may be detected due to the possibility of one of the photons from the annihilation pair to escape the field of view (FOV) of the PET scanner, or due to the attenuation of photons within the imaging object's volume. The scatter event detections are due to the interaction between at least one photon from the annihilation pair and matter, and these interactions essentially occur in the form of the Compton Effect, inducing changes in the direction of the photon prior to its detection. On the other hand, random events occur when photons from two different annihilation events are detected within the same coincidence window, whilst the other photons from each of the two separate annihilations are not detected. This occurrence is also depicted in Fig. 2.2. Both random and scatter events lead to the generation of an incorrect LOR or TOR, which ultimately contribute to image quality degradation. In addition to the increase in the number of apparent counts in the image due to these incorrect event detections, the PET signal can also experience a decrease due to scattered photons that are not detected, either because they

are emitted in a direction that is not captured by the detectors, or because their energy is reduced below the acceptable imposed limits.

Therefore, an accurate quantification of the tracer distribution in terms of space and time is proportional to the amount of true coincidences detected in the signal, which justifies the need for the correction of a plurality of factors, in order to allow for the decrease in the amount of random/scatter events or to the amplification of true PET signals. These correction methodologies shall be enumerated in the next section (**2.1.2**). For further information regarding PET principles that fall outside of the scope of this work, other sources can be consulted (Weirich & Herzehog, 2012).

## 2.1.2. Data Correction

Data correction is an imperative process towards obtaining accurate quantitative and qualitative PET data.

The main reasons to implement correction routines are related to intrinsic characteristics of the scanner and consequences of the interaction of photons with matter. Scanner characteristics that need compensation routines are related to detector efficiency correction, dead time correction, normalization and, mainly, partial volume correction. Photon interaction related compensation methods encompass essentially scatter, attenuation and random events correction. A different aspect that requires correction routines is regarding patient related discrepancies, which encompass essentially motion during the scan. In this section the focus was on the correction methods that would provide with a more significant impact in terms of image reconstruction and quantification: attenuation, scatter, randoms and partial volume corrections. Although motion is also an important effect that produces influence over image quality, motion correction was chosen to be left out of the scope of this work since all the quantification processes within this study were performed on a motionless model, hence causing motion correction methodologies to fall outside of the scope of this report.

### 2.1.2.1. Attenuation Correction

Attenuation correction is one of the correction routines that produce significant visual and quantitative effects (Fig. 3). This compensation routine is of noteworthy importance in nuclear cardiac applications, as it serves as a critical mechanism towards improved diagnostic accuracy (Hendel et al., 2002).

Photons that travel through matter suffer attenuation effects, mainly in the form of Compton scattering, losing their energy in the process. For simplification purposes, if one considers a monoenergetic photon beam entering a uniform target with length $\boldsymbol{x}$, the beam will be attenuated exponentially according to the known relation:

$$N(x) = N_0 e^{-\mu x}, \qquad \textbf{(Equation 2.1)}$$

where the $N_0$ is the original number of photons in the beam and $\mu$ is the linear attenuation coefficient of the medium, which is dependent on the photon's energy.

An essential aspect of the attenuation correction routine is the obtainment of the attenuation map of the imaging object. In order to derive this, the current standardized approach involves the acquisition of a transmission image, acquired under different methodologies according to the specific scanner's characteristics. In standalone PET machines the acquisition of transmission images is performed using rotating sources with high half-life positron emitters ($^{68}Ge - {}^{68}Ga$) (Dahlbom and Hoffman, 1987) or single photon emitters ($^{137}$Cs) (de Kemp and Nahmias, 1994). However, standalone PET systems are currently no longer operating in the market, as the most common current set-up used in clinical and research environments are PET-CT systems. In these scanners the transmission image is provided by the CT component. The process that leads to the obtainment of the attenuation map consists in having the transmission image go through a series of post-processing steps that involve, essentially, the application of a scaling factor (either linear or not) (Carney et al., 2006) and a post-filtering Gaussian smoothing step. The scaling step is only applicable when the transmission image is not acquired using a positron emission source (which is the case in CT). The Gaussian filtering is uniquely applied to transmission images obtained via CT imaging, and is required in order to perform a resolution matching between the high resolution CT and lower resolution PET. In the case of the promising PET-MR systems, no rotation source or CT system is available, which presents with an implementation difficulty that justifies the fact that MR based attenuation map generation is still an active field of research in PET-MRI. For further information on MR based attenuation correction other publications can be consulted (Ay and Sarkar, 2007), (Keereman et al., 2012).

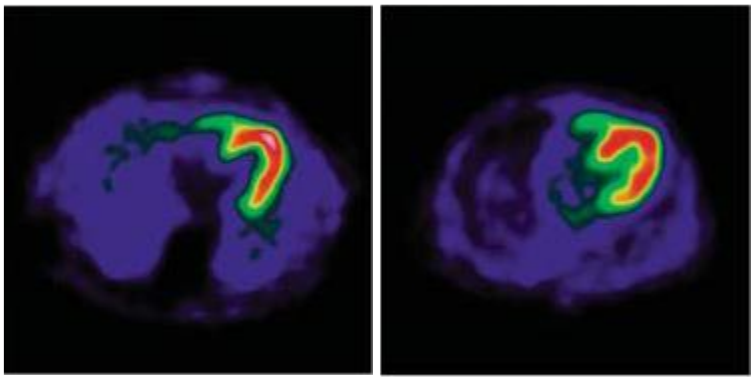

***Figure 2.3*** *- Left) $^{82}$Rb-chloride myocardial perfusion study with no attenuation correction; Right) Corresponding study with attenuation compensation (Di Carlie & Lipton, 2007)*

### 2.1.2.2. Scatter Correction

Similarly to attenuation correction, scatter compensation methodologies also have a significant visual and quantitative impact on images (Fig. 2.4). However, whilst attenuation is characterized by an exponential decrease in the signal intensity, scatter is known to add blur to the image, hence deteriorating its contrast and spatial resolution. The reported scatter contribution for a 2D acquisition mode, evaluated in different scanner designs, varies from 10% to over 40%, and it is not possible to assign an exact scatter contribution due to the complex dependence of this factor on the patient (Paans et al. 1989). Different compensation methods have been developed, such as photon energy restriction or numerical calculations based strategies (Zaidi and Montandon, 2007). A common algorithm used in scatter correction methodologies involves the usage of the attenuation map and reconstructed image to compute a numerical simulation of the distribution of scatter, in terms of each LOT/TOR. Once the simulation is finalised, a scaling of the scatter

distribution to the reconstructed data needs to be performed. The scaling procedure starts with the assumption that the events detected outside of the imaging object's volume (attenuation map) are merely scattered events after a random correction routine is applied, also known as scatter tails. Using these scatter tails originated from the simulation and data reconstruction it is possible to scale the scatter distribution (Monteiro, 2012). Once the scaling is complete, the scatter distribution is available for scatter correction use. More details on scatter correction methodologies can be found elsewhere (Zaidi and Koraly, 2006).

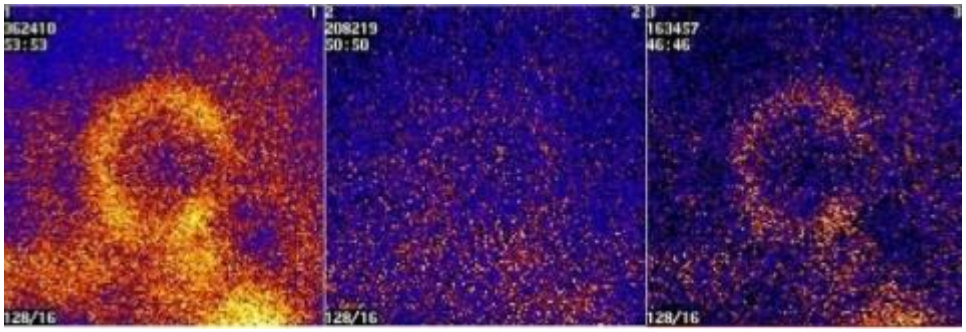

***Figure 2.4*** *- Left) Non-corrected (raw) Rb-82 cardiac image; Centre) Corresponding scatter map; Right) Scatter corrected image (de Kemp and Nahmias, 1994)*

### 2.1.2.3. Correction of Random Events

The accountability of random events leads to an improper increase in the PET signal, hence contributing negatively to image contrast.

The amount of random events can be accounted for in terms of the rate of random detections $R$, calculated across a temporal window $\tau$ in terms of a pair of detectors $i$ and $j$, according to the following relationship:

$$R = 2\tau R_i R_j, \quad \textbf{(Equation 2.2)}$$

where $R_i$ and $R_j$ present with the rates of single events identified by detectors $i$ and $j$, respectively. It is worth noting that the random coincidence rate increases with the square of the activity and the true coincidence rate increases linearly. Two methods are generally considered when formulating random events correction routines, one using measurements of the single rates and using Equation 2, the other consisting in a real-time subtraction of delayed coincidence channel where one of the single-photon events has an arbitrary large time delay, the latter one being called delayed time window method. This approach has the intrinsic assumption that the probability of detection of a true or scattered event in a delayed time window is null. Taking into account that coincidence events are detected in a well-defined temporal window (e.g. 6 $ns$), in the event where a delayed time window with the same duration and a delay of 60 $ns$, for example, is considered, the latest window will only measure the random events. Since both the time windows have the same width (6 $ns$) the rate of random detections should be the same in both windows. Subsequently, the rate measured with the shifted window can be used in order to correct for the bias caused by the random events. This provides an accurate correction for random coincidences, but also increases statistical noise in the net coincidence sinograms. In other words, the estimate of random coincidences is noisy and correcting for random coincidences by subtracting a noisy

image increases the noise in the net coincidence sinograms. For further information on random correction strategies, consult (Brasse et al., 2005).

### 2.1.2.4. Partial Volume Effect and Partial Volume Correction

In emission tomography, PVE refers to a series of phenomena that result in three-dimensional (3D) image blurring. Quantitatively, PVE consists in count/activity spillover between different regions in an image. The blurring is usually modelled as a convolution operation between the true count distribution in the imaging object and the point spread function (PSF) of the imaging system, generally modelled as a Gaussian function. The blurring yields an activity decrease in regions where the count density is higher, and produces an opposite effect in adjacent areas of lower count concentration. Fig. 2.5 illustrates this effect in a two-dimensional (2D) framework.

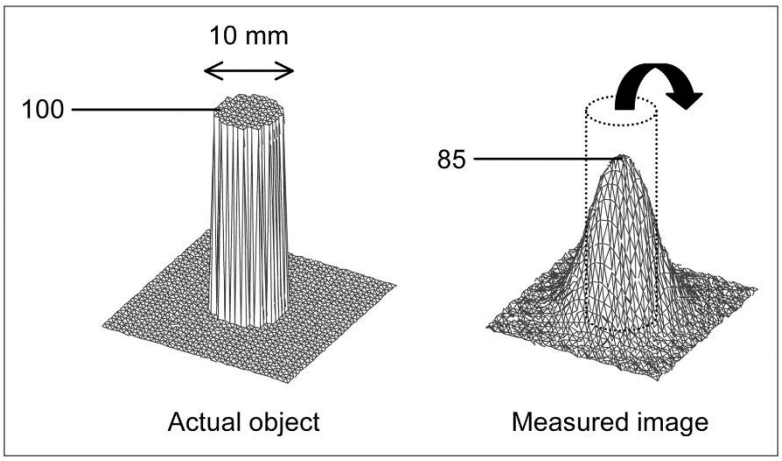


***Figure 2.5** - Illustration of the PVE phenomenon (Soret et al. 2006)*

Fig. 2.5 illustrates that after the convolution operation, counts are removed from their original location of interest - i.e. count spill-out from a region occurs - and are relocated to nearby image regions - i.e. count spill-in to adjacent regions.

The PVE is dependent on the system's spatial resolution – so that the worse the spatial resolution is, the more intense the PVE; the imaging object's geometry – so that the smaller the dimensions of the object are, the more intense the PVE; and the size of the voxels – so that the larger the voxels are, the more intense the PVE. PVE is also dependent on scanning system type – SPECT or PET; motion – mainly due to biological organ activity's cycles; and positron range – particularly significant in PET $^{82}$Rb protocols, due to the relatively high positron range, referenced as 2.6 mm root mean square (Yoshinaga et al. 2010).

It is estimated that PVE affects structures which spatial extent is smaller than 2.5 to 3 times the full width at half maximum (FWHM) of the scanner's PSF (Soret et al. 2006), (Zaidi et al. 2006). The different amount of PVE associated with different object sizes is one of the main problems produced by this effect. Smaller structures undergo a more intensive spill-out effect, which represents a more significant decrease in those structures' apparent activity. On the other hand, larger structures have a lesser PVE related variability in their apparent activity values. In any case, this introduces a bias that consists in apparent changes of activity due to object size variation

across time (e.g. myocardial thickness variation during the cardiac cycle), while the actual activity concentration is not expected to change (e.g. between systole and diastole).

PVE is also related to the size of pixels or voxels present in an imaging matrix, so that the bigger the size of the voxels, the greater the extension of structure overlap on the same voxel in terms of activity mixture from different objects. This is known as the sampling or tissue fraction effect (Erlandsson et al. 2012), (Iida et al., 1991).

In nuclear medicine, namely in PET and SPECT, the PVE is of particular importance since the PSF, or, in other terms, the spatial resolution, is notably limited compared to current anatomical imaging approaches, such CT and MRI. Therefore, concise and effective PVC strategies are needed in order to correctly recover the 3D activity distribution of a tracer in the organism.

In a fairly general way, PVC techniques can be understood as attempts to reverse the effect of the system's limited spatial resolution, either in the image or projection domain (post-reconstruction or reconstruction approaches, respectively). The principal applications of PVC consist in improving the accuracy of quantitative studies and correcting for resolution blur.

A method to recover the original image activity distribution is by deconvolving the acquired image with the system's PSF, hence undoing the convolution that lead to the blurred image. However, this procedure is inherently ill-posed, since the deconvolution is applied to an image that, besides the original convolution step, has been affected by noise of different types, in different stages of the image acquisition and reconstruction procedures, making the solution unstable (Kabanikhin et al. 2008). Simplifications often adopted in the modelling of the PSF, namely spatial-invariance or symmetry, further contribute to the ill-posedness of the deconvolution process. In order to introduce some degree of regularization to avoid high-frequency noise amplification, anatomical information and activity distribution homogeneity assumptions are often introduced in the algorithm. These concepts are further explored in Chapter 3.

Reconstruction based algorithms aim to achieve PVC directly in the projection domain, compensating for spatial resolution through resolution modelling. However, in cardiac applications particularly, image-domain PVC techniques are more popular.

The general approach for PVC usually requires characterization of the PSF of the imaging system; characterization of tissue components that participate in the tracer's physiology or metabolism (usually through segmentation of regions of interest in anatomical images); and characterization of the resolution effects in terms of correction factors or maps.

### 2.1.3. PET Image Reconstruction

Tomographic image reconstruction techniques are mathematical based operations that make use of the PET signal in terms of the LOR/TOR information (depending on whether the system is programmed for a 2D or 3D reconstruction, respectively) gathered from the imaging object, in order to form cross sectional images of the scanning object that can be further organized into a 3D image composition.

For the scope of this study, uniquely 2D acquisition modes and hence 2D reconstruction strategies will be explored, which justifies the limitation of the coverage of reconstruction techniques to the bi-dimensional case.

This section is organized in terms of analytical and iterative reconstruction approaches, each one presenting its own advantages and limitations. Analytic reconstruction methods offer a direct mathematical solution for the formation of an image. In this way the reconstruction process can be viewed as an inverse problem, where the inverse of a formula that represents the image formation process is estimated. Therefore, solutions can be computed very quickly and very efficiently. Nevertheless, the resulting data may contain some artefacts due to the fact that attenuation and noise are not accounted for in the most appropriate manner, particularly in PET.

On the other hand, iterative reconstruction methods are based on more complex mathematical grounds requiring multiple steps to arrive at a solution. This approach relies on the selection of the best estimation of the true image, and an algorithm that repetitively attempts to get closer to the solution. They are usually based on statistical estimation methods and probabilistic models which can include factors that contribute to image quality, like noise, detector response characteristics, scatter and attenuation.

In the following sub-section analytical and iterative reconstruction methodologies will be approached: simple and filtered back projection - analytical methods -, maximum likelihood expectation maximization (MLEM) and ordered subsets expectation maximization (OSEM) - iterative methods.

## 2.1.3.1. Analytical Reconstruction Methods

### 2.1.3.1.1. Simple Back-projection

The simple back-projection is one of the simplest methods for image reconstruction in PET.

The projection information saved in the form of a sinogram can be seen as a set of profiles $p(r, \emptyset_i)$ acquired at discrete angle intervals $\emptyset_i$ and with each projection sampled at discrete intervals along the radial coordinate $r$ (Cherry et al. 2003)

Using back-projection, the profile acquired at each angle interval will be projected back into the image space, which means that the number of counts acquired at each projection line will be uniformly distributed between the pixels along that specific path (Fig. 2.6 ) (Cherry et al. 2003).

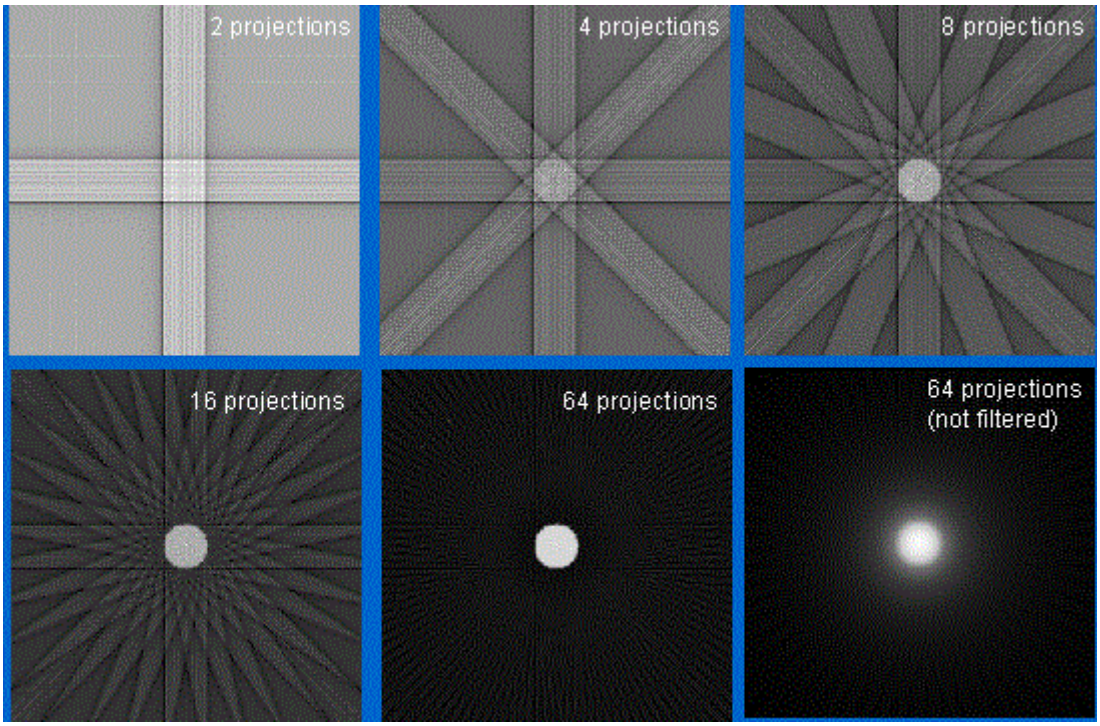


***Figure 2.6*** *- Illustration of back-projection resulting images, with different numbers of projections (Platten, 2003)*

By taking the following equation into account:

$$r = x\cos\emptyset + y\sin\emptyset, \quad \textbf{(Equation 2.3)}$$

The value of each voxel in the resulting image can be defined as:

$$f'(x,y) = \frac{1}{N}\sum_{i=1}^{N} p(x\cos\emptyset_i + y\sin\emptyset_i, \emptyset_i), \qquad \textbf{(Equation 2.4)}$$

where $f'(x,y)$ is the approximation to the true distribution $f(x,y)$, $N$ is the number of profiles measured and $\emptyset_i$ is the $i^{th}$ projection angle (Cherry et al. 2003).

One of the disadvantages of this technique is the fact that an appreciable amount of blurring occurs due to the presence of projection information outside of the original location on the imaging object. This can be seen in Fig. 6. The process to improve image quality requires the usage of an additional amount of projections in order to reconstruct the image. However, the images will always inherently possess a certain amount of blur, even if an infinite number of projections is taken (Cherry et al. 2003).

#### 2.1.3.1.2. Filtered Back-Projection

In order to fully grasp the concept of filtered back projection (FBP), the notion of Fourier Transforms (FTs) needs to be introduced.

FT allows the representation of a spatially varying function $f(x)$ in image space as a sum of sine and cosine functions of distinct spatial frequencies $k$ in "spatial frequency space", also known as *k-space* (Cherry et al. 2003). This operation can be represented as:

$$F(k) = \mathrm{F}[f(x)], \qquad \textbf{(Equation 2.5)}$$

The original $f(x)$ function can be recovered by applying the inverse FT, which can be represented as:

$$\mathrm{F}^{-1}[F(k)] = f(x), \qquad \textbf{(Equation 2.6)}$$

This conceptualisation of a FT in one dimension can be further applied to bi-dimensional spaces, such as the projection space $p(r, \emptyset)$, by using the projection slice theorem, which states:

$$\mathrm{F}[p(r, \emptyset)] = P(k_r, \emptyset), \quad \textbf{(Equation 2.7)}$$

where $P(k_r, \emptyset)$ is the value of the FT at a radial distance $k_r$ along a line at an angle $\emptyset$ in *k-space* (Cherry et al. 2003).

Using these concepts in an image reconstruction routine, the first step is to measure the projection profiles $p(k_r, \emptyset)$, at the $N$ projection angles, and apply the FT to each projection profile (**Equation 2.7**). The next step involves the application of a ramp filter to the resulting $P(k_r, \emptyset)$, which means that each projection is to be multiplied by $|k_r|$ (Cherry et al. 2003):

$$P'(k_r, \emptyset) = |k_r|\mathrm{P}(k_r, \emptyset)\,, \qquad \textbf{(Equation 2.8)}$$

Following the application of the ramp filter, the inverse FT for each projection profile is then calculated:

$$p'(k_r, \emptyset) = \mathrm{F}^{-1}[P'(k_r, \emptyset)] = \mathrm{F}^{-1}[|k_r|\mathrm{P}(k_r, \emptyset)], \qquad \textbf{(Equation 2.9)}$$

As a final step, the image can be reconstructed using the filtered projection $p'(r, \emptyset)$ and **Equation 2.4**:

$$f(x, y) = \frac{1}{N}\sum_{i=1}^{N} p'(x\cos\emptyset_i + y\sin\emptyset_i, \emptyset_i), \qquad \textbf{(Equation 2.10)}$$

where $f(x, y)$ is the discretized true distribution. As opposite to the case of a simple back-projection, FBP allows for the reconstruction of the exact true discretized distribution. However, this behaviour is only projected to occur under this formulation in theory, since measured data contains noise, which incurs in a certain degree of image quality degradation that cannot be fully compensated for (Cherry et al. 2003).

Given the speed and relative ease of implementation associated with this reconstruction approach, the FBP can be viewed as one of the most popular reconstruction methods. However, a number of limitations are associated with this reconstruction technique: 1) Data sets containing low count statistics incur in streak artefacts (Cherry et al. 2003); 2) FBP cannot be adjusted in order to consider various characteristics of the PET system, such as the limited spatial resolution associated with the detectors, scattered events, etc. In order to implement these steps extra processing stages are necessary (Cherry et al. 2003).

### 2.1.3.2. Iterative Reconstruction Methods

These algorithms require more computational power than the analytical methods. However, improvements in their processing speed have led to the implementation of these routines in clinical PET reconstruction. The concept behind these algorithms is illustrated in Fig. 2.7.

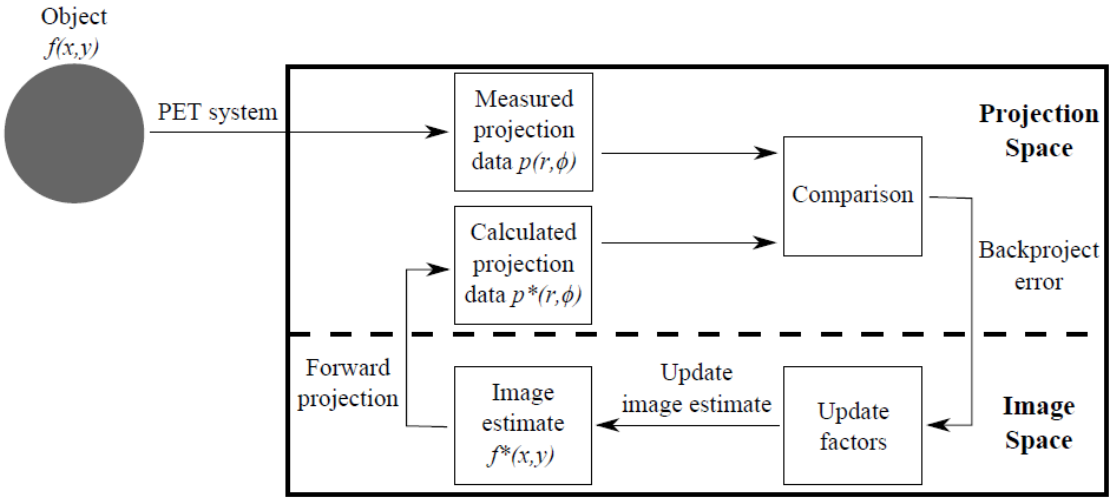


***Figure 2.7*** *- Iterative Reconstruction Process (Cherry et al. 2003)*

The diagram shown in Fig. 2.7 describes an algorithm that aims to reach the true image distribution $f(x, y)$ through a succession of estimates $f * (x, y)$. The first estimate is generally taken as either a uniform intensity or blank image. This initial estimate is then submitted through a process known as forward projection, leading to the generation of a detector response from the imaging object. Associated with this process is the sum of all intensities along the ray paths for all LORs (Cherry et al. 2003).

The calculated projection data $p^*(r, \emptyset)$ is compared against the measured data $p(r, \emptyset)$. The error in the projected space is then back-projected into the image space and used to provide with an updated estimate of the $f^*(x, y)$. This procedure is then repeated in an iterative manner in order to improve the image estimate.

The specifics of the iterative reconstruction methods determine the reasons for these algorithms to incur in a more significant computational load. One reason is that iterative approaches require, logically, that the algorithm runs through a successive number of repetitions towards convergence, until it reaches an acceptable result. Each of these iteration steps include a forward projection and a back projection stages, each one roughly consuming the same amount of time. Since in FBP the back projection step is the most time consuming stage of the algorithm, it is quite understandable that the characteristic nature of iterative methods, which leads to the repetition of this and the forward projection steps for a plurality of times, makes iterative reconstruction algorithms substantially slower in comparison to analytical methods, and FBP in particular. (Cherry et al. 2003)

Iterative algorithms can be viewed as having two essential components: a) the methodology used to compare the measured and current image estimates, in the projection space, $p(x, y)$ and $p^*(x, y)$; and b) the method that leads to the update of the estimate, $f^*(x, y)$, in each iteration. The comparison step is performed with the aid of the cost function and the update of the estimate is done using the update function. This is the general formulation of an iterative reconstruction algorithm, and the development of new methods is basically focused on the usage of new cost or update functions (Cherry et al. 2003).

In the following subsections the MLEM and OSEM algorithms will be presented.

#### 2.1.3.2.1. Maximum Likelihood Expectation Maximization (MLEM)

The MLEM algorithm is based on the estimation of the most likely count distribution considering statistical considerations (Cherry et al. 2003), (Matela, 2008).

The acquired data shall be represented by the vector $\boldsymbol{p}$, where $p_j$ is the number of counts in the $j^{th}$ projection element. A relationship can be established between this measured data and the activity in each voxel, using:

$$p_j = \sum_i M_{i,j} f_i, \qquad \textbf{(Equation 2.11)}$$

where $f_i$ is the number of photon pairs produced in voxel $i$ and $M_{i,j}$ is the system matrix, giving the probability that the photon pair originating from the $i^{th}$ voxel is detected in the $j^{th}$ projection element (Matela, 2008).

Taking into account Equation 11 and its Poisson statistical nature, as well as the maximum likelihood definition, the following relation can be deduced:

$$f_i^{k+1} = \frac{f_i^k}{\sum_j M_{i,j}} \times \sum_i M_{i,j} \frac{p_j}{\sum_v M_{v,j} f_v^k}, \qquad \textbf{(Equation 2.12)}$$

where $k$ is the iteration number and $f_i^{k+1}$ is the activity in each pixel $i$ in the next iteration.

The elements present in the Equation 12 are intrinsically related to the diagram in Fig. 2.7. The sum element $\sum_v M_{v,j} f_v^k$ corresponds to the forward projection, which comprises the step when the information in image space is converted to the projection space (**Equation 2.11**). The measured data $p_j$ is afterwards compared to the estimated data by calculating the quotient. This quotient is weighted by the system matrix element $M_{i,j}$ and then summed, which gives the update factor for each voxel $i$. The last step comprises the multiplication of the update factors with the current estimation (divided by the sensitivity in the image space $\sum_j M_{i,j}$), which leads to the obtainment of an updated image estimation (Matela, 2008).

The MLEM method provides with a good estimate of the real count distribution. However, this approach is associated with two major issues: a significantly high computation time (in comparison with analytic methods, and FBP in particular) – (Kastis et al. 2010) - and stability related issues. These latter issues are related to the fact that the algorithm is based on the attempt to find the signal intensity distribution that best fits the measured data. However, the natural presence of noise in the data leads to the convergence of the algorithm to a solution containing noise as well. In order to avoid the occurrence of too noisy solutions an alternative is to stop the algorithm before the image reaches significantly noisy levels. However, this leads to the obtainment of an image with a particularly limited spatial resolution (Matela, 2008). This noise/spatial resolution relationship is the main compromise that needs to be taken into account in iterative reconstruction algorithms, although this relationship is also true for FBP.

Additional information regarding the derivation of Equation 12 can be found in Matela (2008).

#### 2.1.3.2.2. Ordered Subsets Expectation Maximization (OSEM)

The OSEM algorithm was initially proposed by Hudson and Larkin in 1994 (Hudson and Larkin, 1994). This algorithm is quite similar to the MLEM technique, with the exception that the projection data is divided into subsets, seeing that this step was implemented in order to reduce the computational time associated with the MLEM.

The algorithm can be described by reorganizing **Equation 2.12** in the following way:

$$f_i^{k+1} = \frac{f_i^k}{\sum_{j \in S_n} M_{i,j}} \times \sum_{j \in S_n} M_{i,j} \frac{p_j}{\sum_v M_{v,j} f_v^k}, \qquad \textbf{(Equation 2.13)}$$

where $S_n$ is the $n^{th}$ subset.

The main difference with regards to the MLEM approach – observable in the discrepancies between **Equations 2.12** and **2.13** – is the fact that the sum of the projection data is not performed in the complete data set. Instead, a subset of iterations is performed only in terms of the projections associated with each $S_n$ subset. By breaking the operation into simpler calculations, the algorithm becomes significantly faster than the MLEM, with the cost of aggravating the issues in terms of stability. This higher computational efficiency achieved with the OSEM algorithm led to the possibility of computing iterative image reconstruction techniques at a time frame compatible with the requirements of clinical imaging, which made OSEM and its variants popular reconstruction strategies.

## 2.2. Cardiac Anatomy

The heart is an organ with an approximately conical geometry, lying in the middle of the mediastinum, between the lungs and enclosed in the pericardium. Its size averages about 12 cm length, 8 to 9 cm at the broadest region, and approximately 6 cm depth, in a fully grown adult.

The cardiac organ is limited at the exterior by a thin layer, the epicardium, and in the interior by the endocardium, comprising a thick middle layer formed by cardiac tissue, the myocardium.

The heart is oriented obliquely in the thoracic cavity, situated behind the body of the sternum and adjoining parts of the rib cartilages, projecting usually slightly into the left, so that around one-third of its volume is comprised on the right and two-thirds the left side of the median plane of the human body.

The heart is divided by a septum into two halves, which are further subdivided by a constriction into two pairs of cavities, the upper being the atriums, and the lower being the ventricles. The pumping system of the heart works in the sense of collecting poorly oxygenated blood from the vena cava system into the right atrium, which contracts its content into the right ventricle, which in turn pumps the blood into the pulmonary vein, where it follows the arterialization process in the pulmonary system. Then, the oxygenated blood heads towards the left atrium, where it is further expelled into the left ventricle, which in turn pumps its content into the systemic circulation. Each cardiac chamber undergoes therefore a dynamic cycle comprising filling - and hence volume increasing - and contracting – or volume decreasing - phases, known as diastolic and systolic periods, respectively.

The heart consists therefore of a dynamic four chamber organ, with each half working separately in order to oxygenate blood in the pulmonary tract and supply this oxygen through the systemic tract.

We focus our efforts on the LV in particular, where nuclear medicine cardiac applications are mainly concentrated due to left ventricular systemic importance, and where IVS are expected to produce a more significant bias, due to their larger characteristic dimensions.

The LV is the most muscled of the four cardiac chambers, which is due to its inherent function of pumping blood with a high pressure into the systemic circulation. The LV wall is approximately 3 times thicker than the right ventricle (RV) one. Besides, the LV integrates a longer and more conical shaped cavity than the RV, having a perpendicular cross section that features a nearly circular outline.

The LV wall thickness is variable, being thicker at the base level, slenderizing into a minimum value at the apex region (Bogaert et al. 2005). Its wall thickness averages 8 mm at end-diastole (Bogaert et al. 2005), and can increase up to around 15 mm at end-systole (Johnson et al. 2011).

In terms of general geometry, the end-diastole LV has the approximate morphology of a truncated ellipsoid (Petitjean et al. 2011), reaching about 5 cm inner-cavity diameter, at the broadest level, approximately 120 mL volume capacity, and circa 9 cm cavity length (Henriksen et al. 1996).

The LV cavity comprises internal prominences, the *trabeculae carneae* (TC). These are rounded and/or irregular columns which project densely, essentially from the apex and posterior wall of the ventricle. The TC are of three kinds: some attach themselves along their entire length on one side and merely form prominent ridges, others are fixed at their extremities but free in the middle, while a third set, the papillary muscles (PM), are a special kind and often viewed as independent structures, that are continuous with the wall at their bases, while their apices give origin to collagenous *chordae tendineae* which in turn are attached by their other extremity to the cusps of the mitral valve (Grey 1918). The LV PMs are two in number, the posterior and anterior one, being appreciably larger compared to the remaining internal ventricular structures. Fig. 2.8 shows a depiction of PM and TC inside the LV cavity.

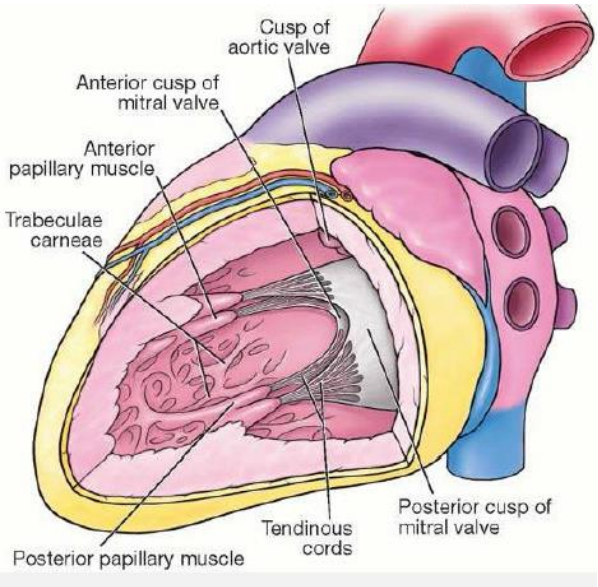


***Figure 2.8*** *- Open view of the LV free wall: PM and TC (Moore et al. 2010)*

The PMs contract slightly earlier than the ventricular walls, and their function consists on preventing valve prolapse to the atrium during ventricular contraction, through the function of the *tendinous cords*, having an important role in avoiding valve regurgitation. Besides having a

similar function, TC also provide most of the LV inner wall with a rough surface, preventing suction that would otherwise occur in a completely flat-surfaced endocardium.

The precise location and geometry of IVS vary significantly across the cardiac cycle, and from individual to individual as well, which may introduce some variances in terms of their PVE influence over the LV wall.

These intraventricular structures manifest radiopharmaceutical uptake in perfusion studies.

### 2.2.1. The 17 Segment Model

An effort has been made by the *American Heart Association* (AHA) in order to standardize LV imaging assessment and quantification (Cerqueira et al. 2002). A 17 segment 'bullseye' model was created with a precisely defined set of criteria. This model consists basically on a 2D representation of the tri-dimensional structure of the LV. These constructions allow for a common method of viewing, comparing and quantifying LV images from different patients/ image acquisitions. The division of the LV in segments had to maintain consistency with accepted anatomic and autopsy data; had to use existing and accepted approaches to myocardial segmentation and nomenclature; had to allow for precise localization by using anatomical landmarks whenever possible; had to provide adequate sampling of the left ventricle and coronary vessel system distribution without exceeding the resolution limits of the imaging modalities of relevance for clinical application; and had to allow for linkage of the segments to known coronary arterial topography as defined by coronary angiography.

The division model is illustrated in Fig. 2.9. The relationship between the model and LV regions is depicted in Fig. 2.10.

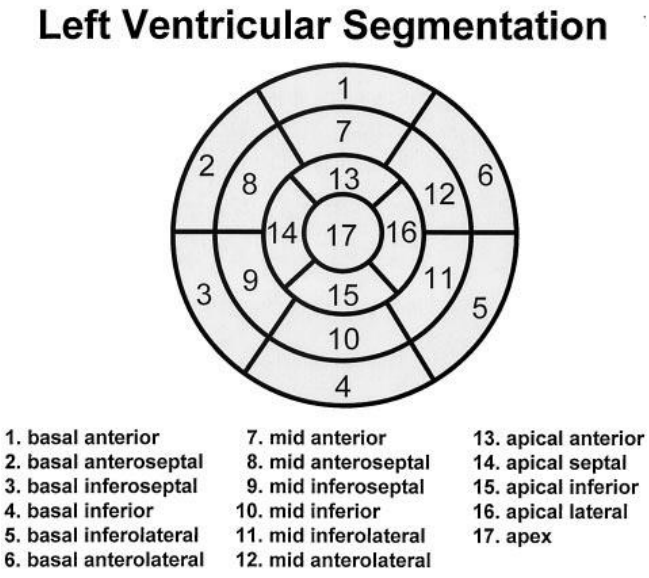


***Figure 2.9** - LV 17 segment model (Cerqueira et al. 2002)*

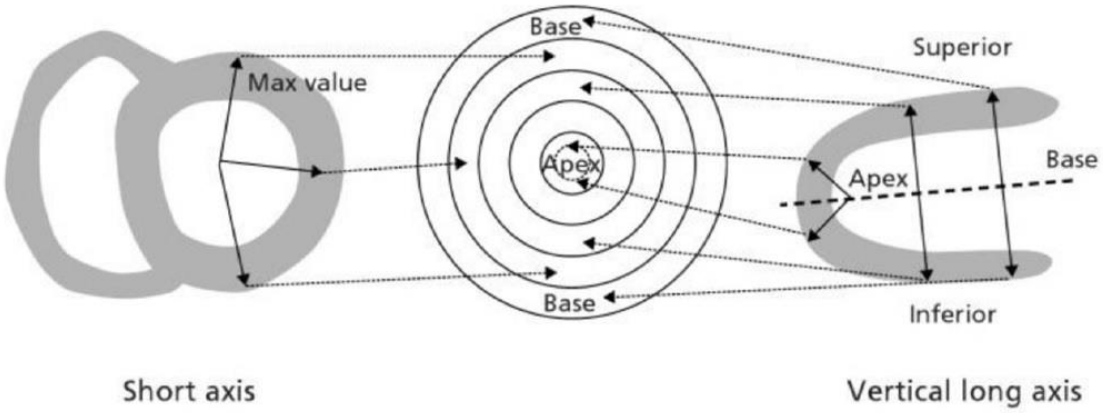


***Figure 2.10*** *- General relationship between LV 17 segment model and myocardial regions (Groch & Erwin, 2001)*

The diagram shown in Fig. 2.9 represents a flattening of the LV, and it sets a concentric distribution of pre-defined segments into radial layers, with the first stratum extending from the mitral annulus to the tips of PM at end-diastole, comprising 35% of the total LV length; the second containing all the extent of the PM, from their tip to their base, also comprising 35% of the LV length as well; the apical region going from the base of the PM to the end of the cavity, comprising about 30% of the cavity's length; and the apical cap region, which consists on the myocardium area beyond the end of the LV cavity, as shown in Fig. 2.10 and 2.11.

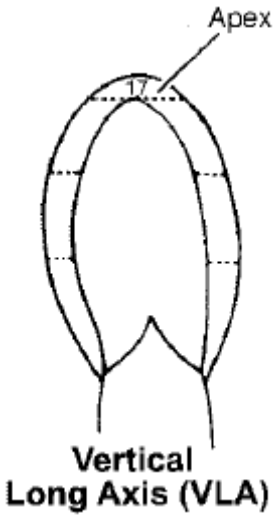


***Figure 2.11*** *- Illustration of a vertical long axis LV view with the depiction of the apical cap (Cerqueira et al. 2002)*

Additionally, Figs. 2.11 to 2.13 illustrate a further standardisation where specific imaging planes are suggested as reference ones. Fig. 2.11 depicts the vertical long axis view, which is in turn complemented by Fig. 2.12 and 2.13, which illustrate a short axis and horizontal long axis heart views, respectively.

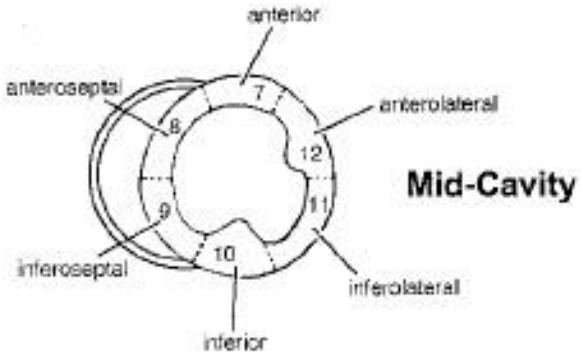


***Figure 2.12*** *- Illustration of a mid-cavity short-axis heart view (Cerqueira et al. 2002)*

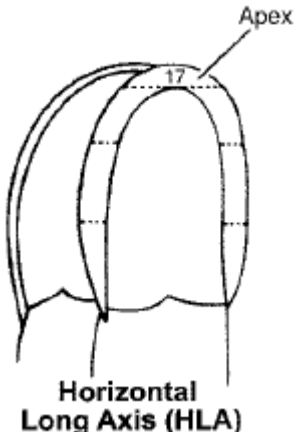


***Figure 2.13*** *- Illustration of a horizontal long axis heart view (Cerqueira et al. 2002)*

It is worth mentioning that the circumferential division of segments observable in Fig. 2.12 is based on anatomical and physiological features such as right ventricle (RV) and LV wall intersection regions, PM locations, LV tampering and coronary perfusion regions. A more detailed description of the circumferential division features of the LV can be assessed in Cerqueira et al (2002).

The problem that manifests is that according to the current bibliography, IVS are not currently being taken into account in cardiac ventricle segmentation for PVC purposes (Petitjean et al. 2011). However, to the date of completion of this report there is no study that supports this segmentation approach as well.

Internal ventricular structures highlight the negative influence of PVE by locally increasing the wall thickness, hence reducing the normal amount of blur in the cardiac ventricular wall, leading to potential misinterpretations due to a qualitative and quantitative subsequent apparent hyper-activity in adjacent wall regions. Therefore, hypo-perfused regions in the wall next to IVS may go unnoticed due to this PVE severity decline, adding to the fact that papillary muscles and mainly *trabeculae carneae* have inherently irregular structures and significant location variability between individuals (Cerqueira et al. 2002), (Spreeuwers et al. 2005). Therefore, it becomes important to assess if IVS produce a significant influence in terms of PVE, and hence if ignoring them in PVC approaches produces an appreciable error or not.

# 3.*PVC Methods*

In general, PVC methods have been applied in the context of neurology, oncology, cardiology, as well as in phantom and simulation studies. Even though the literature regarding brain PVC remains far vaster than the remaining, cardiac PVC has been subject to a significant and increasing amount of interest recently (Pretorius & King, 2009).

In this chapter a general overview of PVC techniques has been provided, following a description of previous and state-of-the-art PVC approaches implemented specifically in cardiac emission images or cardiac phantoms.

## 3.1. General Overview of PVC Techniques

In their essence, PVC methods can be divided into reconstruction and post-reconstruction based approaches. However, both implementation types result in image artefacts due to high frequency information loss during data acquisition (Erlandsson et al. 2012). This justifies the inherent need for high resolution spatial information, as stated in the previous section.

Both reconstruction and post-reconstruction PVC methods can make use of high spatial frequency information from anatomical imaging modalities, or they can be purely image driven. Cardiac PVC methods in particular usually follow an approach that makes use of anatomical information and are generally implemented in a post-reconstruction basis.

PVC methods can be further subdivided into region of interest (ROI) and voxel based approaches. The main difference is that in ROI based techniques only the mean value in a region is generally estimated, while in voxel based techniques the correction is performed at the level of each individual voxel.

This section therefore encompasses a description of PVC techniques, giving special emphasis to post-reconstruction approaches.

### 3.1.1. Post-reconstruction based PVC

#### 3.1.1.1. ROI Based Approaches

#### 3.1.1.1.1. Recovery Coefficient Method

The Recovery Coefficient (RC) method presents as one of the first approaches to PVC, being implemented for the first time by Hoffman et al. (1979). The authors defined the RC as the quotient between the apparent and true activity concentrations of an object of interest. This work was one of the pilot studies that discovered a high dependence on object size in PVE. The method starts by pre-calculating a set of RC values based on objects of known activity, size, shape and location within the PET scanner. In order to apply the method one simply needs to divide the measured activity value in a specified ROI, where this value is taken as the maximum or mean value in the targeted region, by the appropriate RC. It is worth noting that the original description of the method had the inherent assumption that the volume and shape of the functionally active region are approximately known, and often the functional part is assigned to correspond to the anatomical delimitations of the object, using structural imaging modality information (CT or MRI).

Although Hoffman et al. (1979) did not provide a mathematical expression for the RC description, a rigorous definition was given by Erlandsson et al. (2012).

The original depiction of the method (Hoffman et al. 1979) tackled PVE in a context of hot objects against cold backgrounds, which lead to this method being able to deal only with spill-out, hence only half of the PVE problem (Soret et al. 2006).

#### 3.1.1.1.2. Geometric Transfer Matrix

The Geometrical Transfer Matrix (GTM) method appears as a natural extension of the RC method presented by Hoffman et al. (1979), by being able to take into account and correct for both spill-in and spill-out effects, working in a multiple region basis. Although first introduced by Henze et al. (1983), the method was fully described for the first time by Rousset et al. (1998) in the context of PET brain imaging to correct for spill-over effects among gray matter (GM), white matter (WM) and cerebrospinal fluid (CSF).

The method, based on anatomical information (originally MRI), requires the delineation of $\boldsymbol{n}$ functional non-overlapping structures of interest, covering the whole image and assuming uniform activity concentration in each so called compartment. The mean value is usually employed to describe each ROI. This value is stored in a vector $\boldsymbol{v}$ of length $\boldsymbol{n}$, where $\boldsymbol{n}$ is the number of different compartments.

Then follows a convolution of a binary mask of each compartment with the system's PSF, which yields an image that depicts the proportional contribution in terms of signal emanation from each compartment to each of the other $\boldsymbol{n-1}$ regions. Repeating this step for each one of the compartments leads to the calculation of transfer coefficients ($\boldsymbol{W_{ij}}$), which correspond to the fraction of activity emanating from compartment $\boldsymbol{i}$ and detected in compartment $\boldsymbol{j}$. All the fractional contributions are aggregated in a $\boldsymbol{n} \times \boldsymbol{n}$ matrix, the GTM.

Each row and column should add to 1 in order to incorporate the overall activity to and from each compartment. The factors present in the matrix's main diagonal account for the spill-out of each compartment. Accordingly, the observed activity in each region ($\boldsymbol{v}$) can be described as:

$$v = GTM.V\ , \quad \textbf{(Equation 3.1)}$$

where $\boldsymbol{V}$ is the vector containing the true mean activity values for each compartment. Therefore, the true regional mean activity values can be calculated as:

$$V = GTM^{-1}.v \text{ , (\textbf{Equation 3.2})}$$

However, given these steps it becomes easy to understand that the main disadvantage of this method (and ROI methods in general) is that it works under the assumption that the true mean activity vector (V) relies on a perfect segmentation (capturing the ROIs perfectly) and on the fact that the activity within each ROI is constant (ROI uniformity), which is obviously not the case in practical terms.

### 3.1.1.2. Voxel Based Approaches

#### 3.1.1.2.1. Muller-Gartner Method

Voxel based PVC methods appear as a somewhat evolution from ROI based approaches, since these are not based on the assumption of ROI uniformity.

The Muller-Gartner (MG) method is one of the most popular PVE compensation methods (Erlandsson et al. 2012).

The MG method appears as an extension of two pixel-based PVC strategies. Videen et al. (1988) formulated an approach that used anatomical information from CT or MRI in the context of brain PVC. The method consisted in segmenting the brain into cerebral and non-cerebral tissue, assuming that non-brain regions would have no tracer content (Erlandsson et al. 2012), (Videen et al. (1988). This approach had the advantage of compensating for GM and WM, respectively, considered together as the cerebral tissue compartment, from the signal dilution in non-active tissue such as the CSF space (Rousset et al. 2007). After segmenting the anatomical data into these two regions, a binary map of the brain tissue is to be convolved with the system's PSF, in a voxel-by-voxel fashion, in order to get the RC for each individual pixel. The resolution compensation is then applied by dividing the observed PET image by the correction coefficients, in a voxel-by-voxel basis.

One must note that this PVC strategy is essentially the same as the RC method (Hoffman et al-1979), with the particularity of extending the original method from a ROI to a voxel-by-voxel framework.

Videen et al. (1988) applied the method in 2D, which was further extended into a 3D implementation by Meltzer et al. (1990).

Nevertheless, the handicap of not being able to separate GM and WM remained.

Muller-Gartner et al. (1992) further improved the original voxel-based method by allowing for the incorporation of three regions, namely GM, WM and CSF. Although the GM was regarded as the target region and the other two as background, GM and WM were considered as different and independent compartments.

The Muller-Gartner (MG) method implies removing the spill-out effect by subtracting the effect of the WM and, if it is considered to have activity, CSF, by convolving the mask of each of these structures (multiplied by their respective observed image voxels) with the system's PSF,

subtracting this value to the observed PET image, and then dividing the result by the convolution between the PSF and a GM mask, all done in a voxel-by-voxel basis.

The method can be described by **Equation 3.3**:

$$f_{GM} = \frac{f_O - ([C_{WM} p_{WM}] \otimes PSF + [C_{CSF} p_{CSF}] \otimes PSF)}{p_{GM} \otimes PSF}$$ , **(Equation 3.3)**

where $f_O$ is the observed image, $C_{WM}$ and $C_{CSF}$ the mean activity values in the WM and CSF ROIs, respectively, $PSF$ is the system's PSF, originally considered constant throughout space, $p_{WM}$, $p_{CSF}$ and $p_{GM}$ the binary masks of each set of voxels, and $f_{GM}$ the final corrected image for the GM tissue type.

One must note that the main disadvantage of this approach is that it assumes that the two non-overlapping sets of voxels, corresponding to WM and CSF, are not contaminated by PVEs (Rousset et al. 2007). Additionally, the compensation is applied solely to the targeted region's pixels (Erlandsson et al. 2012).

In Da Silva et al. (1999), the MG method was adapted in such a way that instead of being based on convolving sets of pixels with a PSF, the anatomically based regional maps were forward projected according to a model that incorporated attenuation and distance dependent resolution variation information, and then the same reconstruction method as the one implemented on the MG method was applied, in the image to be corrected. This approach allows for the obtainment of a more realistic blurring estimation by taking into account PSF spatial variance, particularly important in SPECT studies, where the PSF has a significant location dependence. Given the introduction of this reconstruction component, this modified MG method is classified as both post-reconstruction and reconstruction based. However, there is not an actual PVC implementation in the reconstruction domain, only the attainment of a more realistic blurring effect of each of the compartments. The compensation is ultimately applied in the post-reconstruction domain and not in sinogram data.

The two approaches of the same method were compared, with no significant differences found between the two in Frouin et al. 2002 (Soret et al. 2003).

## 3.1.2. Reconstruction Based PVC

### 3.1.2.1. ROI Based Approaches

These approaches consist in quantifying ROIs directly from projection data, taking into account the spatial resolution and other effects, such as scatter. This method was first proposed by Huesman (1984), being further applied in cardiac (Muzic et al. 1998), and oncology studies (Chen et al. 1999). Carson (1986) developed an iterative maximum-likelihood expectation-maximization) MLEM algorithm for the same purpose as Huesman. Alternatively, a method based on a least-squares algorithm was developed by Formiconi (1993) and further implemented by Vanzi et al. (1993) in terms of brain SPECT. However, similarly to the methods developed by Carson and Huesman, these approaches by Formiconi and Vanzi had the disadvantage of requiring a segmentation of the whole object. Moore et al. (2012) developed an approach in which only a few tissues needed to be segmented. This method consists in a mixture of ROI and voxel based approaches, stating that only projection rays travelling through the 3D ROI are used to

estimate the mean activity concentration in each tissue type. Also, the contribution of the background outside the ROI is accounted for by re-projecting through the reconstructed image outside the ROI. The main advantage of this approach is the validity of a number of noise assumptions, namely the noise is considered to be spatially uncorrelated and Poisson distributed, which is valid for Huesman's and Carson's approaches as well.

#### 3.1.2.2. Voxel Based Approaches

In this class of PVC approaches the system matrix is modeled in order to more accurately incorporate the blurring effects in PET, from different sources, namely positron range, photon non-collinearity, inter-crystal scattering and/or crystal penetration effects

Although voxel based reconstruction-domain methods are outside of the scope of this work frame, further descriptions of these PVC approaches are present in Erlandsson et al. (2010 and 2012), Erlandsson & Hutton (2010) and Rahmim et al. (2013).

## 3.2. Cardiac Applied PVC

Da Silva et al. (1999) were one of the first to implement the MG method in a cardiac framework, having used it in SPECT studies. However, they introduced adaptations in the method that, as explained in section **3.1.1.2.1,** accounted for the spatially-dependent resolution variation of the SPECT camera. In their study they started by evaluating the method with phantom data, having further applied it to animal studies (Da Silva et al. 2001).

Nuyts et al. (1996) developed a PVE compensation approach similar to that of Muller-Gartner (1992), but directed to myocardial PET images and taking the LV wall as the targeted compartment. However, their myocardial wall delineation approach was based on PET images instead of high resolution anatomical data.

Hasegawa et al. (1997) implemented a similar method with respect to Nuyts et al. (1996), with the goal of quantifying regional myocardial uptake in SPECT perfusion imaging. The method was called template-projection reconstruction, which is basically the reconstruction based MG method described in section **3.1.1.2.1,** with the main difference that the approach involved 3D CT defined cardiac ROIs to determine voxel-by-voxel RC by projecting a template of the myocardial wall and reconstructing these template projections in the same way that SPECT acquisitions were reconstructed.

Pretorius & King (2009) further extended the methods implemented by Nuyts et al. (1996) and Hasegawa et al. (1997), incorporating an additional parameter in the PVC methodology, the Voxel Filling Fraction (F), which specifies the extent to which structure edge voxels in the emission reconstruction are filled by the structure in question, as determined by the corresponding higher spatial-resolution imaging modality and the fractional presence of the structure at different states of physiological motion, as in combining phases of cardiac motion. The method was applied to simulated SPECT images. The authors concluded that the filling factor incorporation produced better results than the mere implementation of attenuation correction, scatter correction and MG method alone, when no misalignment between functional and anatomical images was incorporated. However, the study showed that prior anatomical knowledge of myocardium

perfusion defects is absolutely necessary for the method to be applied. The authors used software phantoms to perform the tests.

Y. Du et al. (2013) were also inspired in Nuyts et al. (1996) in their work regarding the usage of the MG method for cardiac applications, but differently from Pretorius and King (2009), they used the method to implement correction procedures in actual PET images. The approach used consisted of an adapted MG method to compensate for both spill-in and spill-out in respect to LV, blood pool (BP) and background regions, applying the MG method in each region, in an iterative basis, using high resolution CTA (Computed Tomography Angiography) images to allow for ROI individualization. The implementation was tested using simulations and animal studies. The authors concluded that PVC should be applied independently for each of the cardiac phases and that uptake defects should constitute independent structures from the LV wall in the compensation process.

Johnson et al. (2011) made use of clinical PET data to suggest a new adaptation for PVC. The authors made use of a simple post-reconstruction method, the RC technique, for systole PVC, using prior knowledge of a typical PET scanner's PSF, and taking positron range of $^{82}$Rb into account. Following this, a combination of the systolic/diastolic ratio of the apparent myocardium activity measurements were used to PV correct the diastolic phase of the heart. The group concluded that using the combination described allowed them to successfully include a correction scheme for positron range in PVC.

Regarding reconstruction approaches, Muzic et al. (1998) made use of projection domain ROI-based PVC in order to compensate for image degradation of PET data. The authors presented and evaluated a methodology for ROI quantification based on sinogram data only, not requiring the dynamic data sequences to be reconstructed. Moreover, estimates of region variance were also obtained, similarly to Huesman (1984). These estimates were suggested to be used to define weights for model analyses that use weighted least squares minimization in order to obtain unbiased parameter estimates. The authors evaluated the method using both simulated and measured data and concluded that with appropriate models for spatial resolution and scatter effects, the approach was unbiased and capable of quantifying a myocardial activity concentration with no more than 5% error in accuracy for a myocardium wall as thin as 10 mm, comparable to a diastolic LV wall (Muzic et al. 1998).

Rahmim et al. (2008) published one of the few papers that made use of projection domain based PVC with cardiac applications. The method uses a voxel-based reconstruction PVC technique. The work proposes a new approach that models various resolution degrading effects in PET and combines and incorporates them within the statistical image reconstruction framework. It shares features present in Johnson et al. (2011) to evaluate and compensate for $^{82}$Rb positron range resolution degrading effect. However, the authors incorporate a non-uniform blurring due to $^{82}$Rb positron range. The other blurring features accounted for are photon non-colinearity and inter-crystal scatter and penetration. The authors concluded that the method outperformed previous image degradation compensation reconstruction models (Rahmim et al. 2008 and 2013).

Dumouchel et al. (2012) made use of a methodology related to reconstruction based ROI methods (section **3.1.2.1**) for PVC in mouse cardiac phantom images. The model was based on Ghambir's algorithm (Ghambir et al. 1990). The images were acquired according to an ECG-gating (electrocardiogram-gated) scheme, and the algorithm was implemented to each individual gate to minimize cardiac motion associated PVEs. The PVC was tested with simulation processes and a physical 3D mouse LV phantom. *In vivo* cardiac FDG mouse PET imaging was also performed. The authors concluded that the developed image-based PVC algorithm successfully managed to increase the accuracy and uniformity of PET activity distribution in normal mice hearts.

## 3.3. Non-cardiac PVC Methods

One of the innovative aspects of this study is that PVC methods that have not been previously implemented in cardiac applications, have been used in this work.

This section is dedicated to the description of PVC methodologies that have not been directly applied to studies involving the cardiac apparatus, but that demonstrate potential be successful in doing so.

In this section a description of the Yang method is presented, which can be characterized as being an evolution from the MG method. The next level iterative Yang and region based voxel-wise (RBV) correction methods are also described.

### 3.3.1. Yang Method

One of the main disadvantages of the MG method is the fact that the correction routine is only applicable to voxels within the target region of interest. Yang et al. (1996) presented a method where PVC can be applied to the whole image, as opposite to specific target regions (Yang et al. 1996). This method is characterized by the creation of a piece-wise constant image, in which each region is represented by its true relative mean value ($A_i^r = \frac{A_i}{A_1}, \forall i$), where $A_1$ is the mean value in a pre-determined reference region. This image is convolved with the system's PSF, and PVC factors are obtained following the calculation of the ratio between the image before and after the convolution procedure.

This method can be considered as an extension of the Videen approach (section **3.1.2.1**), from one to a plurality of regions. A specific trait of this technique is the fact that it requires knowledge of the true relative activity concentration in all regions (no need for absolute values, although this approach only produces relative values as well), which is still quite a strong requirement. In Yang et al. (1996), the method was applied to brain blood flow studies in order to correct for the cross-contamination between the GM, WM and CSF brain regions, which were assigned the relative mean values of 4, 1 and 0, respectively. Fig. 14 illustrates the nature of the Yang method in a 1D phantom profile (Erlandsson et al. 2012).

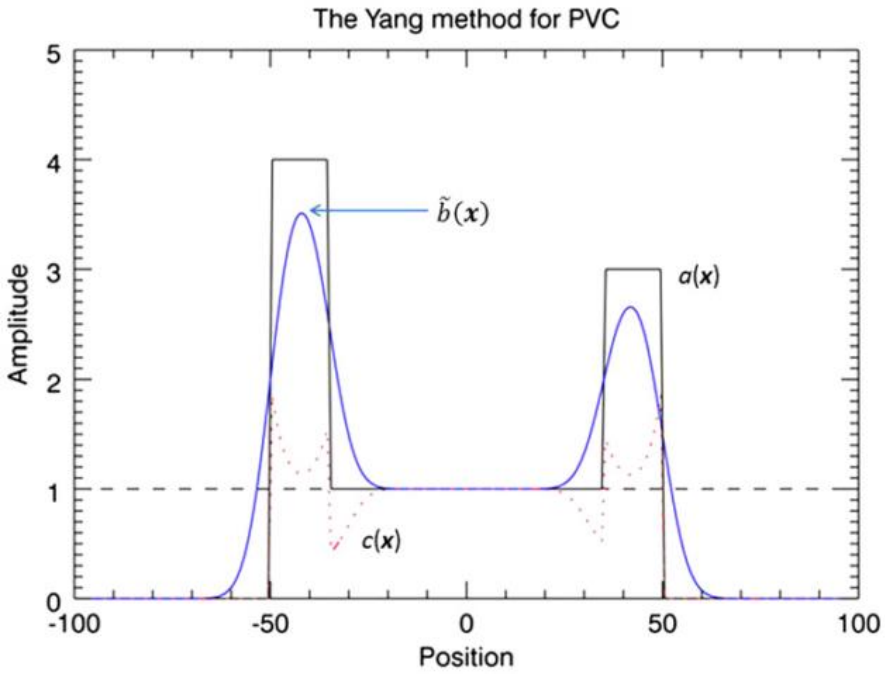


***Figure 3.1** - Illustration of Yang's PVC method in 1 dimension (Erlandsson et al. 2012)*

This Fig. 3.1 illustrates the original signal profile in a black line ($a(x)$), as well as the post-reconstructed signal profile ($b(x)$), in blue. The red dotted line represented by $c(x)$ corresponds to the correction factors.

In any case, both the MG and Yang methods have a significant disadvantage associated, as these methodologies require the provision of initial information regarding the mean or relative mean values in the different image regions. New approaches have been proposed, in which this is avoided. The alternatives involve the combination of the MG and Yang methods with the GTM technique, respectively.

## 3.3.2. Multi-target Correction (MTC)

The Multi-Target Correction (MTC) technique appears as an extension of the MG method, and was first proposed by Erlandsson et al. (2006). The first step of this method involves the use of the GTM technique to obtain initial estimates of the true mean values in all regions. The next step is the repeated application of the MG method formula with multiple background regions, so that each region is taken as target, in turn, whilst the remaining regions are taken as background areas. Hence, all regions would be considered, interchangeably, as a target or background region. The correction routine in each region would be independent from that of all the remaining regions.

## 3.3.3. Region-based Voxel-Wise (RBV) Method

The RBV was initially presented by Thomas et al. (2011a) as a modified version of the Yang method. The regional mean values of each region are obtained using the GTM method, and the Yang correction is then implemented. In a certain way, the obtained results are similar to those of the MTC method, but the RBV method has the advantage of being easier to implement.

## 3.3.4. Iterative Yang (iY) Method

As seen in section **3.3.1**, Yang et al. (1996) introduced a segmentation-based PVC in the context of PET brain studies. The essence of this method resided on the introduction of a PVC factor $I_{pure}/I_{simulated}$, where the "pure" image consists of the matched segmented MR image in which each segment corresponds to the mean value of PET activity; and the "simulated" image is simply the $I_{pure}$ image blurred by a PSF of the PET scanner in question. Thomas et al. (2011) modified the method by iterating the correction factor and reported fast rates of convergence in brain PET clinical applications. The algorithm is described below.

The method is based on matching an emission image $f$ to a segmented image $X$. This can be correlated to a dual modality imaging application, in which the image $f$ can correspond to PET/SPECT data, and $X$ can be assumed to correspond to a segmentation of a registered MRI/CT image. The segmentation step partitions the image $X$ into a number of non-empty sets $P_m$, which cover $X$ and are pairwise disjoint segments. For each set $P_m$ in the partition, the mean value based on the current estimate of intensity is determined as per **Equation 3.4**.

$$\mu_m^{(k)} = \frac{1}{n_m}\sum_{i\in P_m} f_i^{(k)} \quad \textbf{(Equation 3.4)}$$

where $n_m$ is the number of voxels in $P_m$, $i$ denotes the voxel index, and $k$ represents the current iteration. The initial estimate $f^{(0)}$ represents the original emission image. If $p_m$ represents a binary mask associated with the segment $P_m$, then:

$$p_m = \begin{cases} 1, & i \in P_m \\ 0, & otherwise. \end{cases} \quad \textbf{(Equation 3.5)}$$

The "pure" version of the image is then created by assigning the mean values to each partition,

$$s_i^{(k)} = \sum_{m=1}^{M} \mu_m^{(k)} p_m \quad \textbf{(Equation 3.6)}$$

The new estimates of the image intensity are obtained iteratively as per the updated formula given by **Equation 3.7**.

$$f_i^{(k+1)} = f_i^{(k)} \frac{s_i^{(k)}}{s_i^{(k)} \otimes h_i} \quad \textbf{(Equation 3.7)}$$

Where the denominator represents the convolution (and hence blurring) of the "pure" image with the PSF of the system associated with the acquisition of image $f$.

The main advantage of this method resides on the fact that the mean values in each ROI can be estimated using an iterative process, instead of using the GTM method. As only a few of these iterative operations are necessary (typically in the range of 3-5), this procedure presents to be simpler to implement as well.

## 3.3.5. Non-cardiac PVC Methods Summary

Summarizing, the MTC, RBV and iY methods have the common basis of comprising voxel-by-voxel correction routines, applicable to the whole image, not requiring any prior information in respect to the activity distribution on the object, and these can be used to perform a correction routine in an image with an indefinite number of ROIs. However, the iY method is the most computationally efficient technique, which leads to the consideration of this methodology in particular for the PVC routines used in this study.

The process shall involve the separation of the cardiac apparatus into a number of ROIs assumed to have their own uptake values, which will include the LV and RV myocardium, the BP, and a selected IVS with pre-adjustable geometrical properties.

The iY technique shall then be validated with the application of a known blur to the original image (convolution with a known PSF), through the form of simulated reconstruction routine, and further deconvolution of this blur by application of the PVC method in question.

# 4.*Methods*

## 4.1. Introduction

This section comprises the description of the approaches utilized to fulfill this project. The presentation of each consecutive step follows the same logical architecture of this study. In section **4.2** the first level approach towards the evaluation of IVS PVE influence is described. This description involved the listing of all activities from construction of the anatomical model, to the process of convolution with a simulated system's PSF. Section **4.3** describes the steps towards evaluating a potential detour from the chosen research path, in which dog myocardial perfusion SPECT data was evaluated. Section **4.4** continues the study on IVS blurring influence, and describes a more realistic method of evaluating this effect. Lastly, section **4.5** comprises the description of the PVC process implementation in terms of testing the IVS influence, from PVC methodology selection to plan for quantitative evaluation.

## 4.2. First Level Approach - Simple Blurring

The approach for building a model to assess IVS influence required a balance in terms of making the model as simple as possible, while not disregarding potential critical features that would be essential for the model to be considered realistic, at a reasonable level.

Only the LV and RV walls, IVS and BP were modelled, keeping other potentially influential organs such as the liver, lungs and even atria out of scope, in order to achieve a better simplification and to avoid these structures from masking IVS influence, since assessing this is the main goal of this framework. A further simplification in the approach was the absence of noise modelling, which was also done in order to better quantify IVS influence and to maximize the simplicity of the model, in this first stage.

This first level approach was also a study on its own, having the partial goal of making an initial assessment of whether it would be worth to follow a more detailed approach, or if the PVE produced by the IVS could be considered as negligible, to a reasonable level.

The premise on which this approach was based consisted in investigating the relative importance of IVS in terms of their PVE influence, in a comparative framework with respect to

the BP, seeing that the latter is normally taken as producing a significant PVE over the myocardial wall in the literature.

A number of parameters were used to evaluate IVS PVE variability, in order to assess the potential ranges of relatively realistic values around which the PVE could fluctuate, namely the IVS diameter, IVS-wall separation and LV wall thickness, so that the estimate of the influence of IVS could be made in terms of a quantitated spectrum of PVE values.

Also, PM and TC were differentiated during the study, since different geometrical assumptions apply to each of these types of structures.

In order to reach the project's aim, a process comprising a series of well-defined steps was formulated. The first step consisted in the creation of a simplistic LV anatomical 3D model, with the further combination of a RV and a single isolated IVS whose size and geometry could be customised. This resulting object was assigned with a uniform activity distribution. The model was further completed with the option of adding a BP within the ventricular heart's cavities. Secondly, the system's impulse response to a point source, the PSF, was modelled as a symmetrical spatially-invariant Gaussian function. The third step was twofold and consisted in a 3D convolution operation between the system's PSF and the original object in two different formats, one with the IVS and one without it, creating subsequently two different activity concentration distributions. The fourth step comprised a multiplication of each blurred distribution with a binary mask of the LV wall, in order to obtain only the final activity in the LV's defined anatomy. Step five involved a 3D segmentation of the LV according to the AHA 17 compartment model (Cerqueira et al. 2002), as described in section **2.2.1**. The sixth step consisted in quantifying the spill-in in each segment of the blurred wall model with an IVS, and in a parallel way the same quantification would be made for the blurred model of the wall without an IVS. In the last step the overall differences in activity between each LV (total PVE) and each corresponding LV segment (local PVE) of the two blurred models were evaluated.

Therefore, all the PVE quantifications performed throughout the studies were made in terms of total and local spill-in from IVS or BP. Total spill-in corresponds to all the counts that were included in the LV wall, but originated from another ROI. The local spill-in corresponds to the number of counts that were included in each of the individual 17 segments of the ventricle compartmentalization, originated from other regions.

Expressions 4.1 and 4.2 depict the total spill-in and maximum local spill-in percentage parameters, respectively.

$$T = \frac{S}{W+S}.100\%\,, \qquad \textbf{(Equation 4.1)}$$

where $S$ is the total activity spill-in from the IVS/BP, and $W$ is the total activity present in the LV wall after the convolution process. It's worth noting that $S$ can be calculated simply as the difference in intensities between the blurred images with and without IVS.

$$L = \max\left(\frac{IVS_i - NIVS_i}{IVS_i}\right).100\%, i \in [1:17]\,, \qquad \textbf{(Equation 4.2)}$$

where $IVS$ is relative to the blurred model with the IVS, and conversely $NIVS$ is the blurred model with no IVS, and $i$ refers to the instance number of the LV segment, according to the AHA 17 compartment model. The $L$ parameter simply captures the single region of the 17 segment model that underwent the most noteworthy change in terms of activity spillover, following the convolution process.

## 4.2.1. The Ventricular Heart Model

The model was designed in order to correspond to an end-diastole LV-RV system, and the reason for that is that the wall is thinner during this phase of the cardiac cycle, which would increase the potential severity of PVE and PVE-related biases. A fusion between two truncated ellipsoids was chosen as the simplified geometry of the model (Germano et al. 2006), (Petitjean et al. 2011). This is pertained in Fig. 4.1.

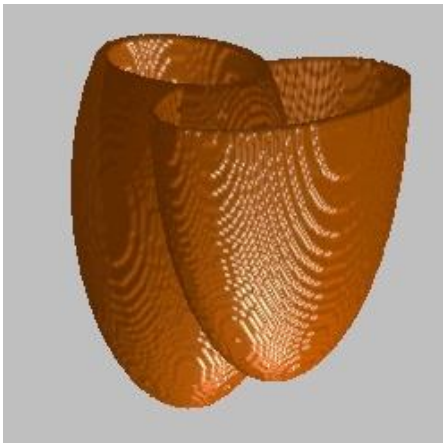

***Figure 4.1*** *- 3D Ventricular Heart Model*

The model was then completed with the incorporation of a BP and a geometrically customisable IVS, located in the referential place where the posterior PM would be. This can be observed in Fig. 4.2.

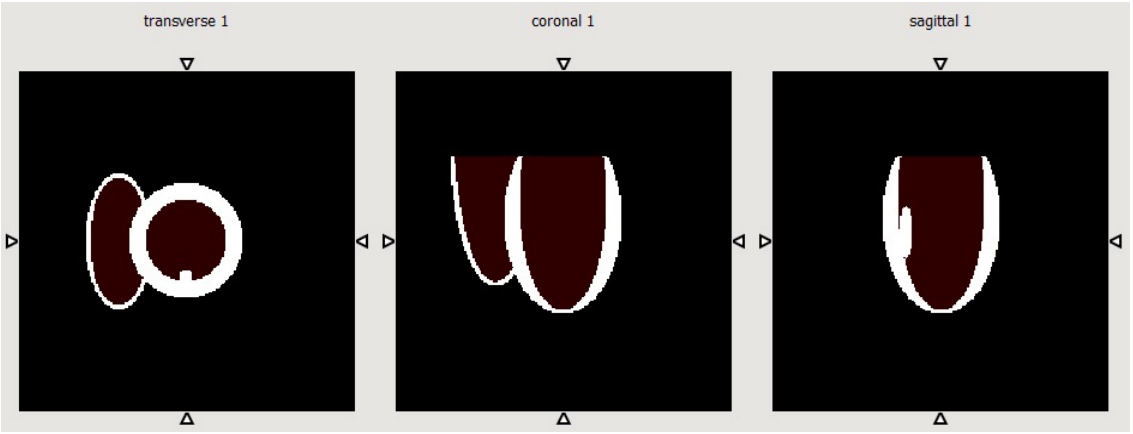


***Figure 4.2*** *- Three referential views of the ventricular heart model. Left) mid-cavity short axis; Centre) horizontal long axis; Right) vertical long axis.*

Following the modelling of the ventricular wall, different thicknesses were imposed, based on the approximate end-diastole thickness of 8 mm, ranging to 11 mm (Bogaert et al. 2005), (Dong et al. 1994). The geometry of the LV cavity was preserved, assuming only a radially exterior myocardial enlargement. This is consistent with realistic cases of concomitant LV hypertrophy and LV dilation conditions (Seiler et al. 1995), (Murphy et al. 2005), harmonising the wall thickness and LV cavity dilation that is characteristic of each one of these cardiomyopathies, respectively (Goktepe et al. 2010).

Another source of variation was related to IVS diameter and distance to LV wall (Spreeuwers et al. 2005), which is related to IVS diversity in terms of geometrical and spatial arrangement (Roberts et al. 1972). Independent studies were performed for IVS diameter for PM and TC, and a conjoint study of both IVS types was made in terms of evaluating the effect of IVS-LV relative wall distance. The different values used for PM diameters were 5, 7 and 9 mm, which are within the reported amplitude of values for these structures (5 to 10 mm) (Spreeuwers et al. 2005). The TC's diameter was assumed to have a general value of 3 mm, based on real MR images observation and the fact that they are known to be smaller than PM, since no solid references could be found in the literature evidencing for quantitative geometrical measurement of the TC. The LV wall distance was varied from a zero wall distance to about 3 mm.

Lastly, BP's PVE influence was also assessed and plotted together with PM's PVE when investigating the effects of LV wall thickness and distance between IVS and LV wall. Based on Pretorius and King (2009), the activity value of 10% of the LV wall's intensity was taken as characteristic of the BP.

Concerning the model itself, further assumptions and simplifications were made, namely a) the uptake was assumed to be equal and uniform across the wall and IVS, since IVS are in fact myocardial protrusions that are assumed to share the same perfusion system as the LV wall; b) IVS uptake was assumed to occur homogeneously across all their physical extension, from base to apex, for the same reason; c) IVS were regarded as ellipsoids (although their actual geometry is known to be more complex and irregular); d) BP's activity was assumed to be constant and uniformly distributed along the LV and RV cavities; e) measurements were done placing an isolated IVS in the general location where the anterior PM is located, adjacent to region 10 of the 17 segment model.

### 4.2.2. First Level Approach Scripts

A number of three main *Matlab* (The Matworks, In., 2012) scripts were created in order to implement the requirements of this first execution part. The contents of these consisted in: 1) the geometrical creation of the model; 2) a function that creates a PSF and takes a 3D image as input in order to calculate the convolution operation between the two; and 3) a function that allows for the PVE quantification of the created model, given the input of the blurred image with IVS and/or BP, another that does not contain the structure which PVE is to be quantified, and a binary mask of the structure where the activity spillover is to be quantified (LV in general terms).

The anatomical model of the ventricle heart, was constructed in parts. The LV was created by generating an ellipsoid, which was further truncated and had the dimensions adjusted in order to have the correct size proportions of a diastolic LV. The dimensions were taken from literature (Bogaert et al. 2005). From this point, the RV was created independently, as an irregular ellipsoid, and then coupled to the LV. The superposition of these two structures was properly removed. The same bibliography as for the LV was taken into account in order to generate the RV geometry and dimensions. Later on, the IVS was created and allocated in an anatomically similar way as the anterior PM. A range of dimensions were imposed to the IVS, in order to represent the TC, PM and intrinsic anatomical variability within each of these structures. Both the dimensions and location of the IVS were determined from (Petitjean et al. 2011). The next steps consisted in the addition of a BP within the RV and LV cavities, and creation of the various model variations that would allow for the PVE quantifications to be performed. This involved the creation of different

arrangements of models with and without IVS and BP. It is worth noting that the script was made to contain parameters that allow for the dimensions of the model's structures to be modified.

The second major script created involved the implementation of a function that generates a PSF modelled as a Gaussian function, which dimensions across the XYZ directions and even the kernel size can be modified according to necessity or will. This function takes a 3D image as input, providing as an output a 3D image with the same size as the input, as a result of a convolution operation between the input and the generated PSF.

The third and last major script created within this first execution step consisted in a function that allows for the full PVE quantification of the ventricle heart model. It takes as inputs the blurred images with and without the structure which PVE is to be quantified (either the IVS or the BP), and the LV binary mask. Following this, the function calculates the total PVE of the structure in question over the LV wall, and divides the LV in 17 segments calculating the individual PVE in each of these, providing quantified PVE values as output. In a certain way, this script allows for the actual determination of the PVE of wanted structures, both in total and local terms.

In addition to the general purpose scripts created above, a number of different functions were created in *Matlab* that aided processing data across all steps of the study. These were essentially 3D adaptations an extrapolations of pre-existing *Matlab* functions, which allowed for the obtainment of custom-made 3D rotation, zero-padding and binarisation, maxima and FWHM localization, as well as reading and writing interfile and text files.

## 4.3. Intermediate Step – Dog Cardiac Data

Following the completion of the evaluation of the IVS PVE influence over the LV myocardial wall, the planned research path for the remaining of the project forked in two different ways. One possibility was to ultimately apply the PVE assessment and subsequent PVC steps on clinical human anatomical data, in order to have a better assessment of how the PVE would occur in progressively more complex and realistic models. The other option to potentially explore was the possibility of having access to myocardial perfusion ($^{99m}$Tc sestamibi) dog SPECT data, as well as the correspondent anatomical images (obtained through CT of the excised hearts) and the mapped ground truth activity present in the dissected cardiac tissues. This approach seemed quite promising as it would allow for the possibility of performing PVC techniques on data which ground truth activity was known, hence permitting the validation of the PVC routine against the true activity distribution on the object, which would prove quite interesting from a possible publication point of view.

In order to assess the possibility of exploring this latter path, a set of criteria was set: 1) there must be a geometrical similarity between the excised and *in vivo* hearts – PVC routines are object dependent and often based on anatomical data, which is obtained *in vivo*. A non-geometrical correspondence between the anatomical image and the corresponding functional data would incur in a major difficulty in implementing this approach. It is worth reiterating that although the functional images corresponded to the *in vivo* hearts, the CT modality was used to acquire the data from the hearts after they were excised; 2) the possibility of implementing an adequate relationship between the activity distribution of the hearts observed in the images and the correspondent values measured in the laboratory – otherwise it would not make sense to attempt this approach; 3) the amount of time estimated to complete the milestones associated with this approach, seeing that the project could only be performed during a maximum period of 6 additional months.

Ultimately this research path ended up presenting itself as unfeasible, as it will be made clearer in section **5.3** ahead.

Therefore, the study's course of actions engaged into the further assessment of PVE influence produced by IVS, using more realistic model approaches.

## 4.4. Second Level Approach – Realistic Reconstruction

In this second level execution part the main goal was to reproduce the main PVE study performed on the previous level, elevating it into a more realistic framework by replacing the *Matlab* emission image simulation generation step with a proper PET image acquisition simulation, using a software named Software for Tomographic Image Reconstruction (*STIR*) (Thielemans et al. (2012)).

The enhanced realistic nature obtained using this software was due to proper simulations of realistic projection based image reconstructions, with a broad option in terms of the preferred type of reconstruction routine. Other effects such as noise, scatter and random counts, total number of counts, scanner efficiency, among others were also more accurately depicted.

However, this more accurate approach contained a number of factors that needed to be validated in order to ensure that the method could be properly quantified and comparable to the previous approach.

Given the aforementioned, this second batch of results was organized in terms of three logical sections: 1) the first part consisting ofn a set of studies aiming to improve the realistic nature of the method – by performing studies aimed to determine the most realistic total number of counts to assign to the model, to determine the proper amount of scatter and random counts to add to the simulation, and to determine the amount of reconstruction averages necessary to keep the reconstruction noise at acceptable levels; 2) the second part consisting of the validation of the whole procedure and quantification of potential sources of discrepancy – where studies were made in terms of ensuring that the overall blurring in *STIR* would be equivalent to the one applied in *Matlab*, quantifying the variability in the image blurring in terms of image spatial displacement across the FOV and total number of counts (count magnitude), and determining the threshold number of subiterations from which the OSEM reconstruction stabilizes; 3) and third and last part – where the PVE is assessed in terms of different reconstruction routines, and the results are ultimately compared to the respective ones in the previous level approach.

### 4.4.1. Second Level Approach Script

Although the geometrical model to be used in the study remained the same, the approach had to be changed for obvious reasons, as the main tool to use when performing the study in this second execution part was *STIR*, as opposed to *Matlab*.

The process inherent to this approach was coded in two major cycles, one that converts the input image into a sinogram map, comprising the projection stage; and a second cycle that is further divided into two independent frameworks, which consisted in a FBP and an OSEM reconstruction

routines. Each of these could be repeated a pre-determined number of times, being able to account for reconstructions with different noise seeds.

The reconstruction output would consist in an image object with a definable voxel size and with an *Interfile* file format.

Although the whole aforementioned process took place under the *STIR*'s framework, in order for the first and second level approaches' results to be fully comparable, the images needed to be quantified under the same outline, and hence in the same file format. Thus, a workaround was defined in a *Matlab* environment, where a simple script was created in order to convert a definable number of *Interfile* input images into a single *.mat file, which can be read, saved and stored in a *Matlab* environment.

In order to have an appropriate observation of the results obtained from the *STIR* routine, and prior to the import of these outputs to *Matlab*, a quality check step was introduced at this stage, that allowed to review whether the results produced were comprehensive or not. Due to the time consuming nature of the simulations run, it was useful to introduce a testing phase before converting large amounts of data into a *Matlab* environment. This was accomplished in the form of a visual check and required a previous step of testing different softwares for image visualization. Softwares such as *Mango* (Lancaster & Martinez), *ImageJ* (Ferreira & Rasband, 2012), *Slicer3D* and *MRIcron* were tested, and although the process of selection of an appropriate image viewer software would fall outside of the scope of this work, the preferred software was *AMIDE* (Loening & Gambhir, 2003), due to its simplicity, versatility in terms of image formats and swiftness in loading large sized files.

Following the validation of the approach, quantification of all sources of bias, implementation of the reconstruction routines and conversion to a *Matlab* environment, the IVS activity spillover to the LV was then determined, in total and local terms, and then compared against the correspondent values obtained in the previous simpler approach.

## 4.5. Third Level Approach – PVC Validation

The third level execution part had the goal of assessing the actual discrepancy in PVC routines that do not take IVS into account.

The main tool initially projected to be utilized for this approach was a previously created iterative algorithm for PVC (Thomas, 2012), designed in the C++ language, that allowed for the selection of a range of different PVC methodologies, upon the input of an emission image, a 4D image containing all the regions of interest to be accounted for in the correction procedure, the selection of the PVC method to use, and the pre-determination of the number of iterations to implement during the routine (in case the latter applies, as not all PVC methods have an iterative character). Further information regarding this PVC code can be found elsewhere (Thomas, 2012).

The first stage of this execution part was based on the validation of the PVC routines, using an image with a pre-determined and well known blur, and applying the respective PVC algorithm in order to retrieve the initial activity distribution. This was performed in order to validate the PVC methodologies to be used.

Following a proper validation of the PVC methods, the difference in results in terms of recovering a model image with IVS and another without the presence of these structures was determined, in

order to ascertain the error expected to be obtained when one does not take the IVS into account, when performing PVC.

This IVS influence in the PVC was taken a step further, by the attempt to use real anatomical images. However, prior to this two different routines of automatic cardiac segmentation were tested in clinical data, one being an atlas based segmentation and another being an active contour based segmentation technique. Following the comparison and validation of the more adequate of these two approaches, the goal was once again to assess the error produced by not accounting for IVS in the PVC process.

Ultimately, a full comparison of total and local IVS influence across all the approaches utilized during this study was performed.

# 5. *Results and Discussion*

## 5.1. Overview

In a similar organization as in the previous section, the current ***Results and Discussion*** section is mainly divided in four parts: 1) simple blurring process evaluation, where the IVS influence is compared against the BP's one, in light of a number of different variability factors. The amount of activity spillover from the IVS and BP is quantified in local and total LV myocardial wall terms; 2) dog cardiac data evaluation, where the possibility of following a certain potentially promising research approach was assessed; 3) realistic reconstruction approach evaluation, where the first IVS assessment study was elevated into a more realistic framework, with the utilization of a proper software for tomographic image reconstruction; 4) PVC implementation, where the IVS influence was tested following PVC routines applied on images with and without the consideration of IVS as independent structures.

Regarding the first level of PVE assessment, the blur produced by the IVS was determined, as well as the PVE produced by the BP, in order to facilitate a comprehensive comparison between the effects produced by both regions. The last part of this first execution set of results was obtained in order to validate the model and account for parameters that may cause the PVE to vary in a realistic set, such as the LV wall thickness, IVS size and relative position of the IVS in respect to the LV wall.

The cardiac dog data sub-section comprises essentially the evaluation of available CT data of excised dog hearts, in order to assess potential complications with regards to geometry deformations and tissue damage that could impede a smooth approach to this sub-study in terms of allowing for a proper co-registration between the available anatomical and functional dog data, which could in turn affect the performance of proper PVC methodologies.

The results in the realistic reconstruction approach sub-section were essentially spread into three distinct parts, 1) the first to improve the realistic character of the study; 2) the second consisting in the validation of this procedure in order to ensure it would be comparable to the correspondent set of results from the normal blur procedure; 3) and a third step to fully implement the comparison routine in the model.

Consistency between the first and second execution steps, using *Matlab* and *STIR*, respectively, was kept in the situations where this was possible. In the remaining cases, a quantification procedure was used in order to account for variability.

The third level approach consisted in validating the whole set of PVE assessment studies by actually implementing PVC routines, allowing both the validation of the PVE in the model and in

the anatomical heart. This approach comprised the obtainment of the following results: a) validation of PVC routines against the ventricular heart model; b) IVS PVC relevance study; c) attempt to validate PVC routines against real clinical data – and associated choice of LV segmentation method, for PVC purposes.

The next sections of this chapter will therefore be dedicated to describing the aforementioned results.

## 5.2. Simple Blurring Study

The first set of results were regarding the PVE assessment of simulated emission images obtained using a simple convolution method, consisting in the blurring of the ventricle heart model with a system's symmetric PSF of 10 mm FWHM. The goal of this sub-section was to quantify the PVE produced by IVS, and to compare it against the BP's activity spill-over on the LV wall. In addition, studies to evaluate the change in PVE with the internal ventricular structures' diameter, distance to the left-ventricular wall and left-ventricular wall thickness were carried out.

Concerning the IVS diameter study, total and local spill-in of activity to the LV wall was evaluated. In this study, four different diameter values were used to illustrate IVS, one depicting a general TC diameter (3 mm) and the other three with 5, 7 and 9 mm, characterizing a range of typical PM diameters. Fig. 5.1 shows a graphical representation of the IVS diameter study, in terms of the local PVE produced. The local BP PVE influence over the same region was quantified as well, based on a representative BP activity of 10% of the original activity assigned to the LV (and IVS).

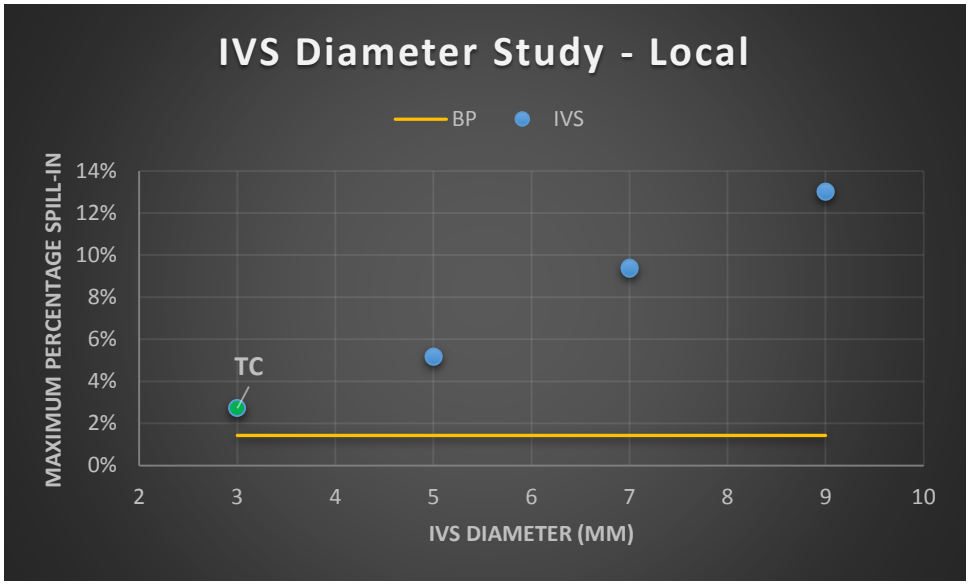


***Figure 5.1*** *- IVS Diameter Study*

Evaluating the IVS diameter variation study, the virtually linear pattern exhibited is consistent with what would be expected, since the greater the dimensions of the object, the more the activity spilled to the wall, seeing that the activity concentration remains the same, despite the change in

the object's volume. This trend is typical both in local and overall LV-wall terms (not shown). From Fig. 5.1 it can also be retrieved that purely from the point of view of local PV effects, the IVS – including the TC - exert a blurring effect that is more significant than the one produced by the BP. The local PVE values ranging from around 3% to approximately 13% were recorded for the typical dimensional range of IVS. On the other hand, the total PVE contribution of the IVS over the LV wall was expectedly lower, and recorded to range from 0,1% to 0,5% of the total activity of the wall. These values were measured to be one order of magnitude lower than the total PVE effect produced by the BP – approximately 3,1%, in the same conditions.

The IVS was inserted at an average distance of 2 mm from the LV wall. It is worth noting that this distance was computed in respect to the medial section of the IVS, since the base of the structure is connected to the wall and the apex is free at the opposite end, the latter comprising the most distanced IVS portion.

Regarding the study assessing IVS to LV wall distance variation implications, representative TC and PM diameters of 3 mm and 5 mm were taken, respectively, as these values are sufficiently close to appreciate their synchronized variation, and illustrate the effect of distance to the LV wall in both TC and IVS. The study was carried out as explained in section **4.2**, where the PVE of IVS was plotted for IVS-wall separations of 3, 2, 1, and 0 mm. The constant PVE of the BP was also superimposed in Fig. 5.2, which completes the depiction of the findings in this sub-study, in local terms.

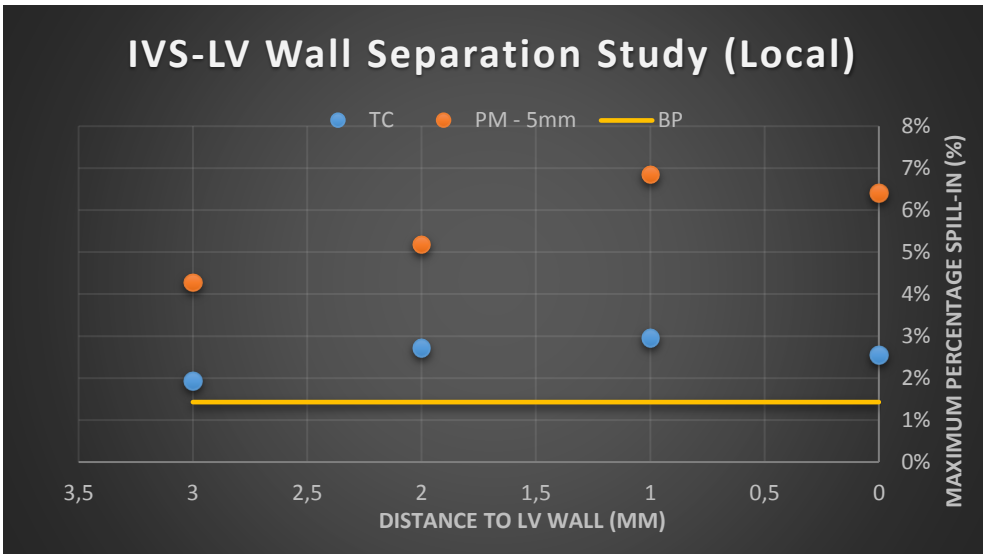


***Figure 5.2*** *– Local IVS-LV wall separation study*

In the previous Fig. 5.2 one can clearly observe that PM PVE is more sensitive to LV wall separation than TC, which is inherently related to its diameter.

An interesting result is that even though wall proximity generally produces an increase in PVE influence, in both the PM and TC cases, when the distance becomes zero there is an actual decrease in the PVE. This is mainly because initially, as the structure approaches the ventricle wall, the amount of activity that spills from the structure to the wall increases (given the current simulated reconstruction blur of 10 mm FWHM). However, in the model, as the distance between the structure and the wall decreases to a critical value, part of the IVS fuses with the LV, decreasing its volume and hence its total activity, which causes the PVE over the wall to decrease.

Therefore, in this case there is a complex relationship between the decrease in the IVS-LV wall distance and the decrease in the dimensions of the IVS. Another important note is that the TC still exerts a PVE influence which is more significant than the BP's in local terms, even at 3 mm from the LV wall.

The PM's maximum local influence was detected to vary at the measured distances between the values of 4,3% to 6,9% of the activity of the wall segment, whilst these values ranged from around 2,0% to 3,0% in the case of TC.

Total spill-in evaluation was also performed, showing virtually the same visual pattern as in the corresponding local spill-in study. The only difference resided on the fact that the magnitude of the PVE produced by the IVS decreased significantly when taking as reference the whole LV as opposed to just a segment of this structure, as evidenced in Fig. 5.2.

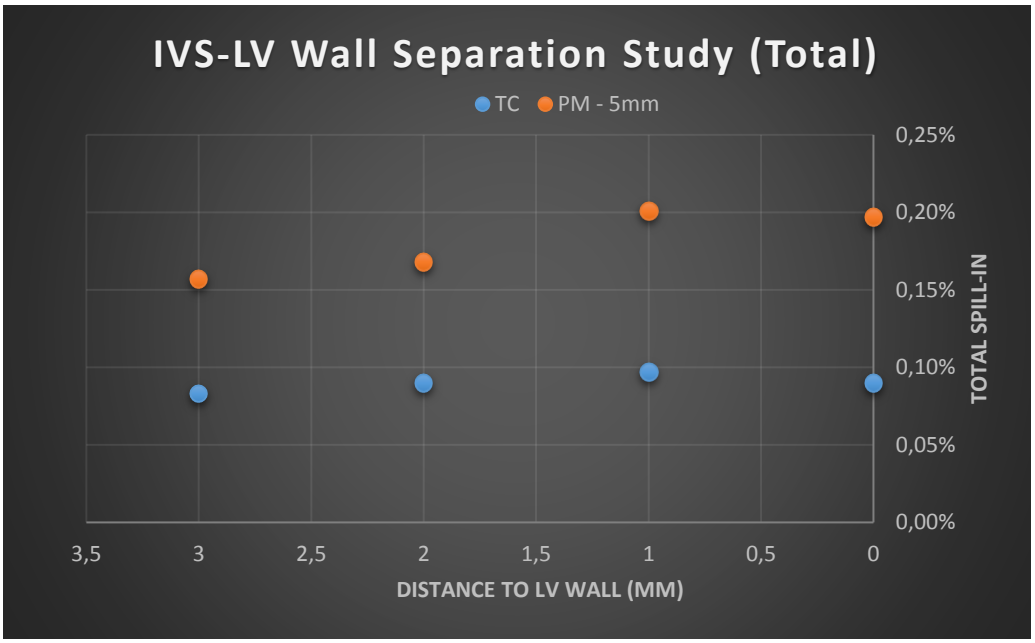


***Figure 5.3*** *- Total IVS-LV wall separation study*

The variation in the pattern of activity contribution from structures within the ventricle cavity is quite similar when the study is shifted towards a total LV wall PVE assessment. Only the PVE values change. As observed in Fig. 5.3, the IVS exert a total PVE in the order of magnitude of 0,1% of the activity of the myocardium, whereas the BP exerts an effect which is one order of magnitude higher (approximately 3,1% - not shown). The observed decrease in IVS PVE relevance in total terms is in accordance with the fact that these structures are only located in an isolated region of the endocardium, whilst the BP was modelled to fill all the available volume within the LV cavity, hence exerting its PVE contribution over all portions of the LV wall. The total PVE ranges observed were of 0,16% to 0,20% for the PMs, and 0,08% to 0,10% for the TCs.

Figs. 5.4 and 5.5 show PVE results for varying LV wall thicknesses. A single IVS with the size characteristics of a 7 mm diameter PM was modelled and fixated at a general 2 mm distance from the wall. The BP's PVE was also plotted as a function of LV wall thickness.

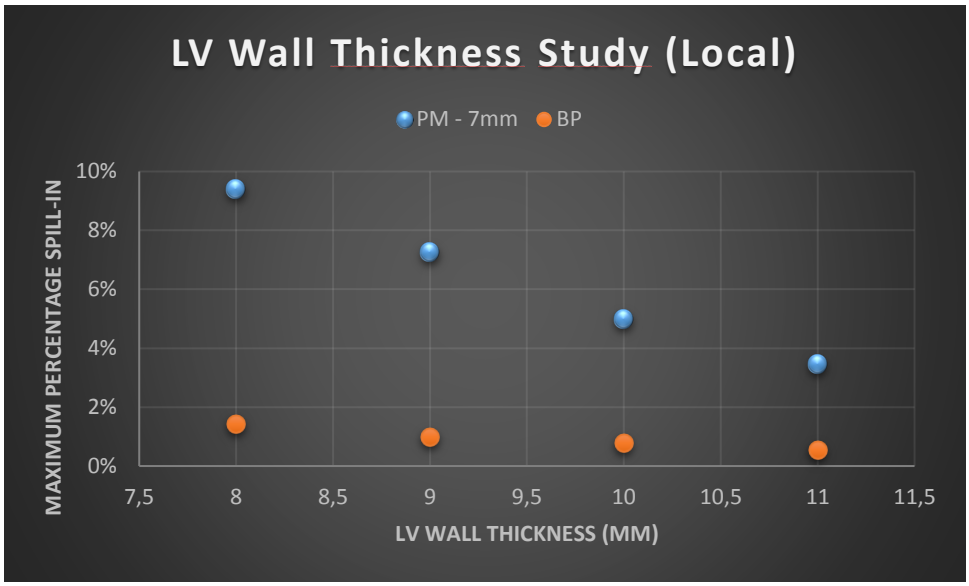


***Figure 5.4*** *- Local LV wall thickness study*

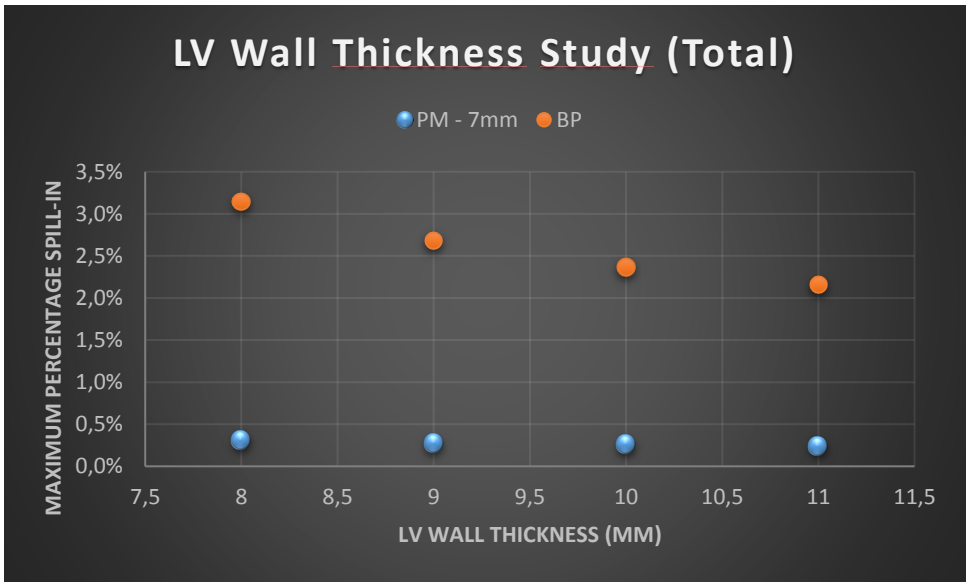


***Figure 5.5*** *- Total LV wall thickness study*

Both Figs. 5.4 and 5.5 show a similar decreasing trend of total and local spill-in, as a function of wall thickening. The non-linear variation can be explained by the fact that the change in wall thickness incurs in a volumetric alteration of the region where the spill-in is being calculated, which in turn determines the calculation of the PVE. From the point of view of the most typical diastolic LV wall thicknesses (8 to 11 mm, as per Dong et al. 1994, and Bogaert et al. 2005), it can be observed that the range of IVS PVE values was of around 3.5% to 9.4% in local terms, and 0.25% to 0.30% in total terms. On the other hand, the BP manifested a PVE range of approximately 0.5% to 1.4% in local terms, whereas the total effect was measured to be of around 2.2% to 3.1%.

The studies performed in this section provided with enough insight regarding the PVE assessment to allow the creation of Table 5.1. This comprises the possible ranges of PV effects produced by each IVS and BP, under plausible conditions.

***Table 5.1*** *- IVS and BP PVE Summary from simple convolution blurring study*

| Structure | Maximum Local Spill-in Percentage | Total Spill-in Percentage |
|---|---|---|
| BP | 0.5 – 1.4% | 2.2 - 3.1% |
| PM | 4.7 – 14.1% | 0.2 - 0.5% |
| TC | 2.4 – 3.0% | 0.07 - 0.10% |

The PVE produced by IVS was depicted in the form of ranges in order to portray the extreme values of PM, TC and BP partial-volume influence, allowing for a clearer observation of the full extent of their impact over the LV wall. While the BP range was fully obtained from the LV wall thickness study, the PM and TC ranges were obtained from a mixture of extreme values obtained from the LV wall thickness and LV wall-IVS distance studies.

Although the BP's total PVE influence is expectedly more significant, it has to be taken into account that the IVS PVE assessment was performed for one single structure only, which leads to the realisation that the conjoint IVS influence is relative to two PM and a typical number of approximately ten TC disposed along the LV wall (estimate taken from visual observation of a number of anatomical cardiac images). This overall effect, combined with the fact that IVS produce a more significant local effect, indicates that IVS may potentially have a significant impact in terms of activity spillover to the LV wall, by taking the corresponding influence of the BP as a reference. In any case, due to the simplicity inherent to this convolution-based approach, a more realistic study is necessary in order to fully compare the PVE produced by IVS and the BP.

## 5.3. Cardiac Dog Data Study

Following the completion of the first stage of PVE assessment, the subsequent course of actions consisting in exploiting the possibility of performing a PVE and PVC assessment on myocardial perfusion dog SPECT data, CT of the correspondent excised heart, and ground truth mapped activity measured in different regions of the *ex vivo* cardiac tissue.

It is worth recalling that the goal of these assessments was to decide on whether to follow through with this path of research or not. The evaluation of the suitability of this study path was performed in three stages, as indicated in section **4.3**.

In order to test the geometrical suitability of the anatomical data, a plurality of CT images of excised dog hearts was assessed.

Figs. 5.6 to 5.7 below illustrate the suitability evaluation of *heart #1*.

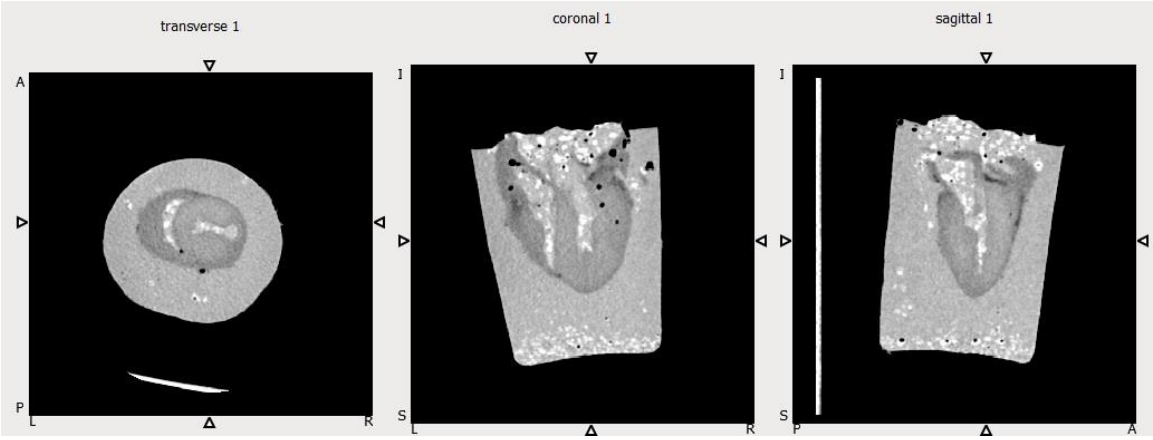


***Figure 5.6*** *- CT scan of excised dog heart #1 – 3 reference views*

Fig. 5.6 allows the identification of collapsed ventricular cavities, as well as an abnormally thick myocardium, even in the standards of dog anatomy, suggesting a pattern of hypertrophic cardiomyopathy (Kumar et al. 2010).

Observing the same heart at a more superior axial level, shown in Fig. 5.7, allowed for the observation of the existence of significant tissue damage, namely a perforation at the anterolateral region of the LV.

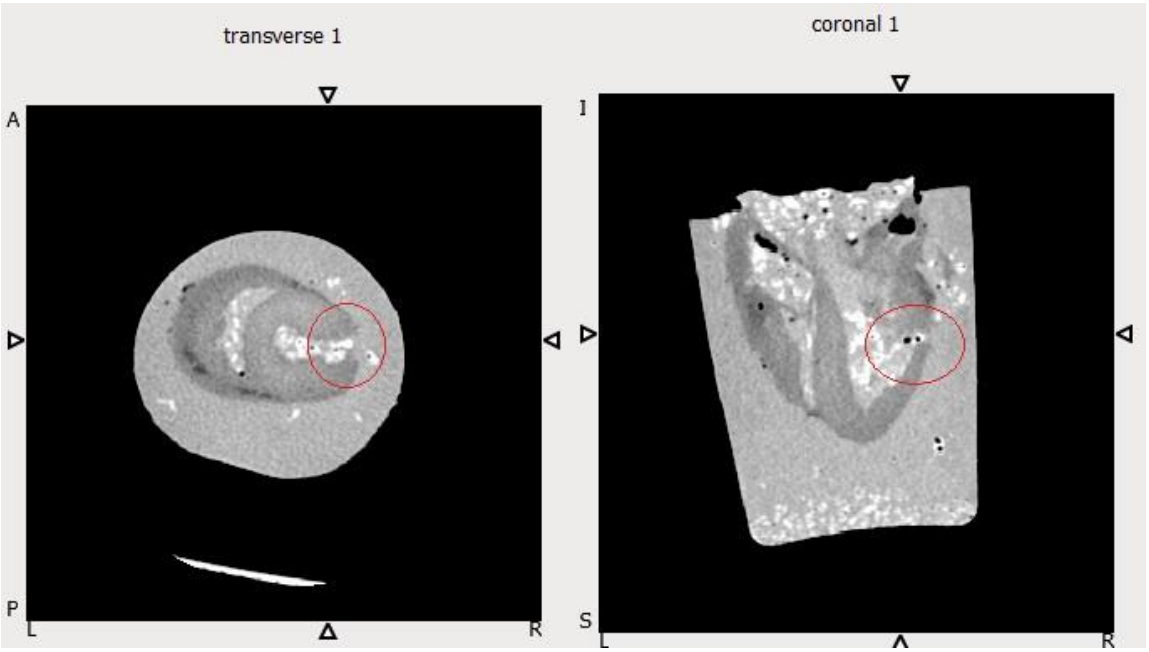


***Figure 5.7*** *- Zoomed view of excised dog heart #1 – more superior axial and coronal views*

Conversely, an investigation of regions located at the apical region of the *heart #1*, illustrated in Fig. 5.8, revealed that the heart contains additional regions where tissue damage is evident. This has been highlighted in the same figure.

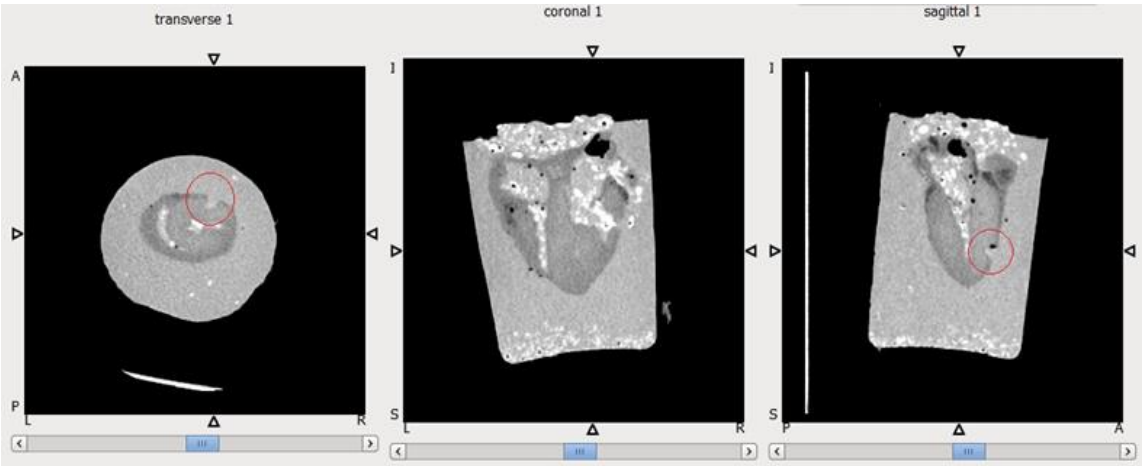


***Figure 5.8*** *- Apical location of excised dog heart #1 - all 3 reference views*

Therefore, given the geometrical collapse of the ventricular structures and significant tissue damage observed in *heart #1*, it can be assumed that this organ is not suitable to be effectively used in a PVC methodology, since it is anticipated that the co-registration step between the anatomical and functional data will result in a significantly arduous task. Also, the damaged tissue regions would also cause problems during the blurring compensation step.

Following the assessment of the suitability of *heart #1*, *heart #2* was also evaluated under the same standards. Figs. 5.9 to 5.10 present the main findings of this evaluation.

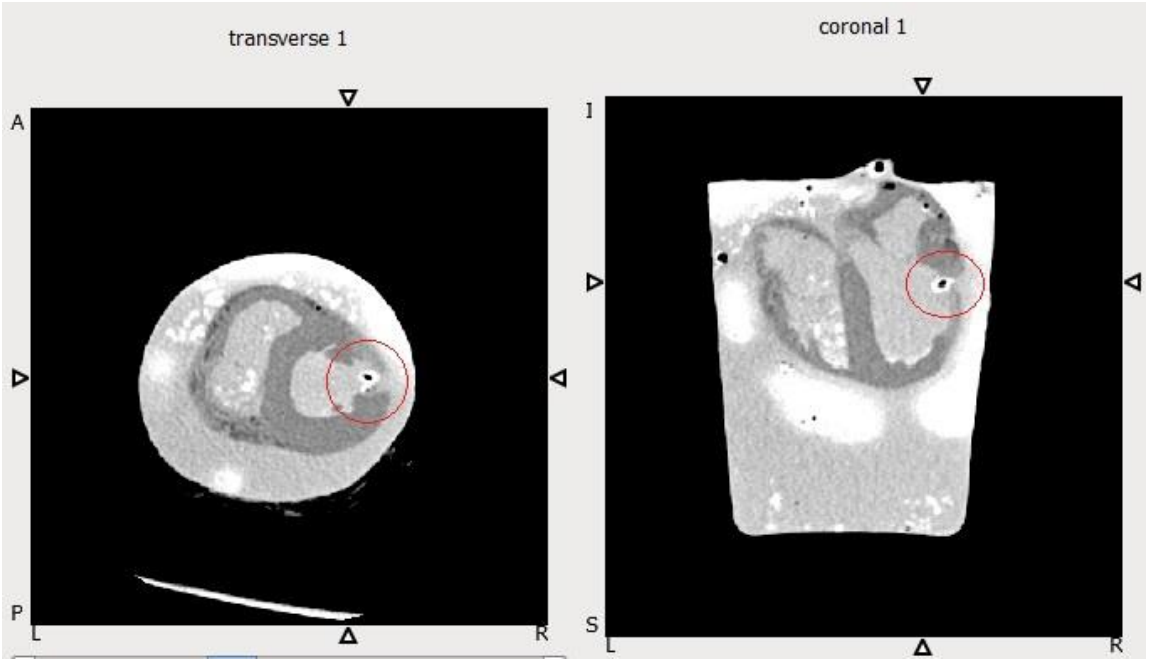


***Figure 5.9*** *- Zoomed view of excised dog heart #2 – axial and coronal views*

Fig. 5.9 evidences either an abnormal thinning or a perforation of the antero-lateral region of the LV, or even a combination of the two.

Additionally, Fig. 5.10 of *heart #2* illustrates a similar tissue damage pattern as in Fig. 5.8, where a fraction of the myocardium on the anterior left ventricular region appears to be obliterated.

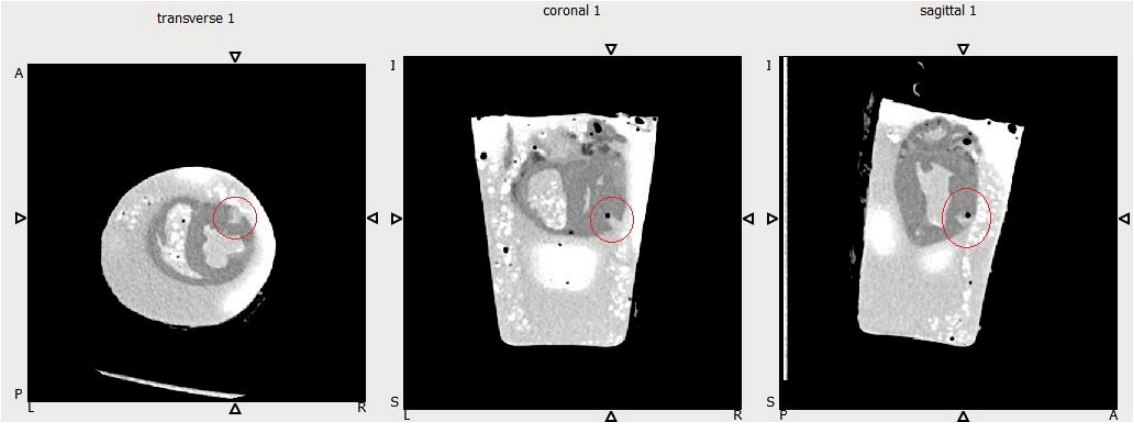


***Figure 5.10*** *- Apical location of excised dog heart #2 - all 3 reference views*

Fig. 5.11 below illustrates an additional depiction of heart *#2*.

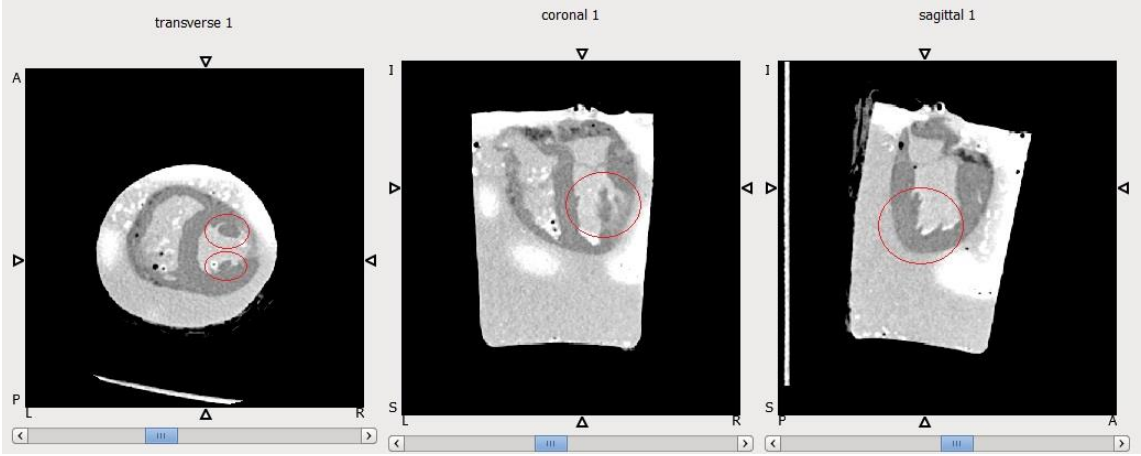


***Figure 5.11*** *- Additional representation of excised dog heart #2 - all 3 reference views*

Despite the tissue damage evident in the previous Figs. 5.9 and 5.10, *heart #2* presents with a good geometry, similar to the *in vivo* one, with no cavity collapse, apparently normal myocardial wall thickness and evident presence of internal ventricular structures, as shown in the present Fig. 5.11. In any case, the damaged tissue regions in heart *#2* would be expected to cause problems during the deconvolution step of a PVC routine.

The following heart (*heart #3*), was also evaluated under the same framework, and the evaluation for physical abnormalities led to the findings evidenced in Fig. 5.12.

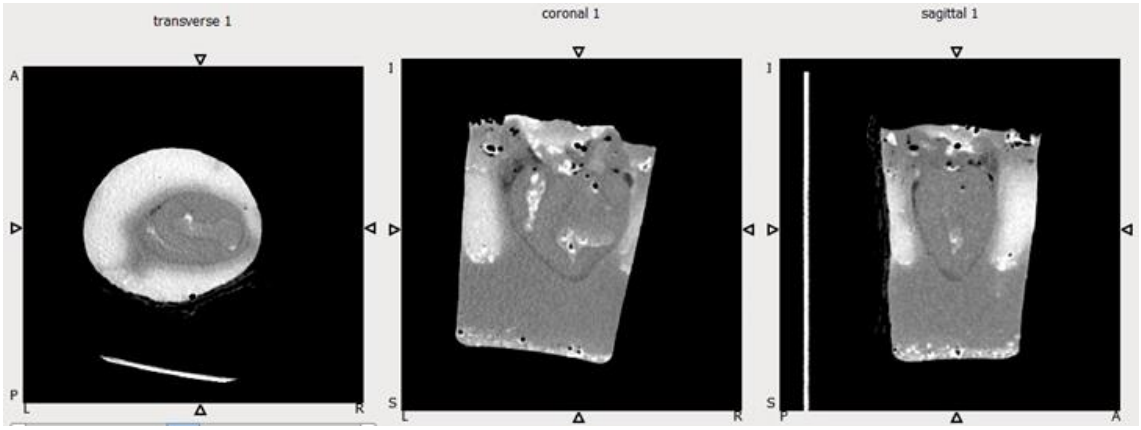


***Figure 5.12*** *- CT scan of excised dog heart #3 – 3 reference views*

Fig. 5.12 illustrates the non-ideal contrast associated with the image of *heart #3*, as well as an abnormal geometry of the ventricular cavities, possibly as a result of the excision process. The anatomy of the heart suggests a geometry which is significantly discrepant in respect to the *in vivo* case.

The final heart (*heart #4*) was evaluated as per Fig. 5.13.

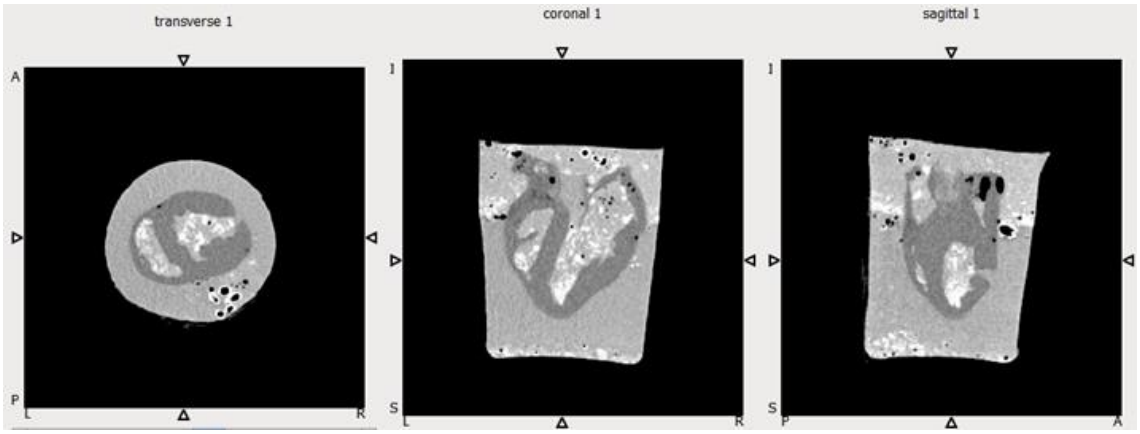


***Figure 5.13*** *- CT scan of excised dog heart #4 – 3 reference views*

Where it can be assessed that although the geometry of the excised *heart #4* is similar to the *in vivo* case, there is evidence of significant tissue damage, in the form of a myocardial perforation. The difficulty in distinguishing internal ventricular structures is also a negative point in the assessment of the suitability of this heart image for PVC studies.

An overview of the obtained results leads to a number of observations. The anatomy/geometry of the dog heart is very similar to the human's cardiac apparatus. Despite the slightly different proportions, they are essentially similar in an anatomical image point of view. The set of available excised CT hearts generally presented with substantial tissue damage. Apart from this, even though some images presented with good geometry (non-collapsed hearts), their shape is probably different to the *in vivo* case, which means that some degree of co-registration would probably still be necessary. In line with this, the IVS observed in the excised hearts are probably in a different orientation/geometry compared to the *in vivo* scenario. In any case, the heart that showed to

preserve the most amount of *in vivo* characteristics was *heart #2*, although still presenting with a certain amount of tissue damage.

However, in addition to the non-ideal results obtained in the geometric suitability study, no logical correspondence was found in terms of the mapped activity of the dissected hearts and the correspondent functional images.

This, added to the fact that a proper approach in which a PVC methodology would be implemented would require a co-registration step between the *in vivo* functional heart and correspondent excised anatomical image representation, taking into account the fact that the excised anatomical data, being the reference object for the registration, was quite deformed, prolapsed and damaged, this would lead to the assumption that the necessary image processing (registration process) would have to be non-rigid and complex in nature, not to mention uncertain in terms of the final results, which would incur in spending a significant amount of time and effort in order to fully test and optimise this approach. The time-frame projected for this cardiac dog data approach was, in the best of scenarios, of around 9 months, which would fairly surpass the time boundaries available for the fulfillment of the project (approximately 5 months left).

Following this evaluation, the decision was to not follow with this option, and carry out with the clinical human anatomical data approach.

## 5.4. Realistic Reconstruction Study

In this second execution part the main goal was to reproduce the PVE measurements performed in section **5.2**, using *STIR*.

The enhanced realistic nature obtained using this software was expected to replicate effects such as noise, reconstruction type, scatter and random counts, realistic total number of counts, scanner efficiency, among others, during PVE assessment exercises.

However, this more accurate approach contained a number of factors that needed to be validated in order to ensure that the method could be properly quantified and comparable to the previous approach.

Given the aforementioned, this batch of results was organized in terms of three logical sections: the first part consisting in a set of studies aiming to improve the realistic nature of the method; the second part consisting on the validation of the whole procedure and quantification of potential discrepancies; and third and last part, where the PVE was assessed in terms of different reconstruction routines, and the results were ultimately compared to the respective ones in the previous execution part.

### 5.4.1. Enhancing the realistic nature of the model

This first step was executed both in order to approximate the model to reality, and to define the model's initial parameter set-up, such as the count magnitude of the original cardiac phantom object and the amount of random and scatter counts generated during the reconstruction routine. The relevance of this phase resided in the fact that all the further steps were dependent on this

initial study and different results would be obtained in case this initially determined parameter set-up would have taken different values.

#### 5.4.1.1. Determining the Initial Image Count Magnitude

This study had the goal of assigning a typical number of counts from a $^{82}$Rb-chloride cardiac study, performed on a GE Discovery PET-CT machine, to the simulated model, since the specifications of this GE scanner were used in *STIR's* routines applied in this study. This would also be the scanner from which the clinical data for the third and final major execution part would be obtained.

In order to perform the required image reconstructions associated with the model, different initial count magnitudes were assigned and the one that presented with the visual aspect that most resembled that of a real $^{82}$Rb-chloride cardiac perfusion image would determine the count magnitude of the voxels of the generated model, with uniform activity within each represented anatomical ROI.

Prior to the commencement of the study, two major points needed to be stated. One was that the typical number of counts produced in a cardiac perfusion $^{82}$Rb-chloride PET acquisition, in a GE Discovery VCT scanner (Teräs et al. 2007), is of the order of *10E7* to *10E8* counts, which was determined upon inspection of the PET *total_counts* DICOM tag – (0009,10A7) from a plurality of real clinical data. The DICOM tag was determined as corresponding to the total number of counts in the study, using the GE Discovery DICOM Conformance Statement (GE Healthcare (2005)). It is also relevant to emphasise that the typical number of scatter and random counts is of around 10% to 40% (Paans et al. 1989), which means that the inclusion of these counts should not change the order of magnitude of the total number of counts in a clinical image. For this reason it was chosen that the study involving the determination of the initial count magnitude of the model would be performed without taking scatter and random counts into account. These would be added at a later stage, after the determination of the total number of counts to assign to the model.

In order to determine what initial values to assign to the myocardium activity, as to obtain a realistic model in terms of reproducing the typical total number of counts produced in a $^{82}$Rb-chloride cardiac perfusion examination, different OSEM reconstruction routines were implemented, with different intensity values assigned to the original image's myocardium voxels. The resulting reconstructed images were then assessed in terms of their total number of counts, as well as their visual similarity to corresponding clinical data.

Different simulations in which voxel intensities assigned to the myocardium, from 0.001 to 1, were implemented. The visual results obtained for the voxel count magnitudes of 0.01 and 0.1 are illustrated in Fig. 5.14, since these presented with a visual aspect that most resembled real clinical raw data.

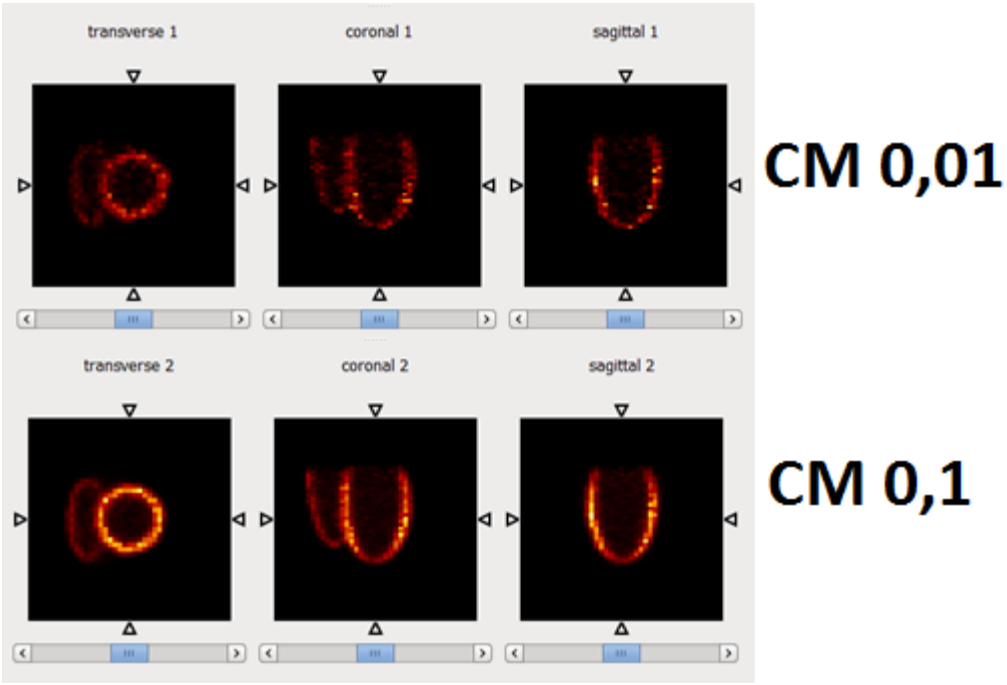


***Figure 5.14*** *- OSEM reconstructions of model images with initial voxel intensities of 0.01 (top) and 0.1 (bottom) - all 3 reference views*

In the previous Fig. 5.14 it can be observed that each voxel intensity count magnitude choice produces a final image with slightly different patterns. Upon comparison with real clinical equivalent raw images it was noted that the count magnitude that produced the most similar pattern to the clinical case was the one with the maximum voxel intensity value of 0.01. The OSEM reconstructions illustrated above incur in a total number of counts in the image in the order of *10E5* and *10E6*, respectively. This means that the produced total number of counts is 2 orders of magnitude lower than the expected *10E7* value for real clinical images. This can be explained by two different reasons. One is the fact that the model does not contain the proper amount of anatomical structures that have uptake as in a real clinical environment set, where the remaining of the heart tissue, blood and extracardiac regions such as the liver would have had a considerable uptake contribution, taking into account the $^{82}$Rb-chloride normal biodistribution (Hunter et al. 2015), as well as the circulating blood. The other reason is that the model was implemented without random and scatter counts, which although are expected to contribute solely in a proportion of approximately 10% – 40% of the total activity present in an image, it would still add up to the current count magnitude calculation. The two reasons given previously would explain the deviation in the total number of counts between the model and the clinical set-up. The final decision was to embrace the simplicity of the model and take into account a maximum voxel intensity of 0.01, which incurs in a total number of counts in the order of *10E5*.

#### 5.4.1.2. Adding Random Counts and Determining the Amount of Scatter

Subsequent to the pre-set of the total number of counts, the number of random counts were added in the representative amount of 10% of the total, since this value is typical in a clinical environment, although higher values of this noise contributing source of counts can be potentially

produced (Paans et al. 1989). The number of scatter counts are calculated automatically by the software, depending highly on the distribution of activity in the object and the attenuation media. Typical percentages for the number of scatter counts in uncorrected images approximates 10% – 30% (Paans et al. 1989), although it should be expected that this contribution would be quite lower in the current model simulation, since there is a smaller amount of attenuation and scatter media.

In any case, the total number of counts, including random and scatter counts, is still expected to amount to the order of magnitude of *10E5*, for this model.

The procedure consisted in performing a simulation of a model containing a ventricle heart template and blood pool, with no atria and no additional extracardiac structures. The amount of 10% of random counts was added and the number of scatter counts determined, simply by performing a simulation without the option of adding scatter, and then performing another one with this noise contributing effect, computing the difference between the total number of counts subsequently.

The below Table 5.2 indicates the amount of counts obtained following reconstruction routines with and without random and scatter counts. The percentages of these additional counts were then computed.

***Table 5.2*** *- Number of Total, Random and Scatter counts determination summary*

| | No Scatter, no Randoms | With Randoms Only | With Scatter Only | Scatter+Randoms |
|---|---|---|---|---|
| **# of Counts** | 159193 | 175110 | 159536 | 175437 |
| **% Contribution** | N/A | + 10% | + 9% | + 19% |

It is noticeable that the scatter fraction is lower than realistic values, which are of the order of 10% – 30% instead of 9%, as mentioned previously (Paans et al. 1989). This is most certainly due to the fact that the model is very limited in terms of attenuation and scattering media.

#### 5.4.1.3. Profile averaging study

This study originated from the fact that after a reconstruction routine, the output image would be obtained with a significant level of noise, mostly due to the low total number of counts resulting from reconstructing the model (*10E5*), which would often cause the reconstructed image to possess higher valued peaks in respect to the original image (as shown in Fig. 5.16).

This pattern was observed in both FBP and OSEM reconstructions, and the adopted solution was to average same-type reconstructions over different noise realisations in order to get an estimate of the mean reconstructed image. This study was therefore performed to assess the most appropriate number of simulations to perform.

Fig. 31 depicts a coronal view of the ventricle heart model, and the blue line across it illustrates the region where a profile was taken, both in the original image and in each of the averaged reconstructed images, in order to quantify the levels of noise.

***Figure 5.15*** *- Axial 1D profile location illustration*

Figs. 5.16, 5.17 and 5.18 depict the results of using different numbers of averages.

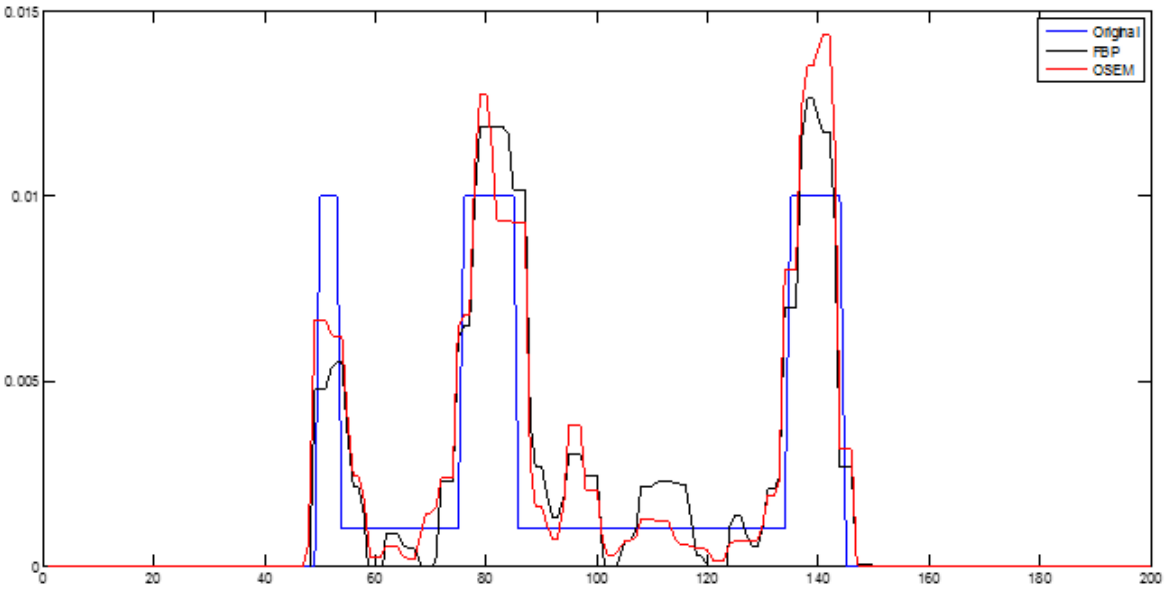


***Figure 5.16*** *- Cardiac model profile averaging. Number of noise realizations = 2*

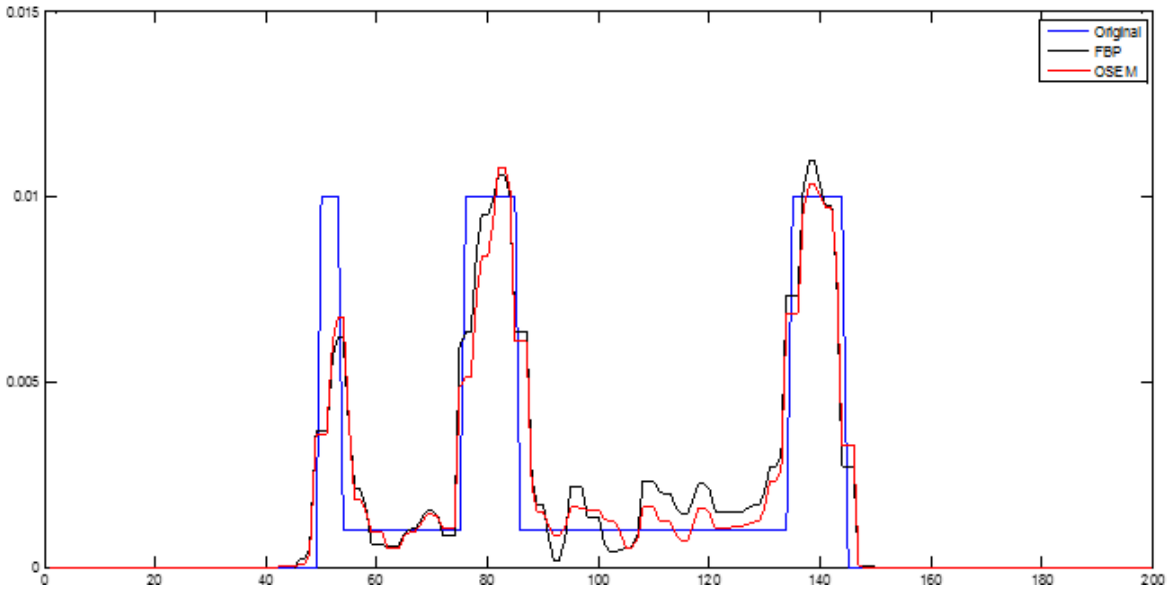


***Figure 5.17*** *- Cardiac model profile averaging. Number of noise realizations = 10*

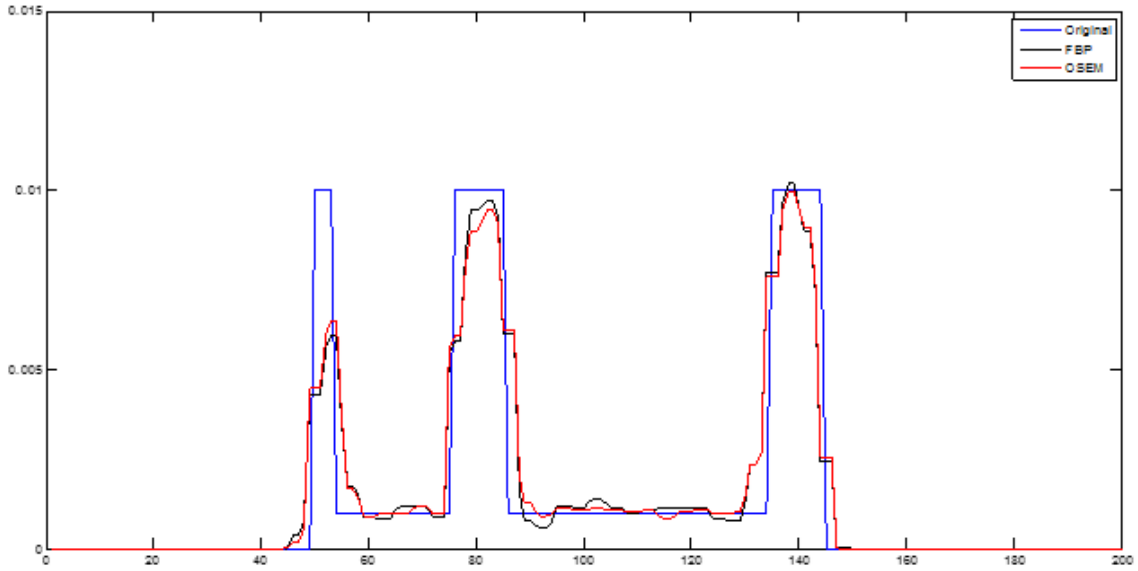


***Figure 5.18*** *- Cardiac model profile averaging. Number of noise realizations = 100*

Given the observed adequacy of the above results, and since a greater number of noise realizations would produce a significant computational load, it was considered that a number of noise realisations of 100 would be adequate and sufficient to obtain a good estimate of the average parameters in later sections.

## 5.4.2. Model Validation and Quantification of Sources of Variability

### 5.4.2.1. FWHM Variation with Count Magnitude

It was observed that there was an inherent degree of variability in the estimation of the FWHM of point sources, due to the image's low count magnitude and the presence of noise in each reconstruction routine output. This would lead to different blurring estimates at each count magnitude. In the previous section it was established that taking 100 image averages from reconstructions with different noise seeds would, in principle, decrease the variability in the model, associated presence of noise. This leaves solely the count magnitude as a source of FWHM variability to measure.

Therefore, the current study was organised towards obtaining a final averaged point source image from reconstructing the same original point source with 100 different noise seeds. However, the standard error would still be calculated from the FWHM of all single reconstructions.

This was performed in terms of FBP reconstructions only, assuming that the FWHM variability for OSEM reconstructions would be of the same order of magnitude.

It is worth noting that the FWHM was estimated using *STIR*'s embedded *find_fwhm* function.

The below Table 5.3 and Fig. 5.19 illustrate the initial results of the mean and standard deviation of FWHM values from 100 reconstructions, for each count magnitude, from *0.01* to *100*.

***Table 5.3*** *- FWHM variation with CM, in the XX and YY directions*

| Count Magnitude | Mean (*XX*) | Std. Dev. (*XX*) | Mean (*YY*) | Std. Dev. (*YY*) |
|---|---|---|---|---|
| **.01** | 10 | 11 | 12 | 17 |
| **.1** | 5.3 | 0,9 | 5.2 | 0,4 |
| **1** | 5.11 | 0,07 | 5.12 | 0,07 |
| **10** | 5.11 | 0,02 | 5.11 | 0,02 |
| **100** | 5.111 | 0,007 | 5.111 | 0,007 |

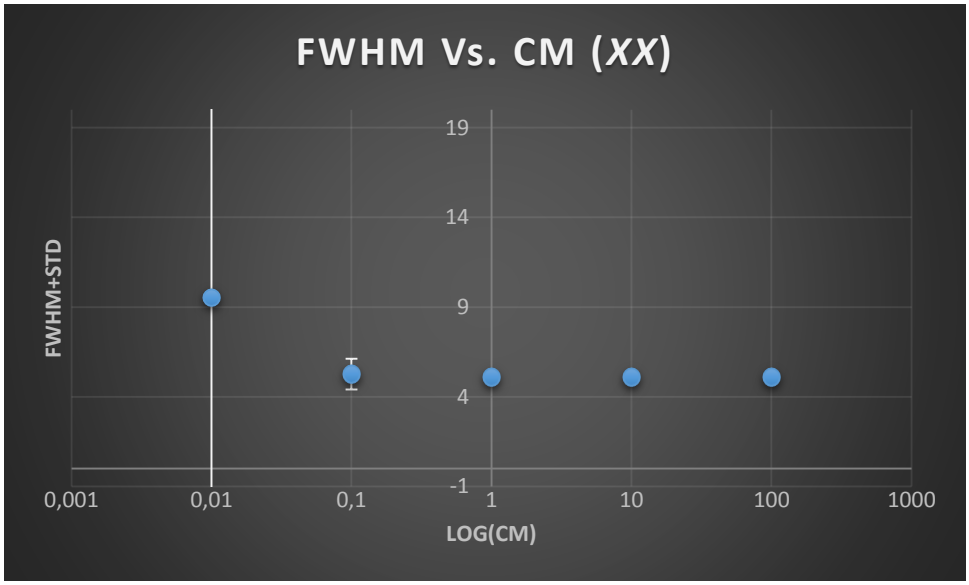


***Figure 5.19*** *- FWHM Variance with CM in the representative XX direction*

Where the most noticeable feature is that the standard deviation of the FWHM values of the 100 reconstructed point sources with a maximum voxel intensity of 0.01 is significantly high, exceeding the mean FWHM value.

This was later assessed as being due to the fact that some of these FWHM values were nonsensical, having very high values, when it is known that the equivalent blurring caused during the reconstruction would amount to the same typical values as in a real scanner environment (i.e. ~5 mm, as confirmed per the above Table 5.3, for voxel count magnitude values from 0.1 onwards). This was appreciated as an effect of noise at lower counts, and it is due to the difficulty of *STIR*'s inherent *find_fwhm* function in detecting the real image peak caused from the point source, possibly due to noise. In practical terms, what occurs is that due to the effect of noise at a low count magnitude, the *STIR*'s function detects apparent signal peaks that do not correspond to the same location as the point source, hence outputting unexpected FWHM values. Fig. 5.20 depicts the obtained values of the FWHM of a point source with an initial voxel count of 0.01, for 100 reconstructions.

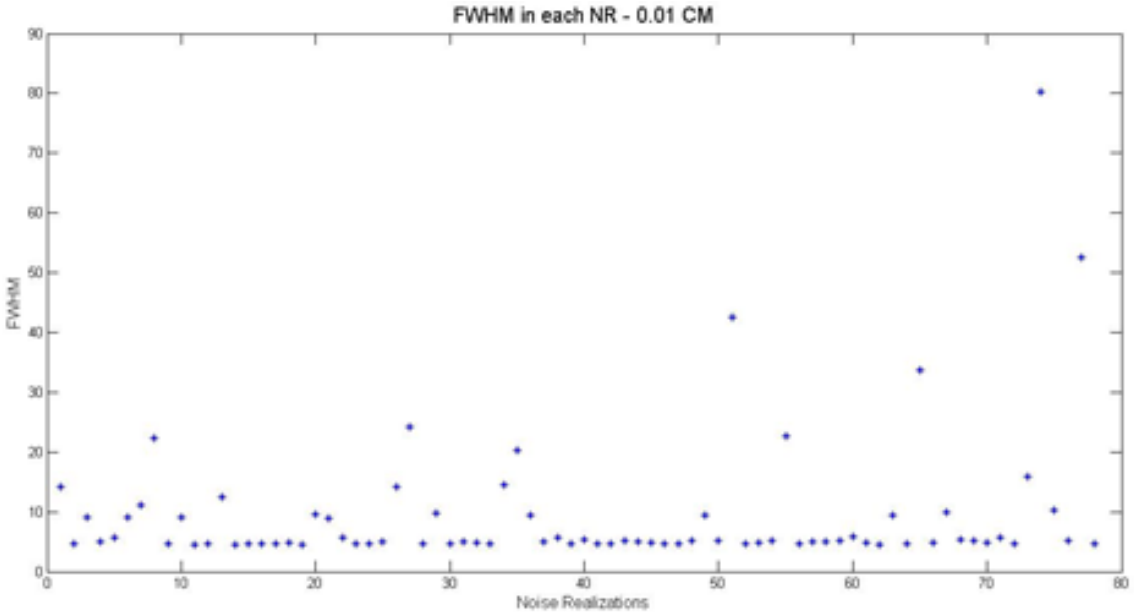


***Figure 5.20*** *- FWHM of PSF of 100 FBP reconstructions of point sources with CM of 0.01*

Given the distribution of values observed in Fig. 5.20, the chosen option was to consider as outliers the percentile correspondent to the highest 15% FWHM values, and exclude them from the mean and variability estimations.

The graphical representation in Fig. 5.21 illustrates this data truncation process.

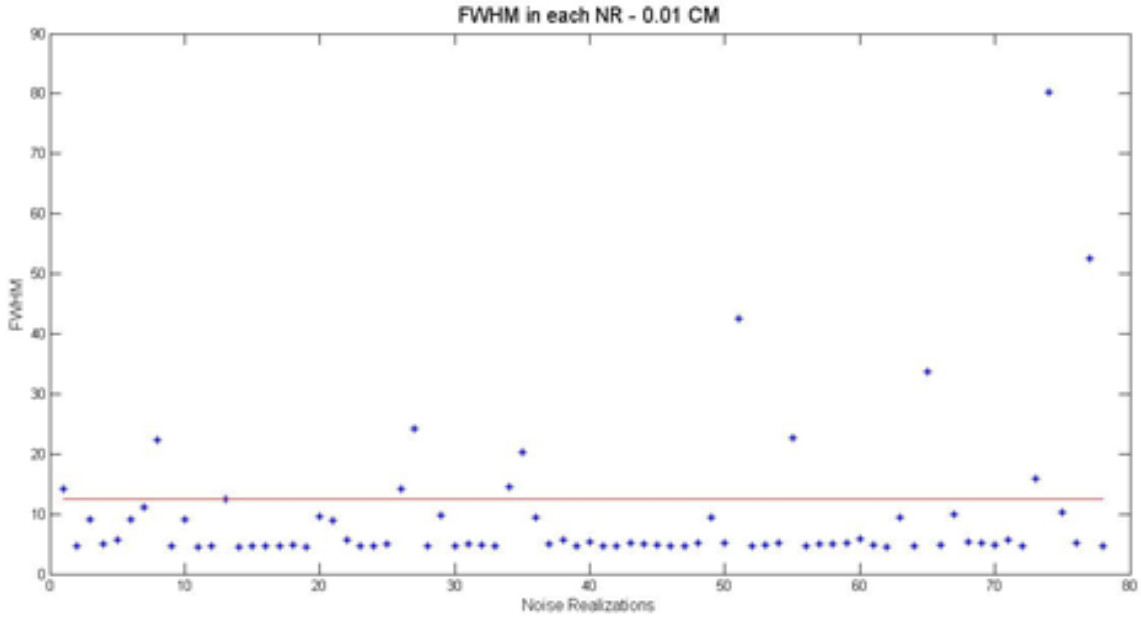


***Figure 5.21*** *- FWHM of PSF of 100 FBP reconstructions of point sources with CM of 0.01 - truncation of outliers*

Following this procedure, the amended Table 5.4 and Fig. 5.22 were constructed as a final output of this FWHM variability study, with the count magnitude of the original image.

*Table 5 4 - Amended FWHM variation with CM, in the XX and YY directions*

| Count Magnitude | Mean (*XX*) | Std Dev (*XX*) | Mean (*YY*) | Std Dev (*YY*) |
|---|---|---|---|---|
| **.01** | 6 | 2 | 7 | 3 |
| **.1** | 5.3 | 0,9 | 5.2 | 0,4 |
| **1** | 5.11 | 0,07 | 5.12 | 0,07 |
| **10** | 5.12 | 0,02 | 5.11 | 0,02 |
| **100** | 5.111 | 0,007 | 5.111 | 0,007 |

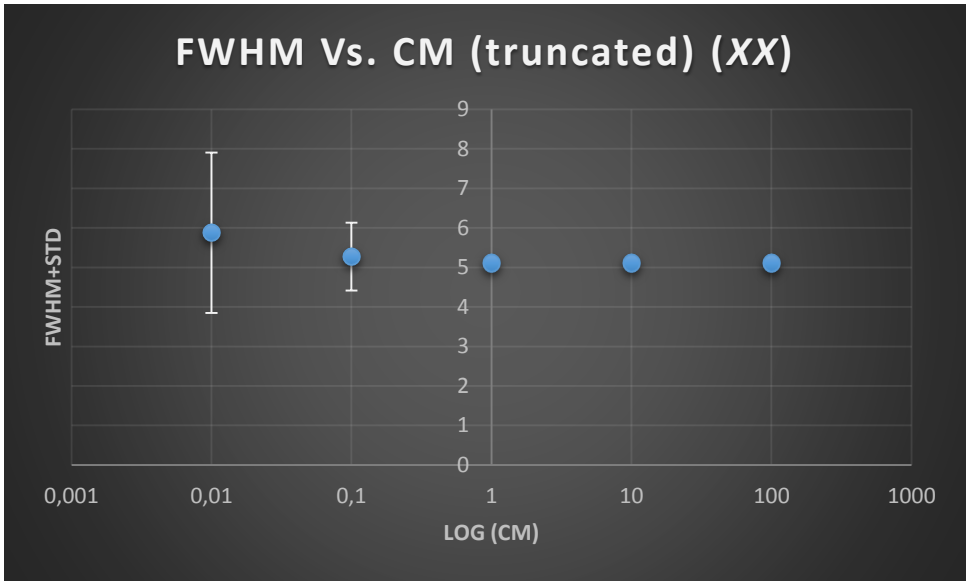


*Figure 5.22 - Amended graphical representation of FWHM Variance with CM in the (representative) XX direction*

Where it can be clearly observed that the variability in this measurement has now a more appropriate and realistic order of magnitude, since the mean FWHM was calculated to be around 6 mm on the *XX* direction, and 7 mm on the YY direction, with standard deviations of 2 mm and 3 mm, respectively.

Therefore, a meaningful estimate of the variance associated with the FWHM of a point source, for each relevant count magnitude, has been successfully determined, along the *XX* and *YY* directions.

### 5.4.2.2. FWHM Variability across the FOV

In the previous section it was observed that there is an inherent degree of variance in the estimation of the FWHM of point sources, according to the original image's count magnitude. On the other hand, in this section the aim was to quantify the variance of the FWHM of point sources located at different regions of the FOV, initially by fixing the count magnitude to 0.01, since this was the most appropriate value selected to be used throughout the study, as per the measurements in section **5.4.1.1**.

However, this showed to be unfeasible. As shown in the previous subsection, the fact that the *find_fwhm* function of STIR often detects an incorrect peak at lower CMs is not compatible with the study of FWHM variability across the FOV. In order to overcome this impracticability, the

choice was to perform the measurements using a higher CM for the point source (i.e. *0.1*), in order to avoid the masking effect caused by noise at lower CMs.

The variability of the FWHM across the longitudinal direction of the simulated scanner was expected to be null, hence the approach was made so that the FWHM variability across the FOV was measured using one single axial plane, with point sources positioned along the *XX* and *YY* directions of that same plane. The FWHM values for each of the point sources would be measured and documented, after the reconstruction routine. The variability would be measured separately for the OSEM and FBP reconstructions.

The number of random and scatter counts was also set to null values, and it is also worth mentioning that this study was performed in terms of OSEM and FBP reconstruction routines.

This study consisted in depicting the locations of the point sources along the *XX* and *YY* directions, at different pre-defined positions, as well as the FWHM estimated along these same points. The (0,0) position corresponds to the origin of the plane.

Fig. 5.23 below illustrates the *XX* and *YY* components of the FWHM of point sources located in different regions along the *YY* axis of the FOV (in the same longitudinal plane).

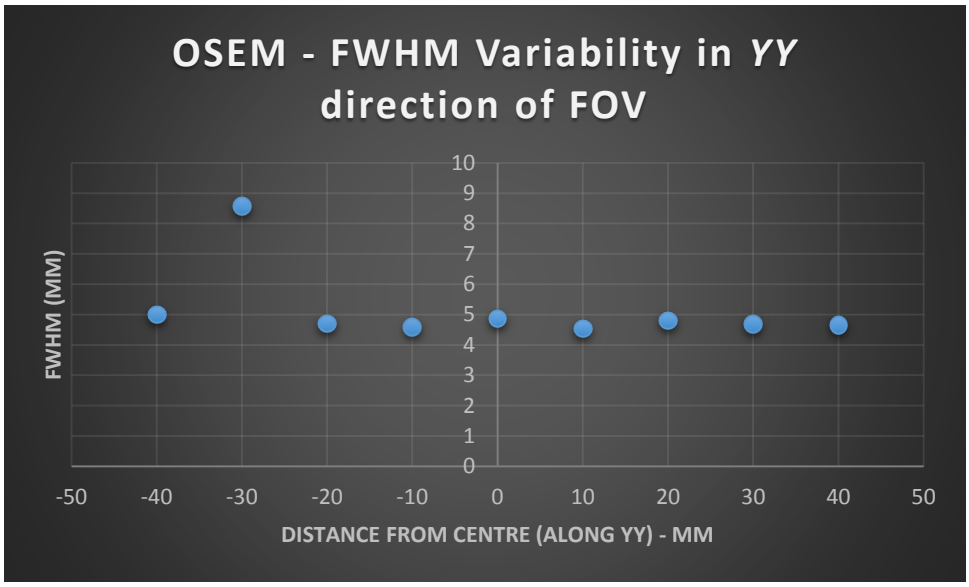


***Figure 5.23*** *- FWHM Variability along the YY direction of the FOV, using an OSEM reconstruction*

In quantitative terms, the information contained in Fig. 5.23 can be summarized in Table 5.5.

***Table 5.5*** *- Mean and standard deviation of FWHM values along YY direction of the FOV, using OSEM reconstruction*

| Rec. Type (Direction) | Mean (*XX*) | Std. Dev. (*XX*) | Mean (*YY*) | Std. Dev. (*YY*) |
|---|---|---|---|---|
| **OSEM (*YY*)** | 4.9 | N/A | 5.2 | 1.3 |

From analysing the previous Fig. 5.23 and Table 5.5, the relatively high variance observed on the FWHM estimation of the point sources in the *YY* direction can be seen as due to the presence of

an outlier on the data, which was generated as a result of noise, potentially due to the determination of an incorrect peak from the *find_fwhm* function. This is an important result, which shows that although a higher CM has been assigned to the point sources in this study, the presence of noise combined with a relatively low aptitude of the *find_fwhm* function still generate inconsistencies in the results, although at a less significant level.

Conversely, measuring the FWHM of averaged point sources at different *XX* locations of the FOV, while keeping the *YY* direction invariant, result in the depictions evidenced in Fig. 5.24.

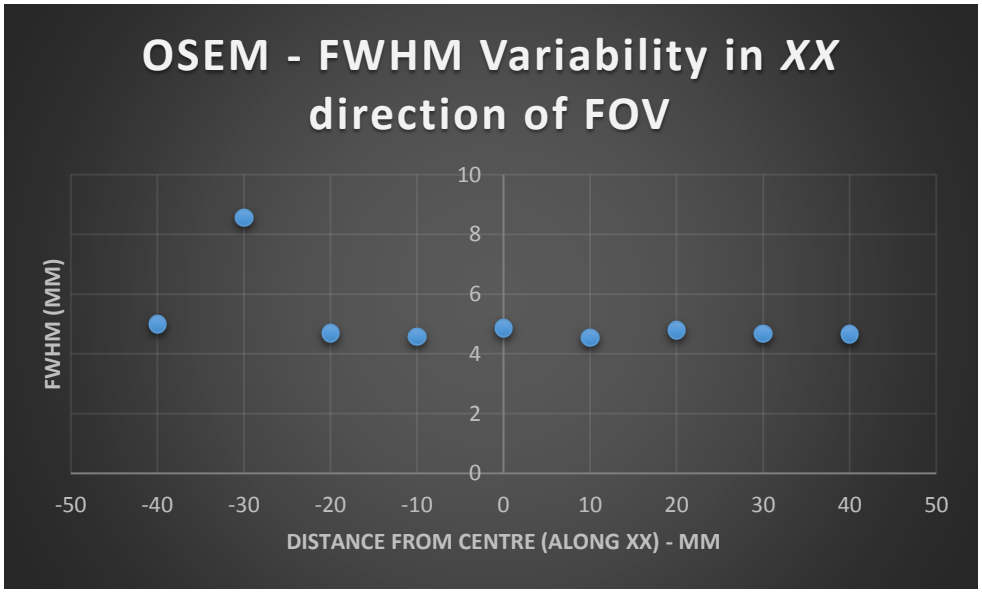


***Figure 5.24*** *- FWHM Variability along the XX direction of the FOV, using an OSEM reconstruction*

Which in turn lead to the obtainment of Table 5.6.

***Table 5.6*** *- Mean and variability of FWHM values along the XX direction of the FOV, using an OSEM reconstruction*

| Rec. Type (Direction) | Mean (*XX*) | Std. Dev. (*XX*) | Mean (*YY*) | Std. Dev. (*YY*) |
|---|---|---|---|---|
| **OSEM (*XX*)** | 5.2 | 1.3 | 4.9 | N/A |

Which leads to the important realization that the amount of blur added to the image, upon an OSEM reconstruction scheme, is symmetrical in the *XX* and *YY* directions of the FOV, since keeping the *YY* point source coordinate invariant, conversely causes the *YY* FWHM estimated value to be invariant as well, and the *XX* component of the FWHM to adopt the same range of values as in the same axial plane, rotated in $90^{\circ}$.

However, this symmetry is a particularity of the OSEM reconstruction routine, since a study performed with FBP reconstructions of point sources, under the same framework of point source positioning, led to the obtainment of slightly different results.

Fig. 5.25 provides with the FWHM *XX* and *YY* components of FBP reconstructed point sources, across different *YY* coordinates of the FOV, whilst the *XX* direction was kept as invariant.

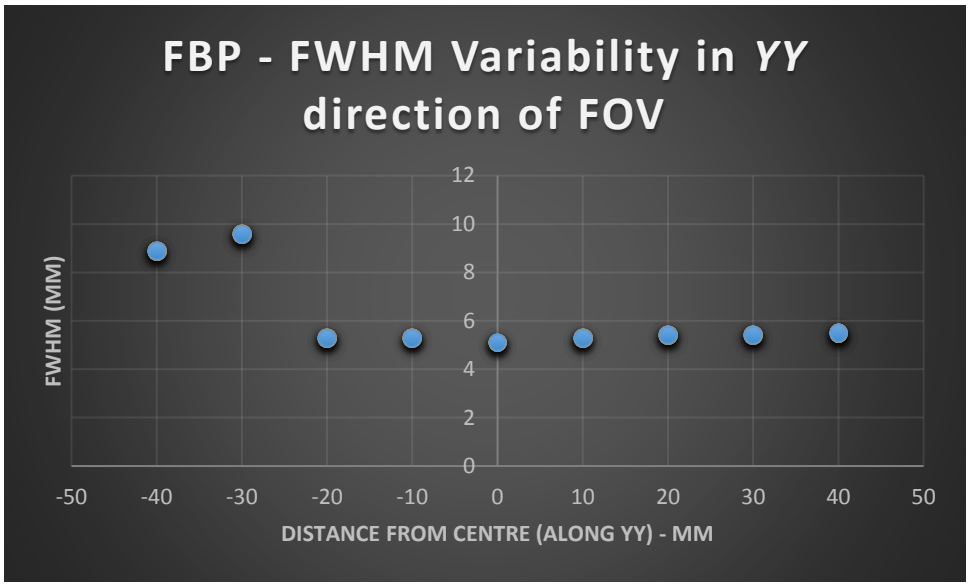


***Figure 5.25*** *- FWHM variability along the YY direction of the FOV, using a FBP reconstruction*

Which allowed for the obtainment of the following values, for the XX component of the FWHM as well.

***Table 5.7*** *- Mean and variability of FWHM values along the YY direction of the FOV, using an FBP reconstruction*

| Rec. Type (Direction) | Mean (*XX*) | Std. Dev. (*XX*) | Mean (*YY*) | Std. Dev. (*YY*) |
|---|---|---|---|---|
| **FBP (*YY*)** | 5.5 | 0.2 | 6.2 | 1.7 |

Where although a similar pattern in terms of *XX* FWHM invariance can be observed following *XX* positioning invariance as well (negligible deviation), similarly to the OSEM case, the *YY* FWHM component's variance of point spread functions along different *YY* coordinates of the FOV is more significant, possibly associated with an increased amount of noise, which is characteristic in FBP reconstructions.

Measuring the *XX* and *YY* components of the FWHM of PSFs across the *XX* direction of the FOV lead to the obtainment of the following values, following a FBP reconstruction routine.

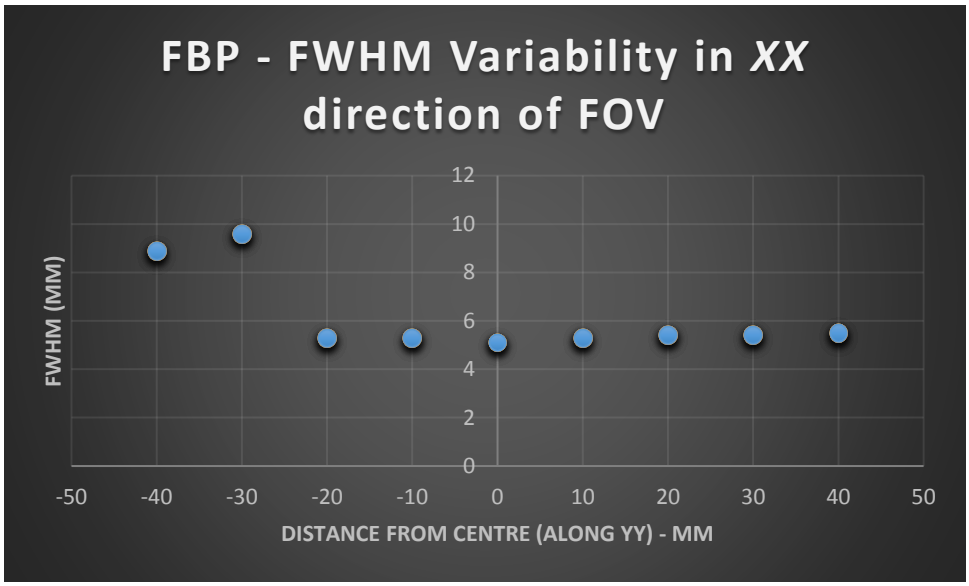


*Figure 5.26 - FWHM variability along the XX direction of the FOV, using a FBP reconstruction*

Where once again a symmetry pattern is observed, as per the results depicted in Table 5.8. This symmetry is present in the *XX* and *YY* directions of the FOV; as well as the *XX* and *YY* components of the FWHM.

***Table 5.8** - Mean and variability of FWHM values along the XX direction of the FOV, using an FBP reconstruction*

| Rec. Type (Direction) | Mean (*XX*) | Std. Dev. (*XX*) | Mean (*YY*) | Std. Dev. (*YY*) |
|---|---|---|---|---|
| **FBP (*YY*)** | 6.2 | 1.7 | 5.5 | 0.2 |

Despite the similarity in the results obtained in this study, for the two different reconstruction approaches utilized, namely the symmetry of the PSF across the *XX* and *YY* directions of the FOV, it is worth noting that this simple study has also allowed to evidence the slightly more significant amount of blur and noise resulting from FBP reconstructions, as compared to data generated following an OSEM reconstruction routine.

However, the main conclusion that can be derived from this exercise is that in the central locations of the FOV - where the ventricle heart model was inserted – there is little variation in the blurring induced by the simulated image acquisition and reconstruction system.

### 5.4.2.3. OSEM Number of Subiterations

A specific trait exclusive to OSEM is the fact that the image updates in the reconstruction process use only a subset of the acquired projections, with each update called a subiteration. An OSEM reconstruction routine can be created with a pre-determined set of subiterations, and the goal of this section was to determine the minimum number of subiterations that are required in order for the reconstruction procedure to present with stable solutions.

In order to accomplish this, reconstructions with different numbers of subiterations were implemented, and the results depicted in Fig. 5.27 were obtained, showing the original pre-blurred image and the reconstructions with different numbers of subiterations.

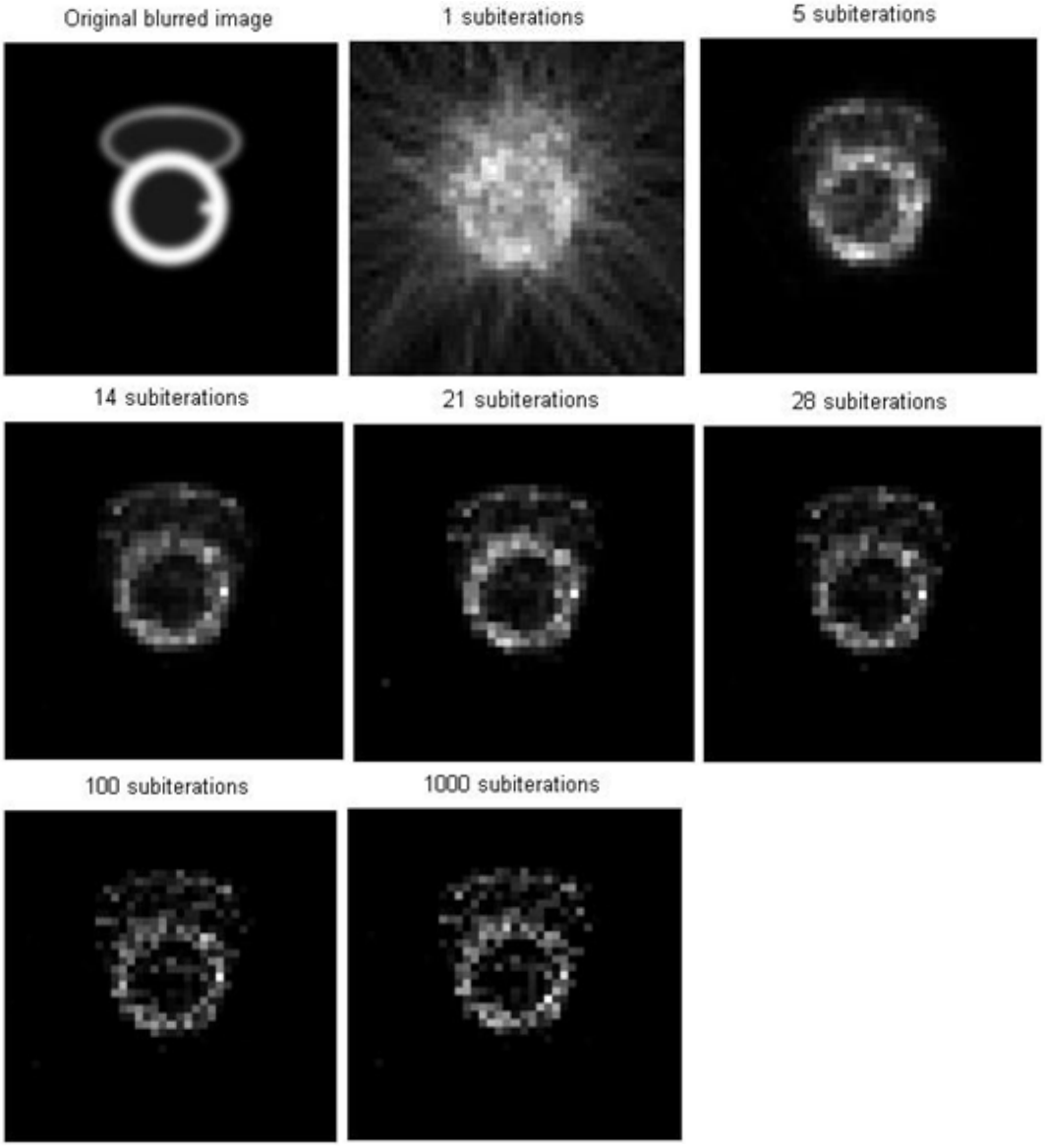


***Figure 5.27** - Depiction of OSEM reconstructed images with different numbers of subiterations*

The visual depiction of subiterations in Fig. 5.27 suggests that starting from the 14$^{th}$ subiteration the image presents with an acceptable level of quality.

However, in quantitative terms the following assessment was performed, resulting in Fig. 5.28, which depicts the evolution of the maximum voxel value in OSEM reconstructed images versus the number of subiterations, in order to obtain a quantitative assessment of the reconstruction routine's stabilisation.

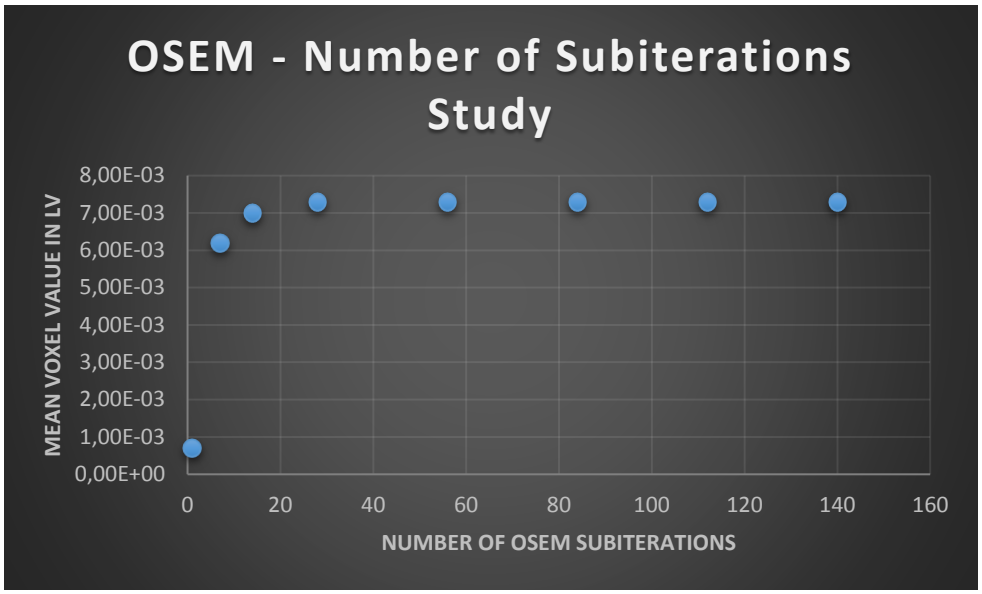


***Figure 5.28*** *- Mean voxel value variation with number of OSEM subiterations - lower scale*

From Fig. 5.28, it can be observed that from subiteration number 28 there is a stabilisation on the LV mean voxel values on the reconstructed image.

Therefore, in order to maximize the accuracy of the future PVE quantification for OSEM reconstructed images, ensuring that the reconstruction time is minimised in parallel, the value of 28 subiterations was chosen to be taken for OSEM reconstructions throughout the study. It is also relevant to note that the higher the number of subiterations, the lower the SNR. Therefore, although a high number of subiterations should ensure a proper convergence of the algorithm, it would also incur in a greater variability of the intensity values within the image due to an increased noise effect in the estimated parameters, as well as an increased the computation time.

## 5.4.3. Implementation of Image Blur

The fact that the projection and reconstruction phases of the FBP and OSEM routines apply an inherent blurring to the image – which does not equal the 10 mm FWHM blur applied during the simple convolution execution part – leaves an issue that consists in the fact that the equivalent blur and hence the PVE quantification would be done under a different basis in case this difference in blur would not be amended.

In order to solve this issue, a set of steps were taken in order to ensure that the overall blurring in this execution part would equal the amount of 10 mm FWHM as well.

The process consisted in separating the blurring procedure into 3 different parts, which improved the realistic nature of the study by mimicking the amalgamated blurring process that takes place in a clinical environment. Since the *STIR*'s simulation routines implemented could not apply the system's PSF blurring effect, a first stage of blurring was implemented in order to simulate this result, as well as the blurring due to the positron range of the radionuclide ($^{82}$Rb in this case), and due to the effects of motion, which are often still latent even following gated and/or motion corrected image acquisitions. This first stage of blurring was determined to be the major source of PVE degradation in the image formation process, and was hence applied by convolving a 4

mm FWHM, symmetric PSF to the image with the original activity distribution. This step was labelled as the *Pre-Blurring* step. Following this, the second blurring stage was simply characterized by the reconstruction procedure, which introduced an additional amount of blur that could not be completely quantified due to its complex dependencies, such as the reconstruction type, the geometry of the original object, the activity distribution, the count magnitude, the FOV location and the effect of noise. Therefore, this *Reconstruction Blurring* step incurred in the production of an asymmetric blur (as shown in the previous section). The final stage of this process consisted in the application of a convolution operation on the resulting image with a customized asymmetric PSF, specific to the FBP and OSEM routines, and determined upon a trial and error method, by matching the current image resulted from the *Reconstruction Blurring* step, against an already blurred high count magnitude image with a 10 mm FWHM PSF blur. This step aimed to simulate the post filtering procedure that takes place in conventional emission tomography images, following the acquisition of the raw data, and was named as *Post Smoothing* blurring phase.

Fig. 5.29 presents a diagram that illustrates the aforementioned process.

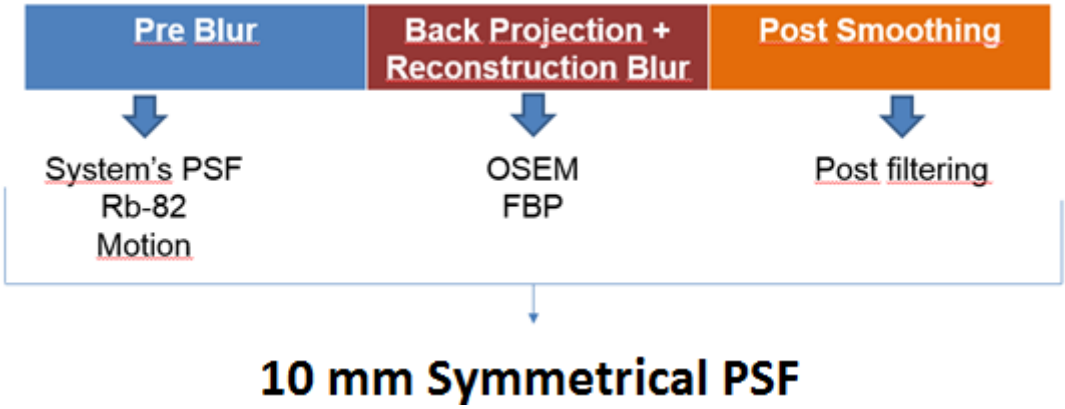


***Figure 5.29** - Blur matching process for STIR reconstructed images*

Due to the inherent difference in the blurring introduced by the FBP and OSEM reconstructions, the FWHM of the post smoothing filter – which was calculated using a trial-and-error fashion – had to be different as well, in order to produce a final equivalent blurring which was as close as possible to 10 mm FWHM, in both reconstruction methodologies.

As mentioned previously, following the reconstruction routine the post-blurring needed to be asymmetrical and their *XX*, *YY* and *ZZ* components, for OSEM and FBP. It is worth noting that the same post blurring was applied to all images that followed the same reconstruction routine in this study, including images with and without BP/IVS. This was performed in order to ensure consistency when comparing correspondent images with and without a certain region. Table 5.9 below clarifies on the FWHM component values of the post smoothing process carried out for OSEM and FBP resulting images.

***Table 5.9** - Post smoothing filter's XX, YY and ZZ FWHM components for FBP and OSEM*

| Reconstruction Type | FWHM - *XX* | FWHM - *YY* | FWHM - *ZZ* |
|---|---|---|---|
| **FBP** | 3 | 3 | 8 |
| **OSEM** | 6.5 | 6.5 | 9 |

From Table 5.9 it can be observed that the post-blurring is significantly more intense in the case of OSEM, since it appears that during the actual reconstruction step the image suffers a less significant blurring effect, in comparison to the FBP reconstruction.

Figs. 5.31 and 5.32 depict a blur matching exercise on the created ventricular heart model, following FBP and OSEM reconstructions, in a 1D perspective. The profiles were taken as shown in Fig. 5.30, in an averaged image resulting from 100 reconstructions with different noise realisations. The maximum voxel value of the original image was of *0.01*, as determined from section 5.4.1.1. The same count magnitude would be used in the next sections of the study, and no observable change in the profiles was observed from post smoothed images with different IVS/BP configurations, which validates the usage of the same post-blurring for images which resulted from the same reconstruction type.

***Figure 5.30*** *- Axial 1D profile location illustration*

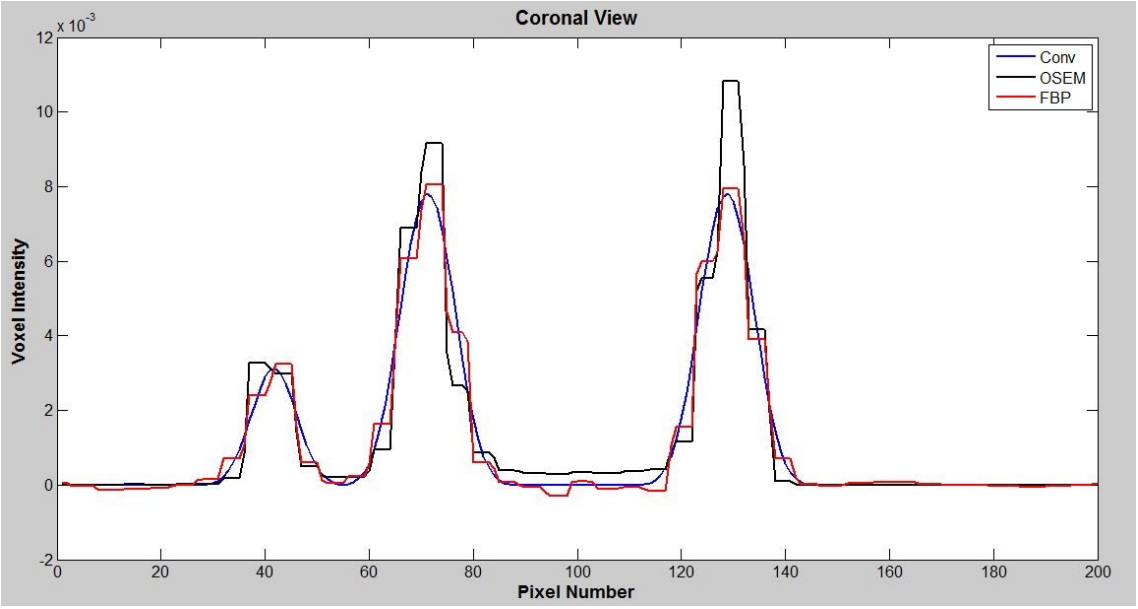


***Figure 5.31*** *- Blur match study of FBP and OSEM reconstructions against 10 mm blurred model image – before matching*

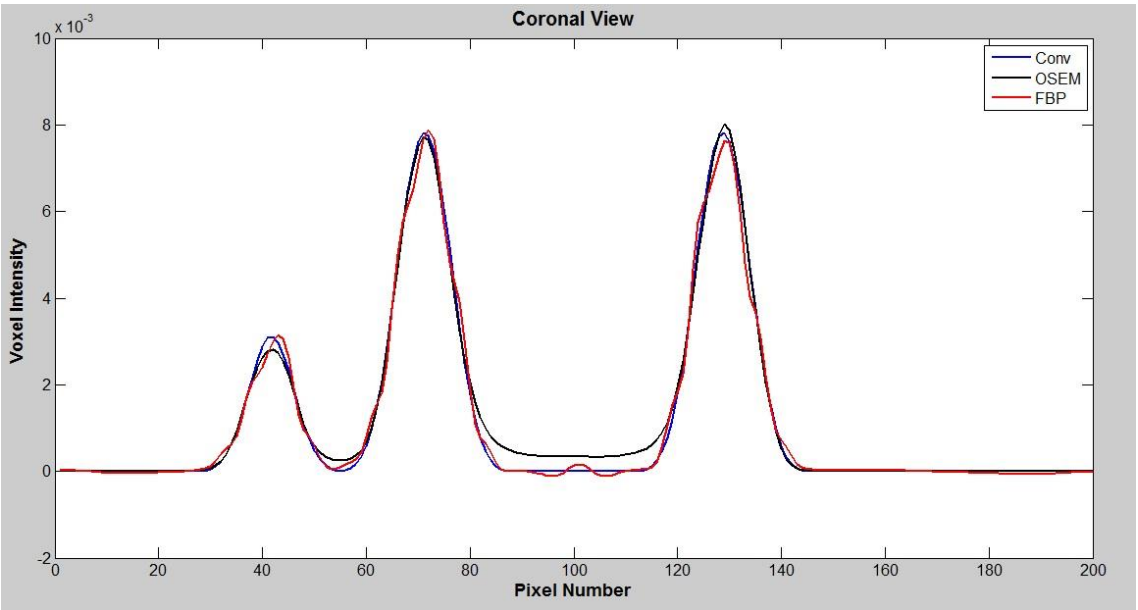


***Figure 5.32*** *- Blur match study of FBP and OSEM reconstructions against 10 mm blurred model image – after matching*

By matching the reconstructed images against a purposely 10 mm FWHM blurred reference image, the overall equivalent blurring process allowed for the data originating from the *STIR* reconstruction routines to be quantified against the results of the simple convolution process, from section **5.2**.

In any case, discrepancies were still expected to occur between the activity distributions from the simple convolution blurring approach and the realistic 3-step blurred images, which are due to the noise effect, inherent to the latter. Therefore, any PVE estimation discrepancies would be related to this unavoidable difference between the two approaches.

## 5.4.4. Main Quantification Results

Following the validation and improvement of the realistic nature of the model created in the previous sections, it became possible to proceed with the quantification of the PVE produced by each of the relevant cardiac ROIs, from *STIR*'s realistic-enhanced approach.

The same study as the one performed in section **5.2** was carried out, now for each of the FBP and OSEM reconstructions, while establishing a comparison with the correspondent convolution-based results and incorporating the standard deviation associated with the plurality of noise realisations averaged in order to generate each final FBP or OSEM image.

The actual PVE values were calculated from averaged images over 100 reconstruction pairs (one with relevant structure and another without), whilst the standard deviation of these PVE values was computed based on the PVE of each individual pair of 100 reconstructed images with different noise realisations (again, each pair consisting in one image with relevant structure and another without). This same approach was utilised throughout this section, and was motivated following the realisation that the PVC metrics in the final averaged images had essentially the

same values as the same metric calculated individually for each noise realisation, and then averaged afterwards (difference < *0.1%*).

Following the same order and set-up as in section **5.2**, the IVS' PVE was plotted against their geometry (diameter), which is illustrated in Fig. 5.33.

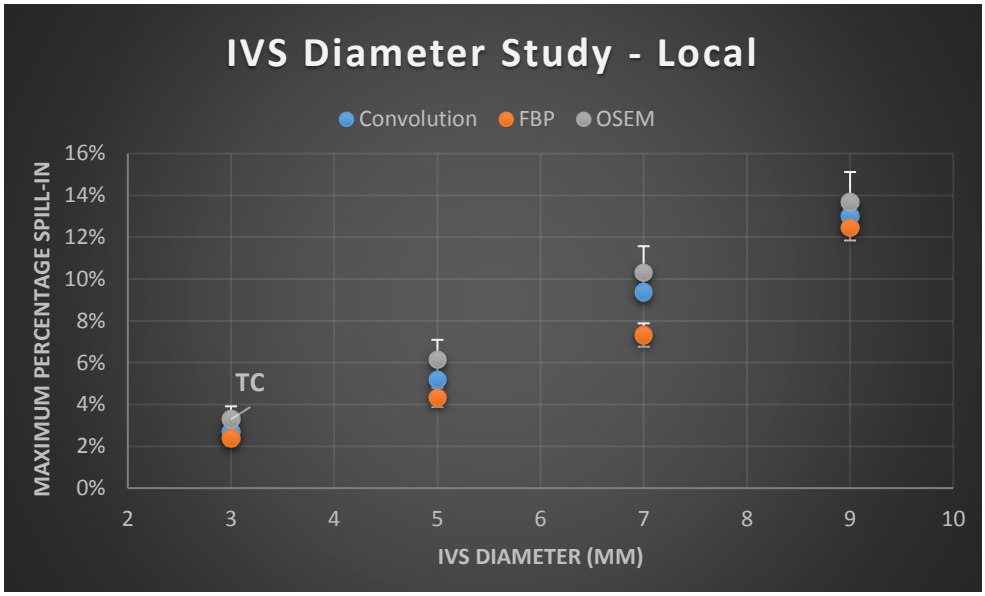


***Figure 5.33*** *- STIR's IVS Diameter Local PVE Study*

Where it is observed that although the PVE measured from the simple convolution method is essentially the same as in OSEM, within the standard deviation of the latter. On the other hand, the FBP's PVE appears to deviate from that of the remaining two methods, with the exception of the TC, in which all the blurring methodologies appear to present the same PVE value. At this point it is worth noting that the standard deviation was calculated based on the PVE calculated for each individual reconstruction with different noise realisations, at each OSEM and FBP. It is also worth noting that the FBP reconstruction had an associated amount of blur which was higher than in the case of OSEM, which causes the need for a more significant filtering in the case of OSEM, in order for both methodologies to allow for the obtainment of an equivalent 10 mm blur. This, associated with the fact that OSEM images at 28 subiterations may be slightly under converged, lead to smoother OSEM images, and hence with a higher PVE, whilst the FBP ones would be slightly noisier, as evidenced in Fig. 5.32. As a result, the OSEM image will be more similar to the simply convolved one, both in qualitative and quantitative terms, as per Fig. 5.33. The reason why the FBP-resulting image has a lower PVE, is directly correlated with the fact that the image is noisier, rather than necessarily more blurred. In any case, smaller structures (i.e. TC) appear to have a more similar PVE, which is expected since the PVE is more significant in objects will small dimensions, hence increasing the amount of blurring, which leads towards more homogeneous PVE values across different reconstruction routines (e.g. OSEM, FBP and simple convolution).

Similarly, the impact of the distance between the IVS and the LV wall was also assessed, in terms of a TC and a PM. In Fig. 5.34 this study is depicted, comparing the results from the convolution and proper reconstructions approaches.

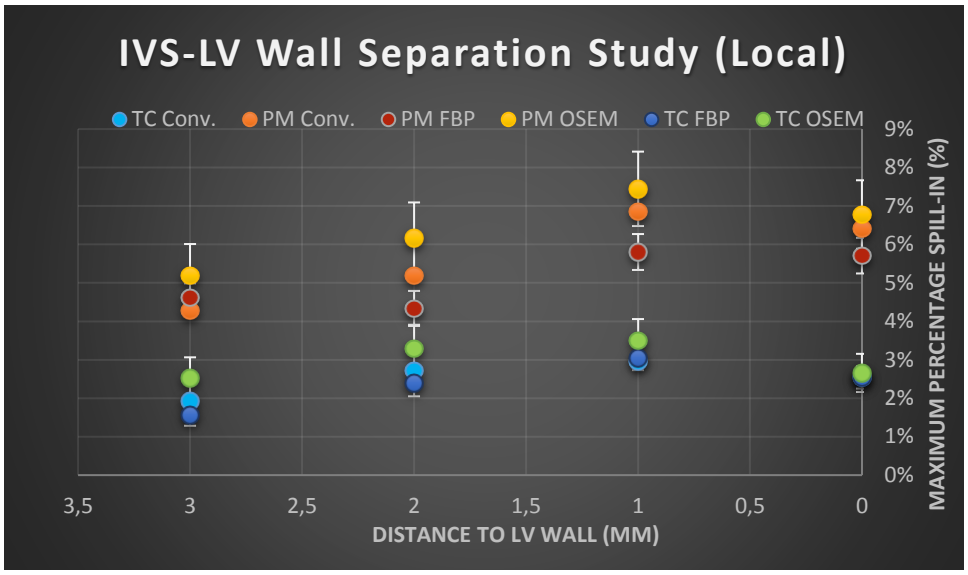


***Figure 5.34*** *- STIR's IVS-LV Wall Separation Local PVE Study*

Where a quite similar pattern as observed in Fig. 5.33 has been obtained. Once again, the OSEM and simple convolution resulting images have an essentially identical PVE, and the FBP resulting data depicts a PVE which only equals the one produced by OSEM and simple convolution in objects with small structures (e.g. TC, in this case).

Following the completion of the LV wall thickness variation study, one was able to gather the data observed in Figs. 5.35 and 5.36, depicting the variation of the PVE produced by IVS and BP, separately.

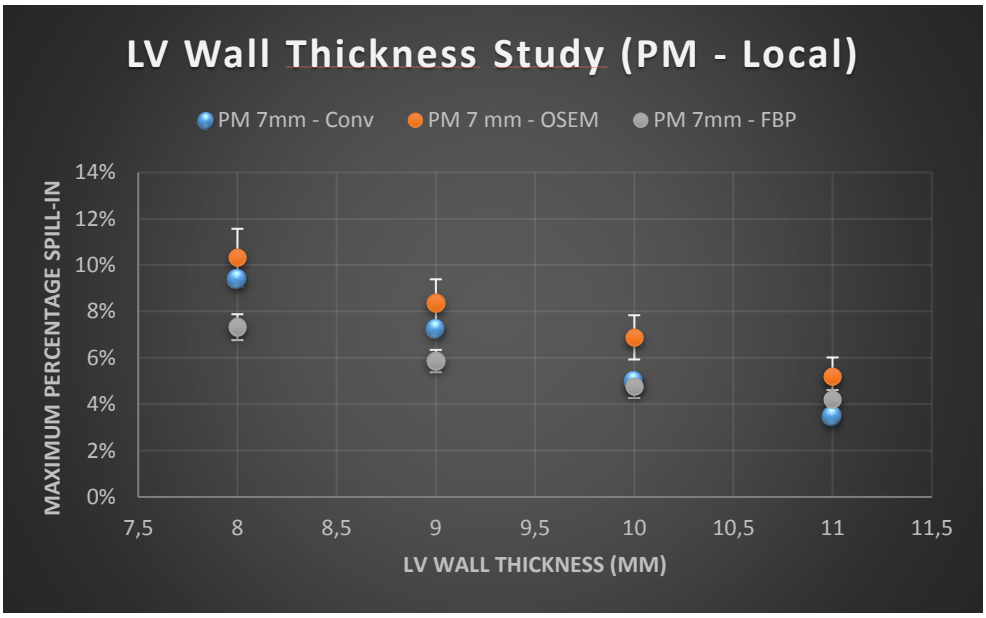


***Figure 5.35*** *- STIR's LV Wall Thickness Local PVE Study*

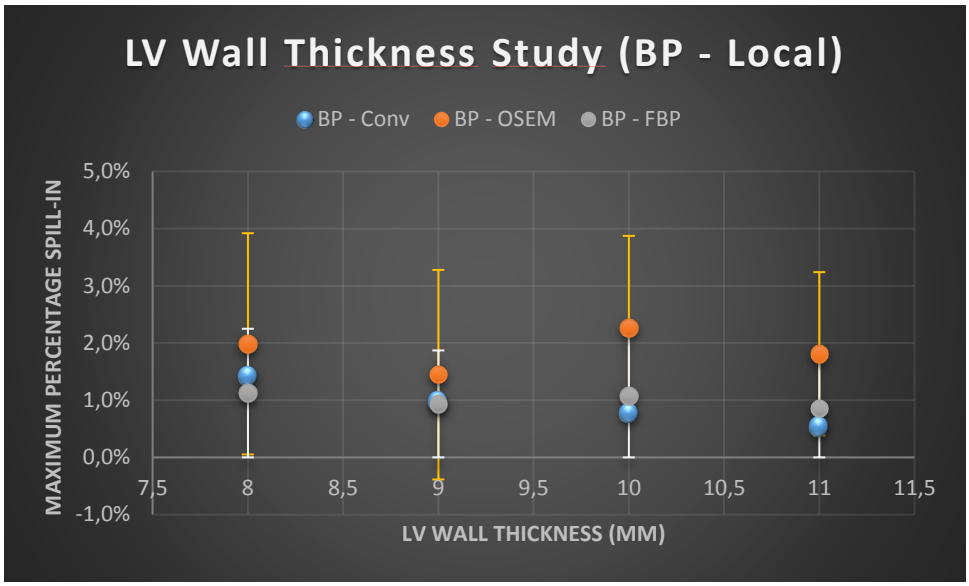


***Figure 5.36*** *- STIR's LV Wall Thickness Total PVE Study. Standard error bar for BP-OSEM in orange and for BP-FBP in white*

Where it can be seen once again that in Fig. 5.35 the images obtained through simple convolution and OSEM reconstruction produce essentially the same maximum local PVE, whilst the FBP falls outside of range. In the case of Fig. 5.36, the PVE produced by each of the simulated reconstruction methods is essentially the same, within the standard error. However, it is worth noting that in the case of the BP's local PVE assessment, a significantly higher standard deviation was recorded in both FBP and OSEM reconstructions.

All the results obtained from the current section, as well as the ones from the first level execution approach (section **5.2**) have culminated in the possibility of computing a realistic estimation of the total and local PVE produced by the BP and different IVS, taking the PVE results from the simple convolution process as the gold standard, and assuming the results from STIR's methodology as actual measures, with an associated standard error.

Fig. 5.37 starts to accomplish precisely that, showing a comparison of the total PVE produced by the BP and the correspondent overall effect from all IVS expected to be encountered within the LV's cavity, namely two PM and a general number of ten TC. The contribution of these individual IVS is assumed to be amounted to a simple sum, given their reasonable spatial distribution within the LV's endocardium, in a real anatomic scenario. One should recall that the current section allowed for the very important realisation that the blurring from the reconstructions is not uniform across the FOV. These measurable discrepancies are assumed to be incorporated in the measure of the PVE associated with the current model, and the standard deviation of the PVE values produced at each noise realisation reconstruction, both for FBP and OSEM, was taken as a measure of the uncertainty associated with the determination of the PVE. It is worth noting that for the IVS PVE assessment, the maximum possible IVS contribution, as per the geometrical limits imposed to the ventricular heart model, has been represented in the following results. This translated into depicting the PVE results of a 9 mm PM located at 0 mm from the LV wall, whilst the latter is at its lower thickness (8 mm). The BP's PVE was also computed at its maximum (for a 8 mm LV wall thickness).

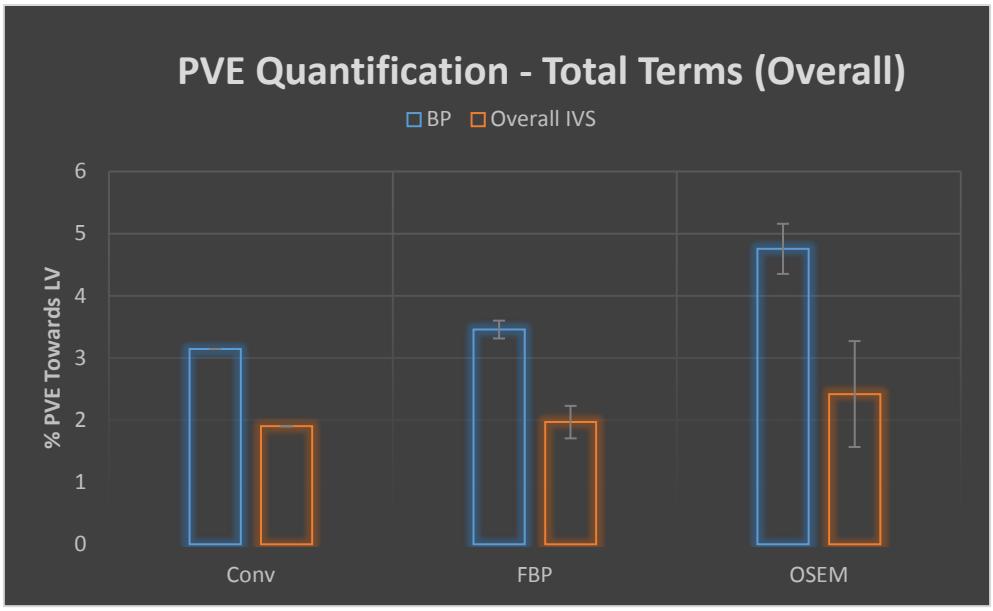


***Figure 5.37*** *- Total PVE Quantification of BP and IVS, under a simple convolution, FBP and OSEM approaches*

Fig. 5.37 shows a consistent pattern in terms of PVE proportions between the BP and IVS, across all blurring approaches, with the overall IVS PVE having approximately 50% of the correspondent effect produced by the BP, which can be seen as an intuitive result, given the fact that the BP was modelled as filling all the available space within the ventricular cavity, hence producing its blurring effect in all of the LV's endocardium. The IVS were reported to have essentially the same overall PVE in the FBP and OSEM approaches. Moreover, these are also virtually the same as the gold standard PVE determined using the simple convolution process. However, it can be observed from Fig. 5.37 that this is not the case with the PVE produced by the BP. One explanation for this would be the same as for Fig. 5.33, as the under convergence of the OSEM with 28 subiterations is known to be associated with a higher PVE. It is also worth reiterating that one single post-filter was used for images with and without a BP, in order to allow for a consistent calculation of the PVE (which is determined as the percentage difference in activity in certain relevant ROIs from each image, with and without the structure of interest). This single post-filter is therefore not fully optimised to bring the images with BP to an equivalent blur of 10 mm FWHM, which causes the final reconstructed blur to be slightly different than the one produced by a simple convolution operation.

Similarly to what was accomplished in the previous approach (section **5.2**), the local PVE produced by IVS was assessed as well. Following the determination of the LV's segment that contained the most amount of activity spillover (zone 10, once again), the PVE in that region was compared to the one produced by the BP. This local effect is illustrated in Fig. 5.38, as well as the region adjacent to the IVS where the maximum spillover occurred, for reference purposes. The error associated the PVE was also computed and illustrated.

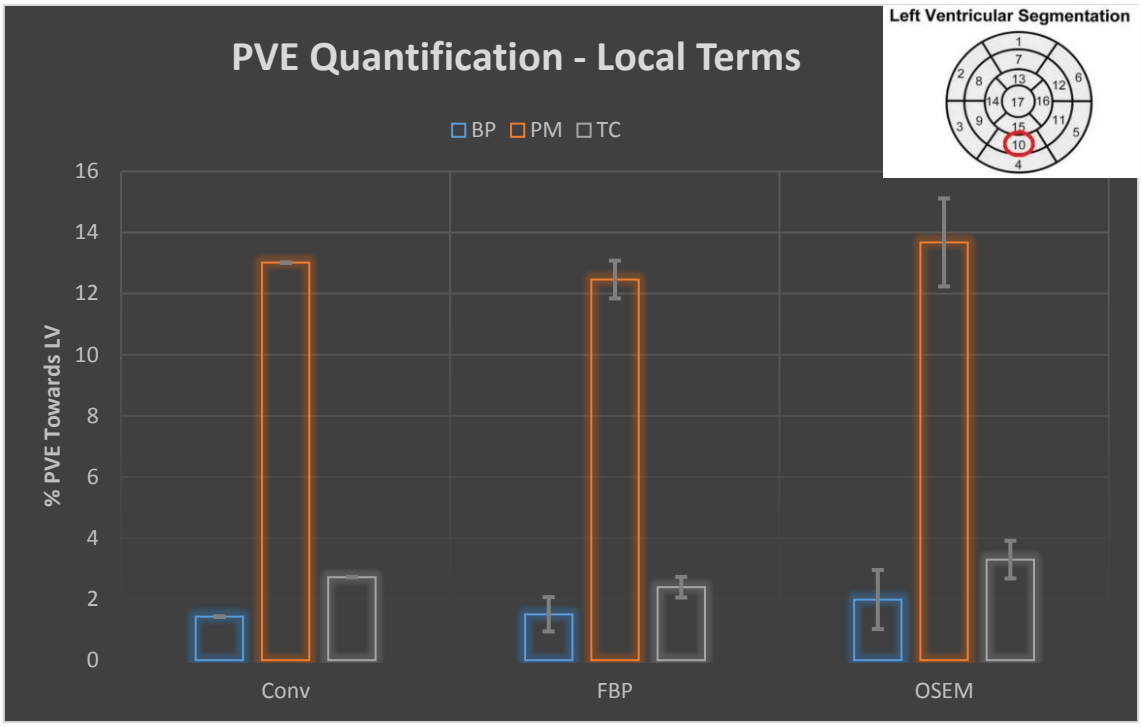


***Figure 5.38*** *- Local PVE Quantification of BP, PM and TC, under a simple convolution, FBP and OSEM approaches*

Which leads to the important realisations that the local PVEs produced by the BP and the TC are equivalent, but most importantly, the local IVS PVE is approximately one order of magnitude higher than the one produced by the other two ROIs.

## 5.5. PVC Study

Following the evaluation of the PVE produced by internal ventricular structures, explored in sections **5.2** and **5.4** of the ***Results and Discussion*** chapter, the next step involved applying actual correction algorithms to the blur produced by the IVS and BP structures, in order to ultimately ascertain whether a PVC routine would be significantly affected by the inclusion of these structures in the correction algorithms or not.

This part was designed in two sections, in which the first contained two stages. The first stage of the first section corresponded to the validation of the selected PVC methodologies, by simply performing a correction routine on an object which had been previously blurred with a known PSF. The second stage of the first section consisted in assessing the error produced by not taking the IVS into account when applying PVC routines, on the ventricular heart model. The second section involved the attempt of implementing the same PVC methodology on real anatomical data. This involved the efforts of selecting an appropriate segmentation methodology, from two available approaches, also involving the choice of adequate real cardiac clinical data to be used for these studies.

The next sub-sections shall enlighten on the successive efforts towards the implementation of the aforementioned process.

## 5.5.1. PVC Method selection and validation

Using the algorithm introduced in section **4.5**, the GTM and iY PVC methodologies were used in the ventricle heart model, following a convolution of the image with a known 10 mm FWHM PSF.

The ability of each one of the two correction routines to recover the original activity distribution in the image was subsequently assessed.

### 5.5.1.1. GTM PVC Validation and IVS PVC Quantification

Table 5.10 provides the normalised GTM results of recovering a model of the ventricle heart containing a LV, a BP and an 9 mm diameter IVS, which was previously convolved with a 10 mm FWHM symmetrical PSF. The PVC was evaluated in total and local terms, seeing that the total assessment was performed in terms of the final mean recovered activity in the LV, and the local corresponded to the same assessment in zone 10, which was once again proved as the region with most variability due to activity spillover from the IVS.

***Table 5.10*** *- GTM PVC results on an image with a known blur of 10 mm FWHM symmetrical PSF*

| ROI | Original activity | Mean Activity After Blur | Mean Activity After Correction | PVC Error (%) |
|---|---|---|---|---|
| **LV (total)** | 1 | 0.6 | 1.0 | 0.03 |
| **Zone 10 (local)** | 1 | 0.7 | 1.0 | 0.07 |
| **BP** | 0.1 | 0.2 | 0.1 | 0.02 |

Where PVC Error is simply respective to the percentage deviation of the recovered mean activity at each ROI, with the original activity values. It can be noted from Table 5.10 that the current GTM correction algorithm provides a very good recovery of the mean voxel value at each ROI, given the negligible PVC Error observed, as expected.

Having validated the GTM correction routine, it became possible to perform a confident quantification of the IVS influence in this PVC scheme. In order to depict this effect, the error resulting from not taking the IVS into account, as an independent structure in the PVC routine, was taken as final output. The total and local PVC errors were assessed from recovering an image containing a 9 mm PM and another containing a TC, in order to obtain an insight on how the PVC process varies at these two extreme IVS scales, similarly to the previous sections.

Table 5.11 shows the original, after blur and corrected normalised mean activity values in the LV, BP and zone 10 ROIs, for both images, one containing a PM and the other a TC.

*Table 5.11 - GTM PVC Error Assessment, upon not including IVS in the correction*

| ROI | Original activity | Mean Activity After Blur | Mean Activity After Correction | Error (%) |
|---|---|---|---|---|
| **LV (total - PM)** | 1 | 0.6 | 1.00 | 0.2 |
| **Zone 10 (Local - PM)** | 1 | 0.7 | 1.06 | 6 |
| **BP - PM** | 0.1 | 0.2 | 0.11 | 8 |
| **LV (total - TC)** | 1 | 0.6 | 1.00 | 0.02 |
| **Zone 10 (Local - TC)** | 1 | 0.7 | 1.01 | 1 |
| **BP - PM** | 0.1 | 0.2 | 0.10 | 1 |

Where it can be seen that the error produced by a single IVS is almost negligible in terms of the activity in the whole LV, although this is one order of magnitude higher than the error observed when the correct PVC mask was used. Moreover, the majority of the error produced in total terms is observed in the BP's calculated mean activity after recovery, which is expected since the incorrect mask used assigns the IVS' activity to a location in the BP. In local terms, the effect of not using a correct mask for the PVC routine was observed to cause a maximum error of 6% in LV's zone 10.

In a similar way as depicted in the previous execution levels (section **5.2** and **5.4**), the amount of error can be summed for each individual IVS that comprises the LV cavity. Analysing Table 5.11, this results in an overall PVC error of ~0.6%, comprising the effects of 2 PMs and a plurality of 10 TCs.

The current PVC methodology was taken a step further, which consisted in it being tested against the OSEM and FBP reconstructed images. The main objective was to evaluate the importance of noise in the PVC routine, and the study was organised in order to illustrate the total and local PVC errors from using an incorrect ROI mask, on an image containing an IVS with 9 mm. The study was categorised in terms of simple convolution, OSEM and FBP related PVC errors and the associated standard deviation for OSEM and FBP. It is worth noting that this standard error was calculated from performing PV corrections on each one of the 100 reconstructed images with different noise seeds, both for OSEM and FBP. The standard deviation of the mean values at each ROI was calculated and then propagated. Fig. 5.39 depicts the respective results.

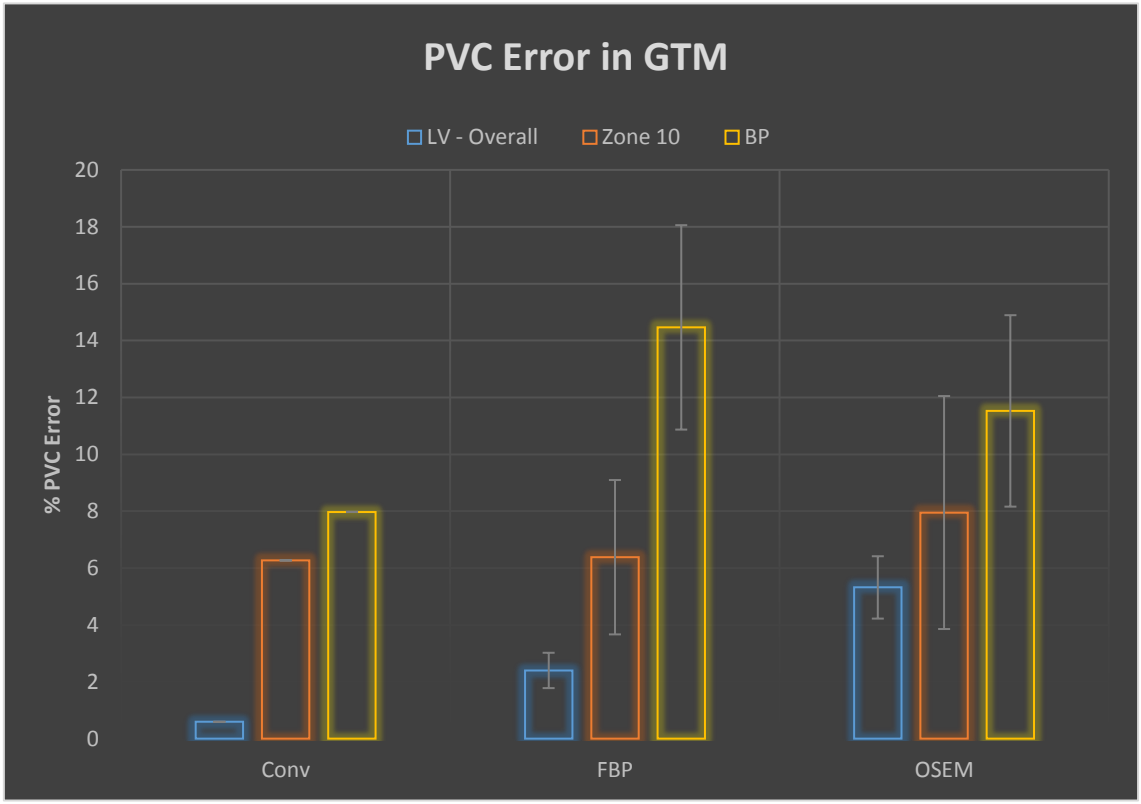


*Figure 5.39 - PVC Error following a GTM activity recovery routine*

These results differ from the ones produced in Figs. 5.37 and 5.38, which is clearly expected, since what is being measured in this instance is no longer the amount of blur contribution from an IVS at each ROI, but the degree to which the activity in a certain ROI can be restored to their original values, using a PVC that does not take the IVS in question into account.

One way to interpret the results from Fig. 5.39 is to ascertain that given the fact that, for example, a ventricle heart model with a 9 mm IVS reconstructed by OSEM was measured to produce a PVE of approximately 14% in local terms (as per Fig. 5.38), the best possible recovery of the activity in the same region would lead to a result with 8% error.

Therefore, from Fig. 5.39 it can be observed that the BP suffered the most significant bias from the attempt to recover its activity using the GTM method. This could potential lead to a miscalculation in the tracer's activity in the blood, in FDG viability protocols, causing the BP not to be considered as a viable option when performing SUV calculations that rely on reference tissues (Perry et al. 2008; Kinahan & Fletcher, 2010). On the other hand, the PVC error associated with Zone 10 has already been reported to manifest in the form of local hyper-intensities on the LV wall, which could potentially mask ischemic regions of the myocardium. With regards to the overall PVC error on the LV wall as a whole, although the error produced is lower, an interesting result is that, essentially for OSEM, the value is more significant, which could mean that the current PVC method is somewhat sensitive to more significant blurring and noise.

Another important observation is that the FBP and OSEM errors are consistently higher than the ones produced from recovering simply convolved images. This can be assigned to the fact that the reconstructed images do not have a blur that amounts exactly to from a 10 mm FWHM PSF, which makes the recovery process less accurate as well. This is an expected result, and should

also be applicable in a clinical setup, as the system's PSF would not be fully homogeneous as well.

In any case, it is worth recalling that the GTM method does not return an actually corrected image, but instead a mean recovered value for each ROI. That is why this method is used more like a precursor of other methods, than actually a correction routine on its own, although it can provide with good results on the activity recovered at each ROI.

In light of the aforementioned, the next sub-section is dedicated to the validation of a full PVC methodology.

#### 5.5.1.2. Iterative Yang PVC Validation

The essential aspect of the implementation of the iY routine using the algorithm referred in section **4.5** is that besides the input blurred image and the FWHM of the deconvolution kernel, the number of iterations also needs to be fed onto the algorithm in order for it to implement the correction routine.

Figs. 5.40-A, 5.40-B and 5.40-C depict the original, blurred and corrected images, when an appropriate anatomical mask is being used.

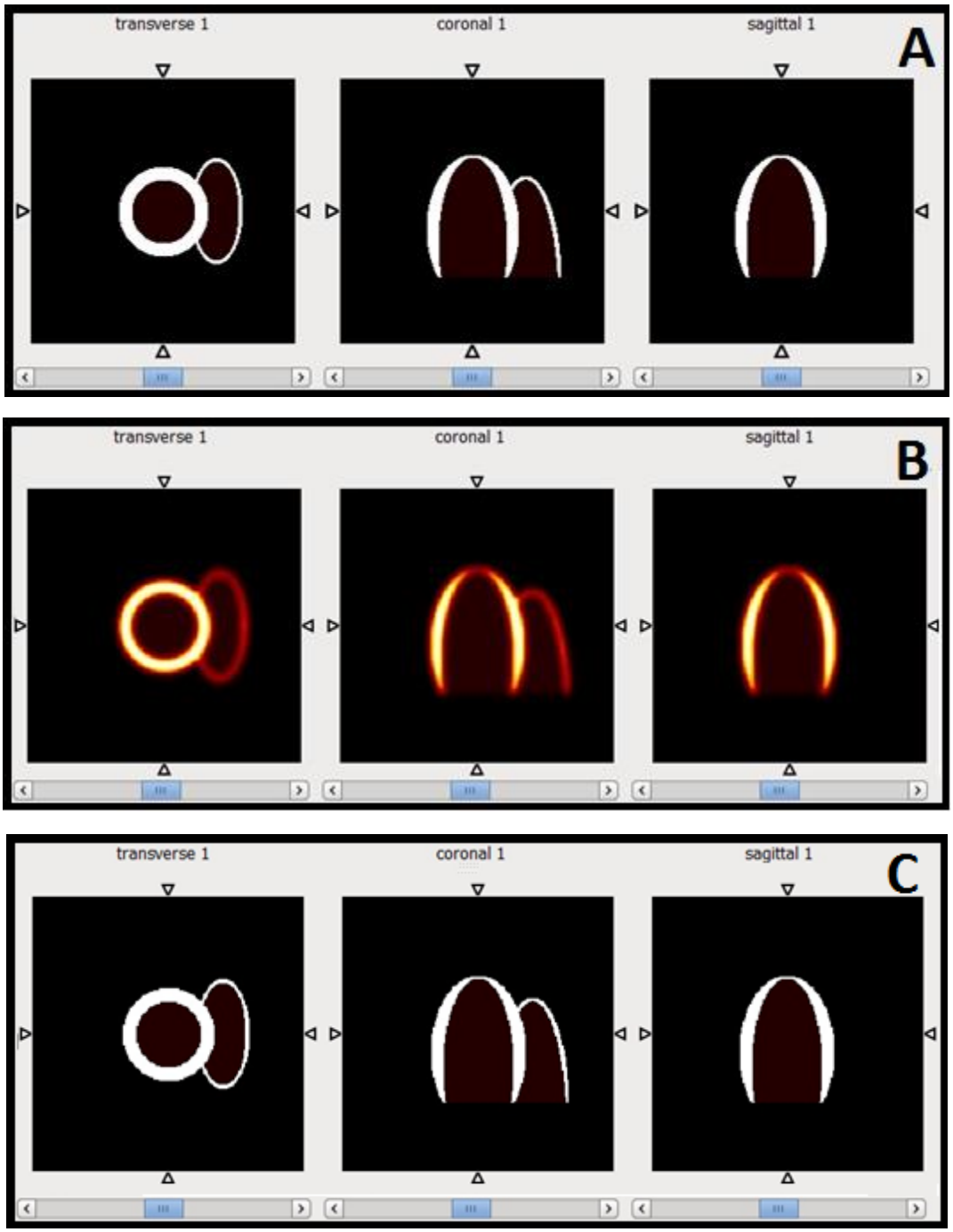


***Figure 5.40*** *- Original (A), Blurred (B) and recovered (C) simply convolved images following iY PVC*

Where it can be observed that the blur has been removed and the original activity distribution has been essentially recovered. Table 5.12 provides with more quantitative information regarding this process.

*Table 5.12 - iY PVC results following correction of ventricular heart model*

| ROI | Original activity | Mean Activity After Correction | PVC Error | Std |
|---|---|---|---|---|
| **LV (total)** | 1 | 1.03 | 0.03 | 0.03 |
| **Zone 10 (local)** | 1 | 1.03 | 0.03 | 0.03 |
| **BP** | 0.1 | 0.096 | 0.004 | 0.005 |

Where it can be observed that the mean activity has been restored to the original values, within the standard deviation, for voxel values of each relevant ROI.

However, it is worth mentioning that the number of iterations used to reach this correction was assigned with a typical value of 5, which leads to two questions: 1) has the algorithm stabilised prior to the 5$^{th}$ iteration (hence, allowing for the implementation of the correction routine using a lower number of iterations)? 2) has the algorithm stabilised from the 5$^{th}$ iteration onwards?

In order to answer these questions, a study regarding the PVC results following the implementation of the iY algorithm on the same model, using different numbers of iterations has been performed. Table 5.13 presents the results from this study.

*Table 5.13 - iY PVC - number of iterations study*

| Nr. of Iterations | Mean Activity Myocardium | Std. Dev. Myocardium | Mean Activity BP | Std. Dev. Myocardium |
|---|---|---|---|---|
| **1** | 0.7 | 0.3 | 0.11 | 0.01 |
| **2** | 0.99 | 0.01 | 0.11 | 0.01 |
| **3** | 0.997 | 0.003 | 0.103 | 0.003 |
| **4** | 0.999 | 0.001 | 0.1008 | 0.0009 |
| **5** | 0.9997 | 0.0004 | 0.1002 | 0.0003 |
| **10** | 0.9999 | 8e-4 | 0.1000 | 7e-4 |
| **20** | 0.999999 | 5e-05 | 0.100004 | 6e-06 |
| **30** | 0.999999 | 5e-05 | 0.100003 | 6e-06 |

From Table 5.13 it can be observed that in terms of total activity within each ROI, the mean activity in the myocardium and BP is essential the same as in the original case (1 and 0.1 for the myocardium and BP, respectively), within the calculated standard deviation. However, it is only at iteration number 5 that there appears to be a decrease in the initial estimate of the deviation of the PVE to below 0.1%, which can be interpreted to suggest that stabilisation in the number of subiterations has fully been acquired from iteration number 5, and in order to minimise the computational time associated with the PVC method, the number of subiterations should not be higher than this. Fig. 5.41 better illustrates the stabilisation of the mean activity within the LV's voxels from the 5$^{th}$ iteration onwards.

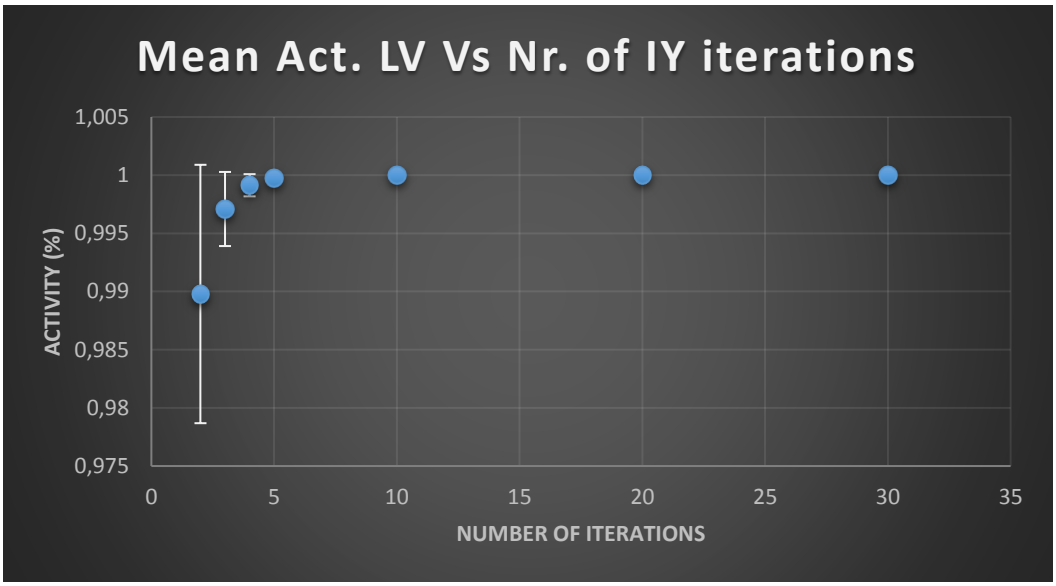


***Figure 5.41*** *- Depiction of the variation of the mean activity in the LV, in function of the number of iterations in the iY routine, with associated ROI standard deviation*

Another point that is worth noting is that while the myocardium is underestimated in the beginning of the routine, the BP is overestimated, which is consistent with the principles of PVE and PVC.

This completes the validation of the PVC routine, allowing for the utilization of this technique in a scenario where a simulated emission image with IVS would be recovered using a corresponding anatomical template that excludes this region. The errors due to this simplification would then be quantified. Therefore, in a similar set-up as in the GTM PVC quantification study, the total and local PVC error was measured in an image which PVC was incorrectly performed without taking into account an IVS of 9 mm. Similarly to the GTM case as well, the activity recovery was performed in images that went through a convolution, OSEM and FBP reconstruction routines, as shown in Fig. 5.42. An additional remark is that although the standard error was calculated in the same way as in the GTM study, in the current iY study the standard error produced by the correction of the simple convolution image was also incorporated. This was calculated by taking into account that one can have a standard deviation around the mean voxel intensity within a certain ROI, and a standard deviation of the mean voxel intensities in 100 images with different noise realisations, and that these two values follow a relationship which can be approximated to the following:

$$Std\_dev\_mean = Std\_dev\_ROI(\sqrt{(N)}) \qquad \textbf{Equation 5.1}$$

Where the $N$ is the number of voxels within the ROI. This approximation comes from the generalisation that the ROI is uniform and large enough. It is worth noting that this was simply not calculated for the convolution based results in the GTM study because the GTM does not provide with an image as an output, but rather mean ROI values.

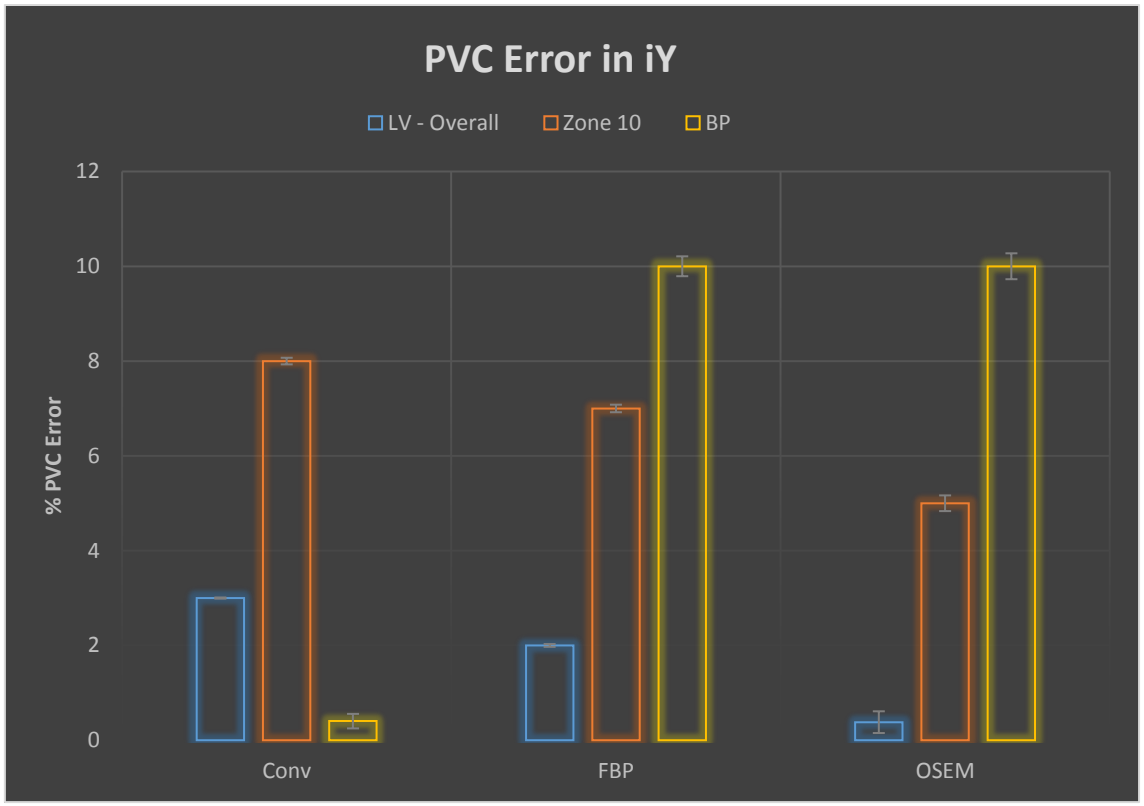


***Figure 5.42*** *- PVC Error following an iY activity recovery routine*

From observing the above Fig. 5.42, one can note two main aspects that differ from the GTM study. One is that the standard deviations were determined to be a lot smaller in the iY case, possibly due to the higher robustness associated with this activity recovery method. The other is the fact that the error in the activity in the BP was shown to be quite smaller in the iY case, differing significantly from the OSEM and FBP cases. One explanation is that the effect on not taking an IVS into account does not have a major impact on the BP's mean activity, given its large dimensions, and the apparent error observed in the FBP and OSEM cases is simply dues to the existence of noise.

Other than the two points noted above, the pattern of PVC is similar in both routines, suggesting a low bias on the overall LV wall, from not taking an IVS into account, while zone 10 is shown with having a consistent bias in both activity recovery exercises. This is in agreement with the previous studies, since the more significant local PVE is now reflected in an increased difficulty in recovering activity locally as well, in regions close to the IVS.

When assessing the visual aspect of the corrected images, the patterns illustrated in Fig. 5.43 become evident. In this figure, the final averaged simulated emission images are shown, before and after being submitted to an iY PVC routine.

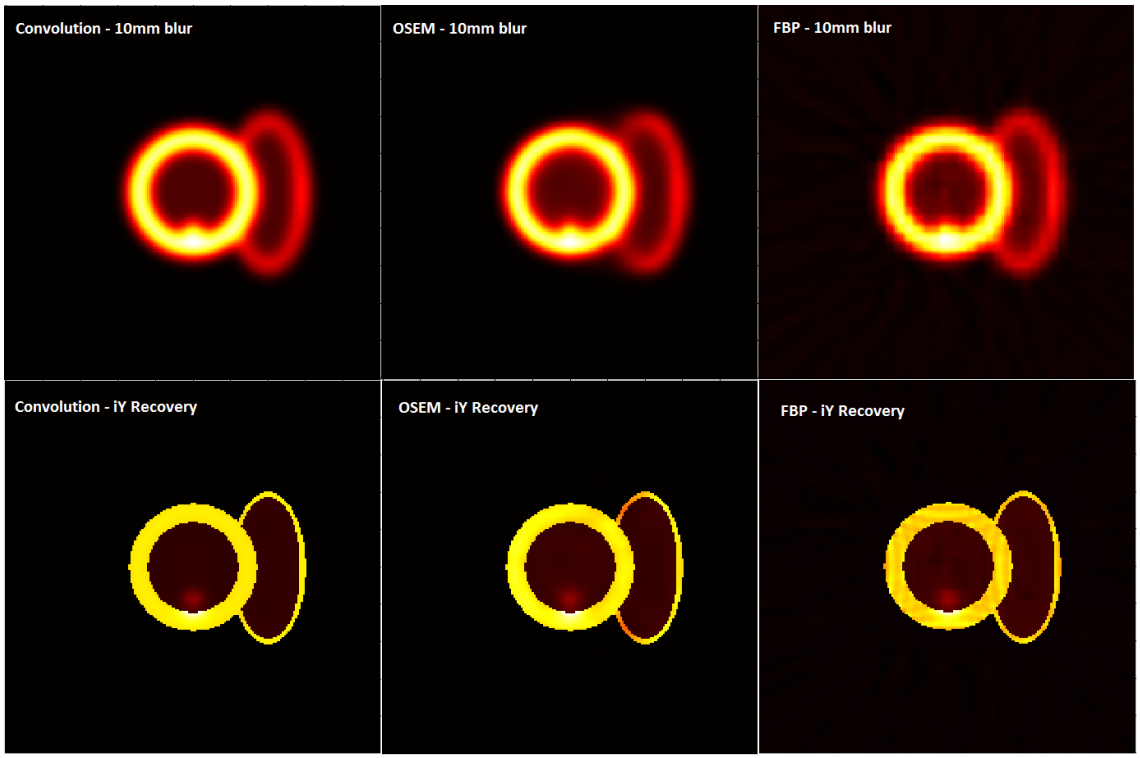


***Figure 5.43*** *- Short axis view of the iY PVC routine applied without taking IVS anatomical reference into account. Left) Convolution; Middle) OSEM with 100 averaged reconstructions; Right) FBP with 100 averaged reconstructions*

In Fig. 5.43 the lack of IVS in the anatomical template caused the PVC routine to overestimate the activity in the myocardium and BP, near the region where the IVS should be. This can be seen as a result of the original activity from the IVS being allocated to neighbouring regions, seeing that the anatomical template used for PVC did not contain such an IVS. In a clinical environment, this could potentially lead to confounding findings of various apparently high perfusion regions, or, even worse, could mask the location of hypo-perfused portions of the wall, as mentioned earlier, which could lead to further cardiac deterioration, due to lack of lesion awareness.

## 5.5.2. Application of PVC to real anatomical data

Following the evaluation of the importance of IVS' accountability in a PVC routine, and the determination that this accountability does indeed have a potentially significant (visual) local impact, it was decided that in order to improve the realistic nature of this study even further, the same set of PVC assessment checks would need to be implemented on real clinical data.

The goal was therefore to obtain cardiac anatomical images (either from high resolution CT or MR), delineate the LV, BP and IVS, and then calculate the percentage of error obtained from performing PVC routines with and without the IVS taken into account.

It was anticipated that the results obtained would shed some additional insight on whether it is indeed worth to include IVS in cardiac PVC techniques or not.

In order to allow for the implementation of this approach, an intermediate step had to be taken, with the goal of evaluating two available cardiac segmentation techniques, in terms of whether

these would be effective or not. The chosen technique would then theoretically be used to individualise a LV from a cardiac apparatus, as well as the BP and IVS within the LV cavity. Therefore, the capability of the segmentation method to provide with a successful delineation of the LV's myocardium and of the major IVS was the main criteria for the acceptance of the routine.

In order to carry out this exercise, each segmentation method was tested by means of segmenting a same pre-selected CTA data set. The description of the methods and their respective results are depicted in the following sub-sections.

### 5.5.2.1. Atlas based cardiac segmentation technique

This method corresponds to a fully automated segmentation technique for the delineation of the whole heart, as well as the great vessels, from 3D high resolution anatomical data, typically CTA and MRI. The method is based on a multi-atlas propagation segmentation approach that has previously proven successful in brain and cardiac segmentations (Zuluaga et al. 2013).

The method is based on a cross correlation metric, and selects the best atlases for propagation, allowing the refinement of the segmentation at each iteration of the propagation process. The method has been previously validated in multiple image modalities (Zuluaga et al. 2013).

Following the implementation of the segmentation routine on the selected anatomical cardiac data, the results shown in Fig. 5.44 were obtained.

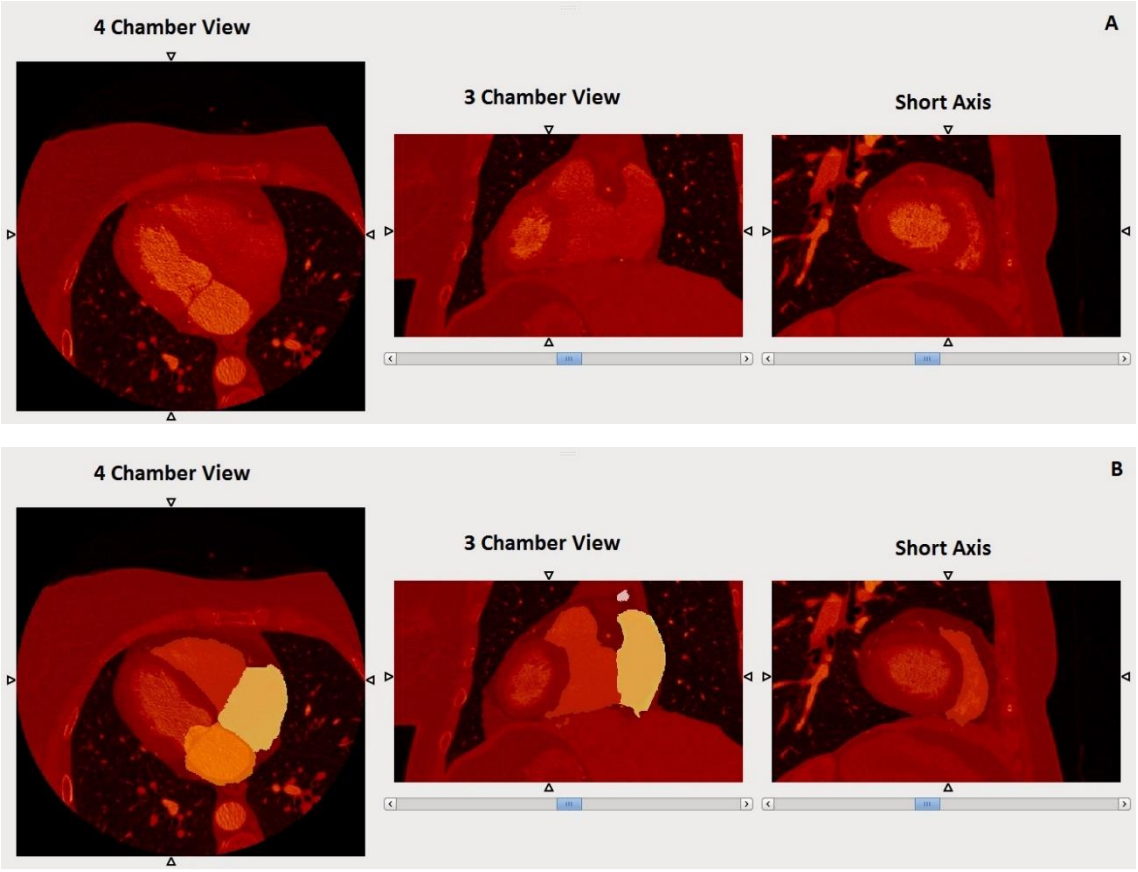


***Figure 5.44*** *- Atlas based cardiac segmentation technique's results, on selected CTA data (A –Original CTA image; B – Original CTA Image + Cardiac Segmentation)*

Where it is clear that the different cardiac apparatus' regions have been segmented and compartmentalised into different ROI's, which are relatively simple to work with. However, Fig. 5.44 also shows that although the method is successful at segmenting the main cardiac tissues, particularly, the LV and respective BP, it does not capture the characteristic irregularities of the LV's endocardium wall, which is mainly illustrated in the short axis view (axial). In fact, it is noticeable that the IVS are not included in this segmentation scheme, neither the PM nor the TC. This has been confirmed upon a thorough inspection of the segmentation results, in all imaging planes. These structures have not been included in the atlas, possibly due to the high variability associated with their location and geometry, across different individuals. This can be seen as a major drawback in utilising this method for the specific purposes of this study. However, it is worth noting that the relevance of this method should not be discarded, as this segmentation routine can provide with a good starting point for intraventricular segmentation, not to mention its usefulness in other cardiac applications, which do not require IVS delineation.

#### 5.5.2.2. Active Contour Based Segmentation Method

This method is based on the active contour technique proposed by Chan et al. (2001). The basic idea behind the algorithm is to evolve a parametric curve subjected to constraints defined from the image. In order to detect a profile in an image, a function representing the energy of the curve surrounding the profile is iteratively minimised.

The energy function is composed of two parts: one term controls the deformation of the curve (i.e. the derivative of the curve) while the other term determines the fitting of the curve to the profile in the image, "pushing" this curve to salient features of the image, like the edges.

The minimisation of the function can be obtained by using the associated Euler-Lagrange equation and solving it iteratively.

This method also allows for a fully automatic segmentation of the four heart chambers, ventricles, atria and great vessels from 3D CTA images.

Following the implementation of this routine on the same data that undergone the atlas-based segmentation, a summary of the results obtained is summarised in the form of the segmented LV and correspondent cavity, as per Fig. 5.45.

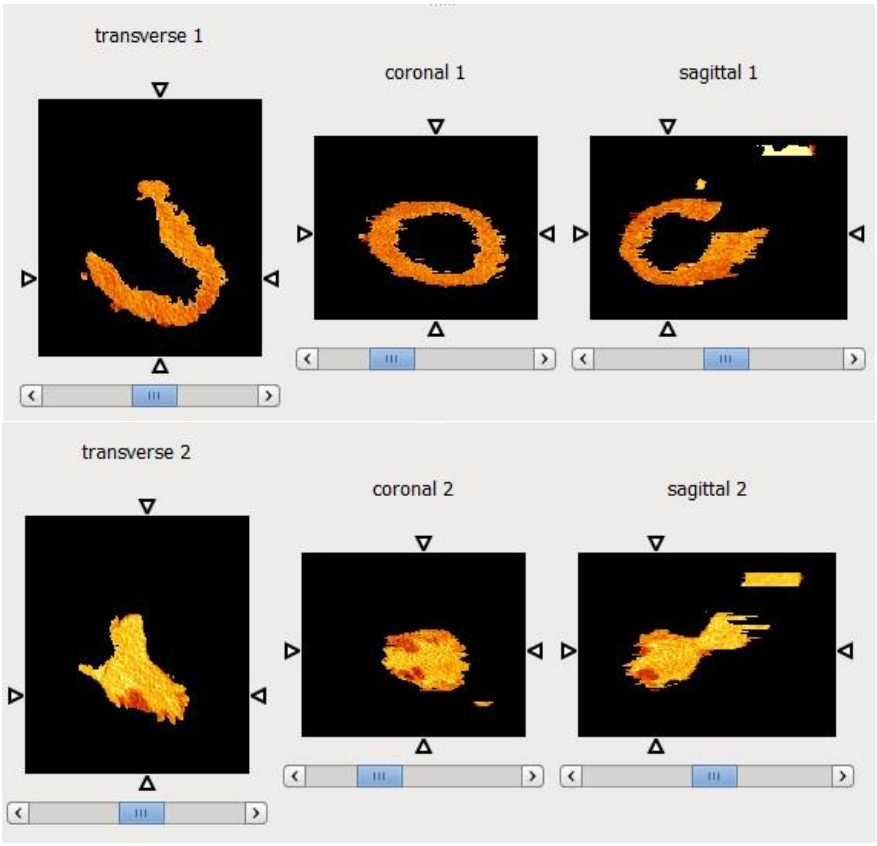


***Figure 5.45*** *- Results from segmenting the LV (top) and BP (bottom) of a selected CTA image, using the active contour segmentation technique*

Which shows that the method appears to capture more efficiently the natural irregularities of the LV wall. However, further inspection of the LV segmentation led to the discovery of the presence of a number of artefacts associated with the segmentation. In addition to the over-segmentation of the BP observed in Fig. 5.45, Figs. 5.46 and 5.47 depict the inclusion of a portion of the aorta in the LV ROI, on the same heart.

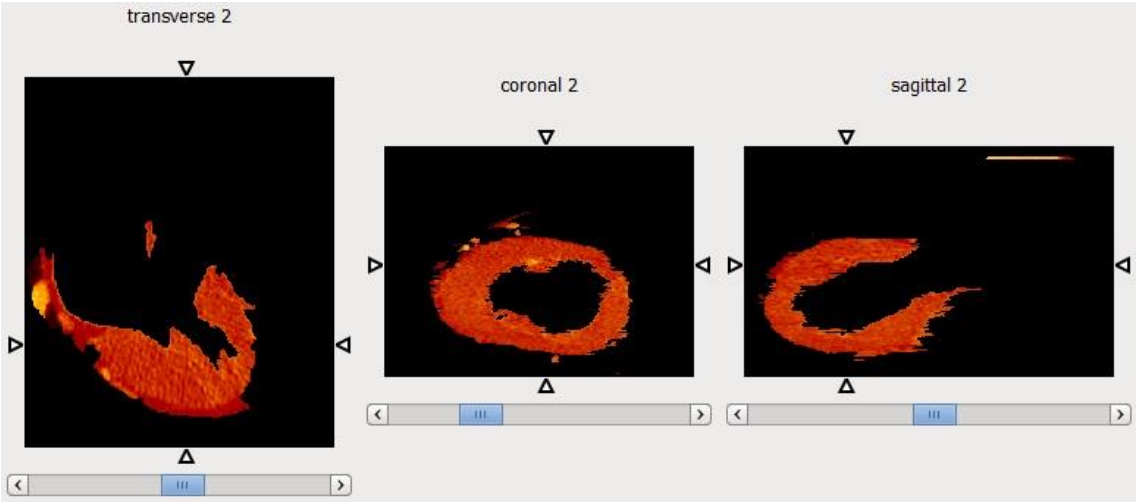


***Figure 5.46*** *- Results from LV segmentation with active contour technique - 2D inclusion of aorta in vertical long axis view*

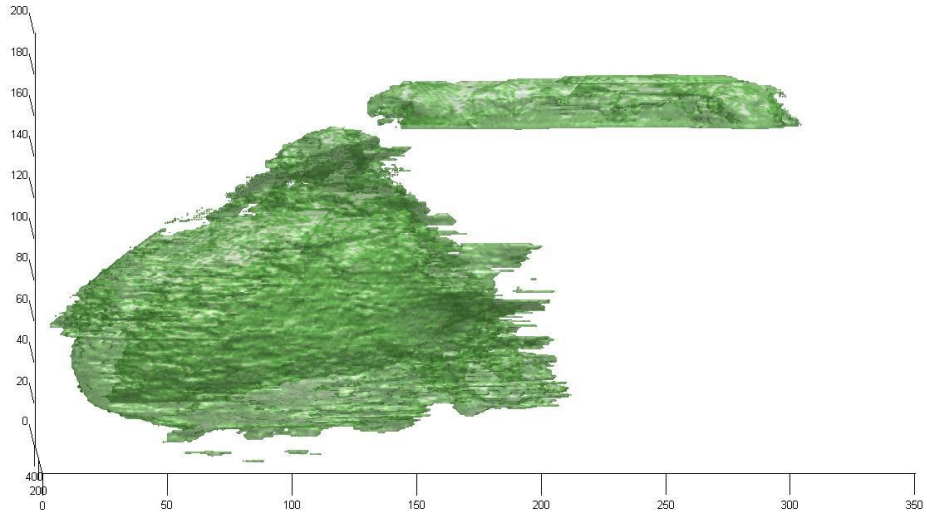


***Figure 5.47*** *- Results from LV segmentation with active contour technique - 3D inclusion of aorta*

This issue could be simply solved, in principle, with a number of pre-processing steps, consisting essentially a number of erosion steps, followed by an adequate number of dilations. This would also help in reducing the abnormal level of irregularities in the pericardium and endocardium surfaces.

Another relevant aspect of this segmentation scheme is that, similarly to the atlas-based method, PMs, which are an integrand part of the myocardium, were not included in the LV's segmentation. Instead, these structures were included in the BP, as depicted in Fig. 5.48, which shows the same heart used previously (*heart A*), and also Fig. 5.49, where the segmentation of a different heart is shown (*heart B*), for the purpose of better illustrating this issue.

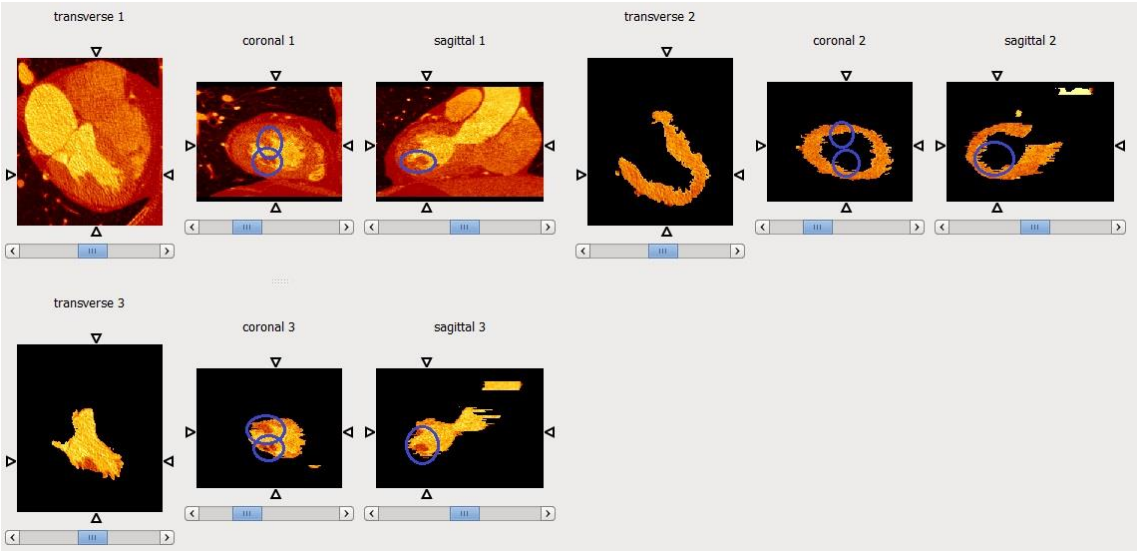


***Figure 5.48*** *- Depiction of IVS inclusion on BP's segmentation, in heart A*

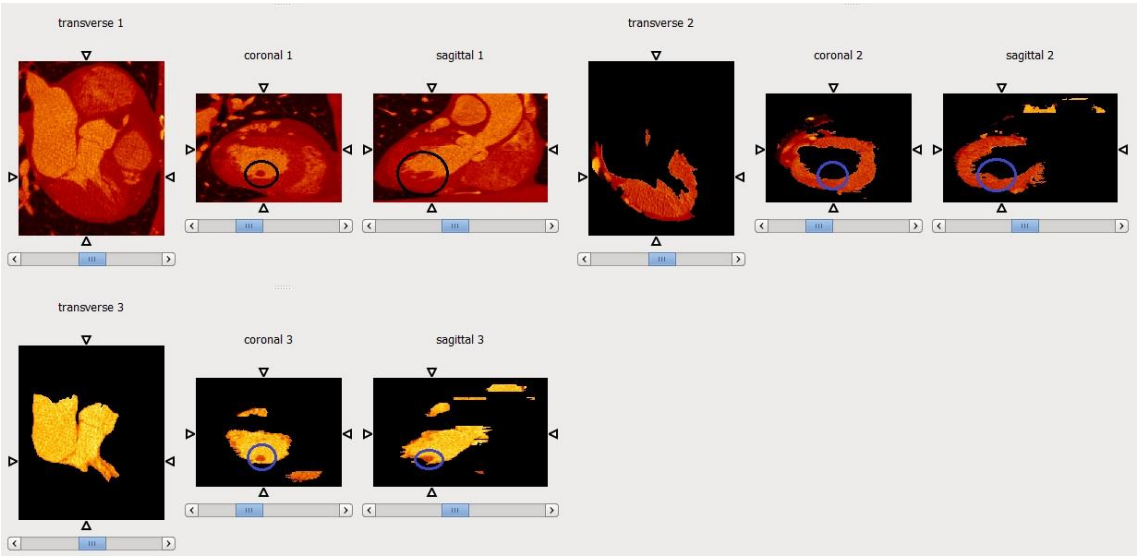


***Figure 5.49*** *- Depiction of IVS inclusion on BP's segmentation, in heart B*

However, moving down a few slices on the axial direction, it can be observed that the phenomenon of inclusion of IVS in the BP is only observable in the slices that contain the medial and apical regions of the PMs, where the PMs appear to hover within the LV cavity, being delineated together with the BP. On slices that capture the base of the PMs, these structures can be seen as being correctly assigned to the LV's ROI, most probably due to the fact that in these cases there is a physical continuity between the PMs and the LV. This can be evidenced in Fig. 5.50, representing a different axial slice from *heart B*.

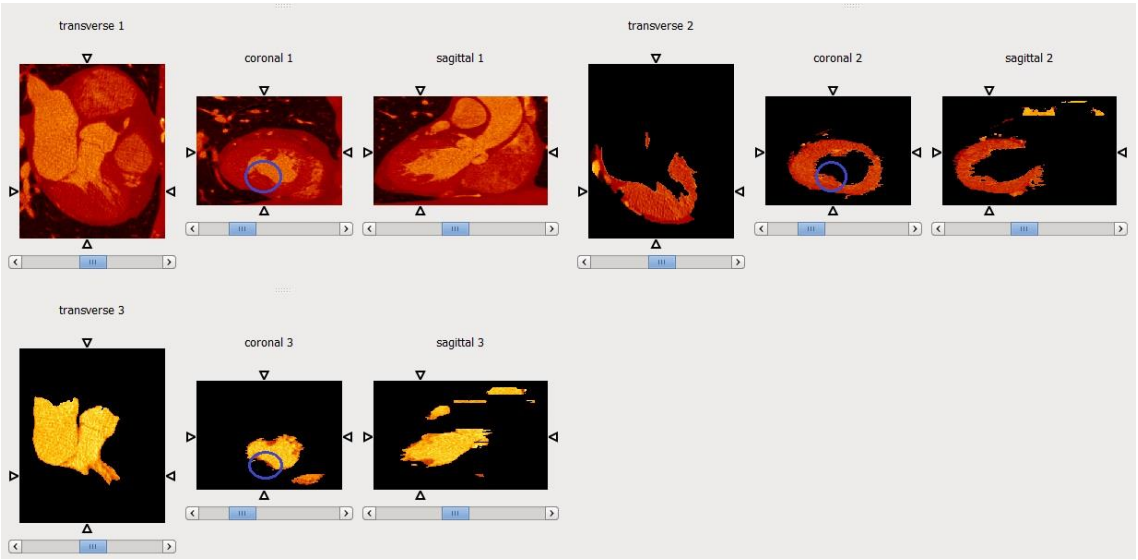


***Figure 5.50*** *- Depiction of inclusion of basal region of IVS in LV's segmentation, in heart B*

Therefore, although there is not a full delineation of the PM, the current segmentation method could still prove as a potentially useful initial step towards achieving a delineation of IVS.

However, in general terms, the level of sensitivity produced by this technique, in terms of the detection and incorporation of the IVS as an intrinsic part of the LV's myocardium is not sufficient, at least for the selected data and parameter set-up, as the majority of the volume of these internal structures has been incorrectly assigned to the BP.

Therefore, it can be concluded that this difficulty in individualising the IVS poses a significant issue in terms of utilising this method in the next steps of this study.

### 5.5.2.3. Overview of Available Cardiac Segmentation Methods

Following the obtainment and evaluation of the results produced from both of the available cardiac segmentation methodologies, comparison measures could be made in order to choose which method to choose from, if any.

Recalling the results obtained in the previous individual evaluations (sections **5.5.2.1** and **5.5.2.2**), although both cardiac tissue delineation methods presented to be satisfactory in segmenting structures like the LV, BP and pericardium, which is of great value in a number of clinical and medical research applications, these methods have not been designed to be used for the particular case of IVS delineation, hence they could not provide with a routine from which the IVS could be completely delineated and taken as independent structures.

Following the evaluations performed in the two previous sections, it was possible to observe that none of the segmentation methods appeared to satisfy the required criteria of providing with a set of structures that would allow to test the error obtained from not accounting for IVS in a PVC scheme, using real anatomical data.

A possible work around for this would be to use one of the previously described segmentation methods and then apply a second (manual) segmentation on the BP alone, in order to retrieve the IVS from the BP's content, using it as individual structures. When simulating the error produced in a PVC routine without consideration of IVS, the voxels corresponding to the region where the IVS would be in the BP would be filled with values equal to the mean intensity of the BP's ROI. The manual segmentation pipeline adopted would be partly intensity based, and partly manual based, and would comprise 3 steps only, to be applied in a case by case scenario: a) first, a threshold would have to be selected in a trial-and-error basis, and after an optimal value for this threshold was achieved, b) the segmentation would be applied and the outlier voxels would then go through a post-processing step in order to remove them adequately. This elimination of outliers could be performed simply by means of thresholding the undesired pixels, and further smearing the surrounding areas into the voxel in question by usage of *Matlab*'s in-built *roifill*() function, in a slice-by-slice basis (2D). c) The last step would comprise a manual adjustment of the segmented structure's borders, through visual checks in the coronal, sagittal and axial views.

However, there were three critical challenges to this approach: 1) a (partly) intensity based segmentation approach would in principle prove inefficient in segmenting the IVS from the BP, as the amount of "impurities" and different intensity-filled voxels in the BP was observed to be quite significant and spread throughout this ROI; 2) the alternative would be to use a fully manual segmentation routine, which on the other hand would require a high level of expertise and experience in terms of cardiac anatomy knowledge; 3) even if a segmentation routine would be successfully implemented, a local PVC assessment could not be easily performed since the division of the LV into 17 segments would be quite complex due to its irregular geometrical nature. Therefore, and mostly due to the previous points 2) and 3), a proper customised

segmentation approach was ultimately taken as unfeasible for the timeframe of the current project, which precluded the implementation of the PVC IVS assessment in real anatomical data.

# 6.*Summary, Conclusions and Future Prospects*

The current study had the objective of assessing the importance of internal ventricular structures in PVC procedures, applied to the cardiac apparatus. In order to test this, different levelled approaches were used, starting from evaluating the amount of blur produced by the structures upon simulated PET image reconstruction routines, rating this blur as significant or not, in comparison with the effect of the blood pool (BP), and culminating in PVC tests where the error produced by not taking these structures into account was quantified.

In general, the results obtained clearly showed that although the internal ventricular structures (IVS) do not pose a significant bias on the ventricle wall as a whole, their local effect, on the other hand, can be taken as quite significant, seeing that, at a local level, these IVS were observed as having the capability of producing more activity spillover than the BP.

Moreover, the fact that the overall number of internal left ventricular structures exerting their effect over the ventricular wall comprise a pair of papillary muscles and a plurality of trabeculae, further contributes to local activity biases in different ventricular regions, in emission images.

However, it is also worth noting that the previously presented results have been obtained from quantifications on the created ventricular heart model utilized in this study. Further enhancements to this approach would be the performance of similar PVE and PVC assessments studies on clinical anatomical data, and a final PVC routine applied to clinical functional and corresponding anatomical data.

The logical sequence of studies showed a good agreement, since the PVE assessment stage showed that the IVS did not seem to produce a significant blurring effect over the full extension of the LV wall – even when taking into account multiple IVS -, whilst having a very significant impact locally; and later on the PVC study showed that it was more difficult to recover the original activity distribution locally, which can be assigned to this enhanced local IVS effect.

This local effect was shown to be significant in both quantitative and qualitative terms in the simulated model. Quantitatively, the IVS seemed to produce a local effect which was taken as being more significant than the one produced by the BP, whereas as qualitatively the recovered images that did not take the IVS into account were shown to be locally biased by hyper-intensity artefacts on the LV wall – despite this effect being evident in the BP as well.

These effects should not be disregarded, as they can potentially lead to LV lesion masking, which could have important consequences in terms of patient management. The relevant question

that poses is whether it is worth accomplishing these imperfect PV compensation results, at the cost of obtaining these localised image processing artefacts.

Unfortunately, the possibility of using anatomical data for PVC purposes was proven to be arduous in this study, especially due to the inherent need for cardiac anatomy expertise in order to rigorously delineate the internal structures within the LV wall. Segmentation of the IVS was proven not to be possible with the automatic delineation methods available, as these were not designed to specifically capture the anatomy of IVS, and hence ended up not accomplishing this. Additionally, this unfeasibility ultimately prevented the achievement of a complementary study which would involve the PVC of functional data, with the aid of corresponding anatomical images, based on the successful obtainment of an IVS segmentation method. This would provide with two main additional realistic features, the possibility of studying a real cardiac activity distribution, as well as the reconstruction biases typical of proper clinical reconstruction routines.

Another important aspect to take into account is that the current ventricle model was designed in order to incorporate IVS with diameters up to 9 mm, whereas it has been reported that these structures could reach diameters of up to 10 mm in healthy scenarios, as well as more irregular geometries. This, added to the fact that cardiomyopathies such as LV hypertrophy may be accompanied with an out of the ordinary enlargement of the IVS, may contribute even further to the PVE produced by these structures, and hence add to the difficulty in recovering the original activity values in the relevant ROIs, following PVC routines. The fact that the activity was taken as uniform in the original objects also comprises source of deviation from a realistic setup, where the activity distribution of the tracer in the cardiac apparatus is expected to be heterogeneous and hard to model.

Therefore, and in light of all the activity homogeneity and geometrical simplification assumptions associated with the model utilized, the study showed no conclusive evidence that the internal ventricular structures should be disregarded from Partial Volume Correction-related segmentation procedures.

# 7.*Publications*

## 7.1. Oral Communication

- Sousa, M., Hutton, B., Thielemans, K. *Myocardial partial volume effect: the importance of intra-ventricular structures*. Oral Communication at: *I International Conference of Nuclear Medicine Technologies*; 2014 May 30-31; Lisbon, Portugal.

# 8.*References*


Abraham, A., Kass, M., Ruddy, T., deKemp, R., Lee, A., Ling, M., Ha, A., Beanlands, R., Chow, B. (2009). Right and left ventricular uptake with Rb-82 PET myocardial perfusion imaging: Markers of left main or 3 vessel disease. Journal of Nuclear Cardiology, 17(1):52-60.

Allender, S., Scarborough, P., Peto, V., Rayner, M., Leal, J., Luengo- Fernandez, R., Gray, A., (2008). European cardiovascular disease statistics. European Heart Network.

Ay, M.R., and Sarkar, S. (2007). Computed Tomography Based Attenuation Correction in PET/CT: Principles, Instrumentation, Protocols, Artifacts and Future Trends. Iranian J. Nucl. Med., 15(2):1–29.

Bengel, F. M., Higuchi, T., Javadi, M. S., & Lautamäki, R. (2009). Cardiac positron emission tomography. Journal of the American College of Cardiology, 54(1), 1–15.

Bogaert, J., Dymarkowski, S., Taylor, A.M. (2005) Clinical Cardiac MRI, Berlin: Springer

Brasse, D., Kinahan, P.E., Lartizien, C., Comtat, C., Casey, M. and Michel, C. (2005). Correction methods for random coincidences in fully 3D whole-body PET: impact on data and image quality. J Nucl Med, 46(5):859–67.

Budoff, M.J., Shinbane, J.S. (2006) Clinical CT Imaging, London: Springer

Burrell, S., & MacDonald, A. (2006). Artifacts and pitfalls in myocardial perfusion imaging, Journal of nuclear medicine technology, 34(4), 193–211.

Carli, M., Lipton, M., (2007) Cardiac PET and PET-CT Imaging, New York: Springer

Carney, J.P., Townsend, D.W., Rappoport, V., and Bendriem, B. (2006). Method for transforming CT images for attenuation correction in PET/CT imaging. Med Phys, 33(4):976–83.

Carson R E (1986). A maximum likelihood method for region-of-interest evaluation in emission tomography J. Comput. Assist. Tomogr. 10 654–63

Cerqueira, M. D. (2002). Standardized Myocardial Segmentation and Nomenclature for Tomographic Imaging of the Heart: A Statement for Healthcare Professionals From the Cardiac Imaging Committee of the Council on Clinical Cardiology of the American Heart Association. Circulation, 105(4), 539–542.

Chan, T., Vese, L. (2001). Active contours without edges. IEEE Transactions on Image Processing archive Vol. 10, 2, 266-277.

Chen CH, Muzic RF, Nelson AD. (1999). Simultaneous recovery of size and radioactivity concentration of small spheroids with PET data. J Nucl Med 1999; 40:118–30

Cherry, S.R., Sorenson, J.A. and Phelps, M.E. (2003). *Physics in Nuclear Medicine*. Saunders

Cochran, R. P., & Kunzelman, K. S. (1998). Effect of Papillary Muscle Position on Mitral Valve Function : Relationship to Homografts, 4975(98).

Da Silva, A.J., Tang, H.R., Wu, M.C. and Hasegawa, B.H. (1999). Absolute quantitation of myocardial activity in phantoms IEEE Trans. Nucl. Sci. 46 659–66

Dahlbom, M. and Hoffman, E. J. (1987). Problems in Signal-to-Noise Ratio for Attenuation Correction in High Resolution PET. IEEE Transactions on Nuclear Science, 34(1):288 –293. ISSN 0018-9499. doi: 10.1109/TNS.1987.4337350.

de Kemp, R.A. and Nahmias, C. (1994). Attenuation correction in PET using single photon transmission measurement. Med Phys, 21(6):771–8.

Di Carli, M.F., Lipton M.J. (2010). Cardiac PET and PET/CT Imaging. New York. Springer Science Business Media, LLC.

Dilsizian, V., Bacharach, S. L., Beanlands, R. S., Bergmann, S. R., Delbeke, D., Gropler, R. J., Travin, M. I. (2009). PET myocardial perfusion and metabolism clinical imaging. Journal of Nuclear Cardiology, 16(4), 651–651.

Dong, S., MacGregor, J., Crawley, A., McVeigh, E., Belenkie, I., Smith, E., Tyberg, J., Beyar, R. (1994). Left Ventricular Wall Thickness and Regional Systolic Function in Patients With Hypertrophic Cardiomyopathy. A Three-dimensional Tagged Magnetic Resonance Imaging Study. Circulation. 90(3): 1200–1209.

Du, Y., Madar, I., Stumpf, M., Rong, X., Fung, G. K., & Frey, E. (2013). Compensation for spill-in and spill-out partial volume effects in cardiac PET imaging. Journal of Nuclear Cardiology, 20(1), 84–98.

Dumouchel, T., Thorn, S., Kordos, M., DaSilva, J., Beanlands, R. S. B., & DeKemp, R. A. (2012). A three-dimensional model-based partial volume correction strategy for gated cardiac mouse PET imaging. Physics in Medicine and Biology, 57(13), 4309.

Erlandsson, K., Buvat, I., Pretorius, P. H., Thomas, B. a, & Hutton, B. F. (2012). A review of partial volume correction techniques for emission tomography and their applications in neurology, cardiology and oncology. Physics in medicine and biology, 57(21), R119–59.

Erlandsson, K. and Hutton, B.F. (2010). Partial volume correction in SPECT using anatomical information and iterative FBP Tsinghua Sci. Technol. 15 50–5.

Erlandsson, K., Thomas, B., Dickson, J. and Hutton, B.F. (2010). Evaluation of an OSEM-based PVC method for SPECT with clinical data. Nuclear Science Symp. and Medical Imaging Conf. pp 2686–90.

Erlandsson, K., Thomas, B.A., Dickson, J. and Hutton, B.F. (2011). Partial volume correction in SPECT reconstruction with OSEM. Nucl. Instrum. Methods A, 648 S85–8.

Erlandsson, K., Wong, A.T., van Heertum, R., Mann, J. J., and Parsey, R. V. (2006) An improved method for voxel-based partial volume correction in PET and SPECT NeuroImage 31 T84.

Ferreira, T., Rasband, W. (2012). ImageJ User Guide. [Online]. Available: http://rsbweb.nih.gov/ij/docs/guide/user-guide.pdf

Formiconi A R 1993 Least squares algorithm for region-of-interest evaluation in emission tomography IEEE Trans. Med. Imaging 12 90–100.

Frouin V, Comtat C, Reilhac A and GregoireMC 2002 Correction of partial-volume effect for PET striatal imaging: fast implementation and study of robustness J. Nucl. Med. 43 1715–26.

Gambhir S S 1990 Quantitation of the physical factors affecting the tracer kinetic modeling of cardiac positron emission tomography data, PhD Dissertation W4C G142q, University of California, Los Angeles, CA, USA (available).

GE Healthcare (2005). Discovery Dicom Conformance Statement for DICOM v3.0 (ID/Net v3.0). Direction 5161694-100, Rev 1.

Germano, G., (2006) Clinical Gated SPECT, 2nd Ed., New York: Blackwell Publishing.

Göktepe, S., Abilez, O. J., & Kuhl, E. (2010). A generic approach towards finite growth with examples of athlete's heart, cardiac dilation, and cardiac wall thickening. Journal of the Mechanics and Physics of Solids, 58(10), 1661–1680.

Grey, H. (ed.) (1918). Anatomy of the Human Body, 20th Ed., Philadelphia: Columbia Encyclopedia.

Groch, M. and Erwin, W (2001). Single-photon emission computed tomography in the year 2001: instrumentation and quality control. Journal of Nuclear Medicine Technology, vol. 29, no. 1, pp. 12–18.

Guillette, N., Sarrhini, O., Lecomte, R., & Bentourkia, M. (2010). Correction of partial volume effect in the projections in PET studies. IEEE Nuclear Science Symposuim & Medical Imaging Conference, 3541–3543.

Harrigan, C. J., Appelbaum, E., Maron, B. J., Buros, J. L., Gibson, C. M., Lesser, J. R., Maron, M. S. (2008). Significance of papillary muscle abnormalities identified by cardiovascular magnetic resonance in hypertrophic cardiomyopathy. The American journal of cardiology, 101(5), 668–73.

Hendel, R. C., Corbett, J. R., Cullom, S. J., DePuey, E. G., Garcia, E. V, & Bateman, T. M. (2002). The value and practice of attenuation correction for myocardial perfusion SPECT imaging: a joint position statement from the American Society of Nuclear Cardiology and the Society of Nuclear Medicine. Journal of Nuclear Cardiology : Official Publication of the American Society of Nuclear Cardiology, 9(1), 135–143.

Henriksen, E., Landelius, J., Wesslén, L., Arnell, H., Nyström-Rosander, C., Kangro, T., Friman, G. (1996). Echocardiographic right and left ventricular measurements in male elite endurance athletes. European heart journal, 17(7), 1121–8. .

Henze E, Huang S C, Ratib O, Hoffman E, Phelps ME and Schelbert H R. (1983) Measurements of regional tissue and blood-pool radiotracer concentrations from serial tomographic images of the heart J. Nucl. Med. 24 987–9

Ho, S. Y. (2009). Anatomy and myoarchitecture of the left ventricular wall in normal and in disease. European journal of echocardiography: the journal of the Working Group on Echocardiography of the European Society of Cardiology, 10(8), iii3–7.

Hoffman E. J., Huang, S. C. and Phelps, M. E. (1979) Quantitation in positron emission computed tomography: 1. Effect of object size J. Comput. Assist. Tomogr. 3 299–308.

Holly, T. a, Abbott, B. G., Al-Mallah, M., Calnon, D. a, Cohen, M. C., DiFilippo, F. P., Soman, P. (2010). Single photon-emission computed tomography. Journal of nuclear cardiology : official publication of the American Society of Nuclear Cardiology, 17(5), 941–73.

Hudson, H.M. and Larkin, R.S. (1994). Accelerated Image Reconstruction Using Ordered Subsets of Projection Data. *IEEE Transactions on Medical Imaging*, 13:601 –609. ISSN 0278-0062.

Huesman R H. (1984) A new fast algorithm for the evaluation of regions of interest and statistical uncertainty in computed tomography Phys. Med. Biol. 29 543–52.

Hunter, C., Hill, J., Ziadi, M., Beanlands, R., deKemp, R. (2015). Biodistribution and radiation dosimetry of (82)Rb at rest and during peak pharmacological stress in patients referred for myocardial perfusion imaging. Eur J Nucl Med Mol Imaging. 42(7):1032-42. doi: 10.1007/s00259-015-3028-3.

Hutton, B. F., & Osiecki, A. (1998). Correction of partial volume effects in myocardial SPECT. Journal of Nuclear Cardiology, 5(4), 402–413.

Iida, H., Eberl, S., Kim, K.-M., Tamura, Y., Ono, Y., Nakazawa, M., Watabe, H. (2008). Absolute quantitation of myocardial blood flow with (201)Tl and dynamic SPECT in canine: optimisation and validation of kinetic modelling. European journal of nuclear medicine and molecular imaging, 35(5), 896–905.

Iida, H., Kanno, I., Takahashi, a., Miura, S., Murakami, M., Takahashi, K., Tomura, N. (1988). Measurement of absolute myocardial blood flow with H215O and dynamic positron-emission tomography. Strategy for quantification in relation to the partial-volume effect [published erratum appears in Circulation 1988 Oct; 78(4):1078]. Circulation, 78(1), 104–115.

Iida, H., Rhodes, C. G., de Silva, R., Yamamoto, Y., Araujo, L. I., Maseri, a, & Jones, T. (1991). Myocardial tissue fraction--correction for partial volume effects and measure of tissue viability. Journal of Nuclear Medicine : Official Publication, Society of Nuclear Medicine, 32(11), 2169–75.

Kabanikhin, S. I. (2008). Definitions and examples of inverse and ill-posed problems. Journal of Inverse and Ill-posed Problems, 16(4), 317–357.

Kastis, G., Gaitanis, A., Fernandez, Y., Kontaxakis, G., Fokas, A. (2010). Evaluation of a Spline Reconstruction Technique: Comparison with FBP, MLEM and OSEM. IEEE Nuclear Science Symposium Conference Record, M18-284.

Keereman, V., Mollet, P., Berker, Y., Schulz, V. and Vandenberghe, S. (2012). Challenges and current methods for attenuation correction in pet/mr. Magnetic Resonance Materials in Physics, Biology and Medicine, 1–18.

Kinahan, P. E., & Fletcher, J. W. (2010). PET/CT Standardized Uptake Values (SUVs). Clinical Practice and Assessing Response to Therapy. Seminars in Ultrasound, CT, and MR, 31(6), 496–505.

Kobashi, a, Suwa, M., Ito, T., Otake, Y., Hirota, Y., & Kawamura, K. (1998). Solitary papillary muscle hypertrophy as a possible form of hypertrophic cardiomyopathy. Japanese circulation journal, 62(11), 811–6.

Kumar, K., Nagaraj, P., Kumar, V., Rao, D. (2010). Hypertrophic cardiomyopathy in 12 dogs (2004-2008): first report in India. Veterinarksi Arhiv 80 (4), 491-498.

Lancaster, J., Martinez, M. Using Mango. [Online].
Available: http://ric.uthscsa.edu/mango/downloads/Using_Mango.pdf

Lloyd-Jones, D., (2010). Heart Disease and Stroke Statistics–2010 Update. American Heart Association.

Loening, A., Gambhir, S. (2003). AMIDE: a free software tool for multimodality medical image analysis. Unpublished manuscript. [Online] Availablie:
http://web.stanford.edu/~loening/manuscripts/Loening_2003_AMIDE_postprint.pdf

Machac, J. (2005). Cardiac positron emission tomography imaging. Seminars in nuclear medicine, 35(1), 17–36.

Matela, N. (2008). *2D Iterative Image Reconstruction for a Dual Planar Detector for Positron Emission Mammography*. PhD thesis, Universidade de Lisboa.

Meltzer C C, Leal J P, Mayberg H S, Wagner H N Jr and Frost J J. (1990) Correction of PET data for partial volume effects in human cerebral cortex by MR imaging. J. Comput. Assist. Tomogr. 14 561–70

Monteiro, J.M. (2012). Implementation and Evaluation of Different Scaling Methods in Single Scatter Simulation for the Siemens BrainPET scanner. Master's thesis, University of Lisbon.

Moore, K.L., Agur, A.M.R., Dalley, A.F. (2010) Essential Clinical Anatomy, 4th Ed., Germany: the Point.

Muller-Gartner, H. (1992). Measurement of radiotracer concentration in brain gray matter using positron emission tomography: MRI-based correction for partial volume effects. J Cereb Blood Flow & Metab. 12:571-583.

Murphy, R. T., Thaman, R., Blanes, J. G., Ward, D., Sevdalis, E., Papra, E., Elliott, P. M. (2005). Natural history and familial characteristics of isolated left ventricular non-compaction. European Heart Journal, 26(2), 187–192. doi:10.1093/eurheartj/ehi025.

Muzic RF, Chen CH, Nelson AD. (1998) A method to correct for scatter, spillover, and partial volume effects in region of interest analysis in PET. IEEE Trans Med Imaging. 17:202–13.

Nekolla, S., Rischpler, C., Batrice, A., & Schwaiger, M. (2013). Cardiac PET/MRI. Current Cardiovascular Imaging Reports, 6(2), 158–168.

Nuyts, H., Maes, a, Vrolix, M., Schiepers, C., Schelbert, H., Kuhle, W., Mortelmans, L. (1996). Three-dimensional correction for spillover and recovery of myocardial PET images. Journal of nuclear medicine : official publication, Society of Nuclear Medicine, 37(5), 767–74.

Paans, A.M., Rosenqvist, G., Holte, s., Eriksson, L., Dahlbom, M., Bohm, C. (1989). Scatter fraction: measurement and correction. European Journal of Nuclear Medicine, Volume 15, Issue 11, pp 727-731.

Perry, K., Tann, M., Miller, M. (2008). Which reference tissue is best for semiquantitative determination of FDG activity? J Nucl Med, Volume 48, 49:425P.

Petitjean, C., & Dacher, J.-N. (2011). A review of segmentation methods in short axis cardiac MR images. Medical image analysis, 15(2), 169–84.

Pretorius, P., & King, M. (2008). Spillover compensation in the presence of respiratory motion embedded in SPECT perfusion data. Nuclear Science, IEEE Transactions on, 55(1), 537–542.

Pretorius, P. H., & King, M. (2009). Diminishing the impact of the partial volume effect in cardiac SPECT perfusion imaging. Medical Physics, 36(1), 105.

Rahmim, A., Tang, J., & Lodge, M. (2008). Analytic system matrix resolution modeling in PET: an application to Rb-82 cardiac imaging. Phys in Med, 53(21), 5947–5965.

Rahmim, A., Qi, J., & Sossi, V. (2013). Resolution modeling in PET imaging: theory, practice, benefits, and pitfalls. Medical physics, 40(6), 064301.

Ritt, P., Vija, H., Hornegger, J., & Kuwert, T. (2011). Absolute quantification in SPECT. European journal of nuclear medicine and molecular imaging, 38 Suppl 1, S69–77.

Rousset, OG, Ma, Y., & Evans, A. (1998). Correction for partial volume effects in PET: principle and validation. Journal of Nuclear Medicine, 39(5).

Rousset, Olivier, Rahmim, A., Alavi, A., & Zaidi, H. (2007). Partial Volume Correction Strategies in PET. PET Clinics, 2(2), 235–249.

Seiler, C., Jenni, R., Vassalli, G., Turina, M., & Hess, O. M. (1995). Left ventricular chamber dilatation in hypertrophic cardiomyopathy: related variables and prognosis in patients with medical and surgical therapy. British Heart Journal, 74(5), 508–516. doi:10.1136/hrt.74.5.508

Silva, A. Da, Tang, H., & Wong, K. (2001). Absolute quantification of regional myocardial uptake of 99mTc-sestamibi with SPECT: experimental validation in a porcine model. Journal of Nuclear Medicine, 42(5), 772–779.

Soret M, Koulibaly PM, Darcourt J, Hapdey S and Buvat I. (2003) Quantitative accuracy of dopaminergic neurotransmission imaging with (123)I SPECT J. Nucl. Med. 44 1184–93.

Soret, M., Bacharach, S. L., & Buvat, I. (2007). Partial-volume effect in PET tumor imaging. Journal of nuclear medicine : official publication, Society of Nuclear Medicine, 48(6), 932–45.

Spreeuwers, L. J., Bangma, S. J., Meerwaldt, R. J. H. W., Vonken, E. J., & Breeuwer, M. (2005). Detection of trabeculae and papillary muscles in cardiac MR images. Computers in Cardiology, 2005, 415–418.

Teräs, M., Tolvanen, T., Johansson, J., Williams, J., Knuuti, J. (2007). Performance of the new generation of whole-body PET/CT scanners: Discovery STE and Discovery VCT. Eur J Nucl Med Mol Imaging. 2007 Oct;34(10):1683-92. Epub 2007 Jul 28.

The MathWorks, Inc., (2013), MATLAB 2013b, Natick, Massachusetts, United States.

Thielemans, K., Tsoumpas, C., Mustafovic, S., Beisel, T., Aguiar, P., Dikaios, N., & Jacobson, M. W. (2012). STIR: software for tomographic image reconstruction release 2. Physics in medicine and biology, 57(4), 867–83.

Thomas, B.A., Erlandsson, K., Modat, M.,Thurfjell, L., Vandenberghe, R., Ourselin, S., and Hutton, B.F. (2011). The importance of appropriate partial volume correction for PET quantification in Alzheimer's disease Eur. J. Nucl. Med. Mol. Imaging 38 1104–19.

Thomas, B.A. (2012). Improved brain PET quantification using partial volume correction techniques. PhD thesis, UCL.

Vanzi E, De Cristofaro MT, Ramat S, Sotgia B, Mascalchi M and Formiconi A R. (2007) A direct ROI quantification method for inherent PVE correction: accuracy assessment in striatal SPECT measurements Eur. J. Nucl. Med. Mol. Imaging 34 1480–9.

Videen T O, Perlmutter J S,Mintun MA and Raichle ME. (1988) Regional correction of positron emission tomography data for the effects of cerebral atrophy J. Cereb. Blood Flow Metab. 8 662–70

Wassenaar, R., & DeKemp, R. (2006). Characterization of PET partial volume corrections for variable myocardial wall thicknesses. Nuclear Science, IEEE, 53(1), 175–180.

Weirich, C. and Herzog, H. (2012) Molecular Imaging in the Clinical Neurosciences, chapter: Instrumentation and Physical Principles, pages 1–22. Neuromethods.

Yang, J., Huang, S.-C., Mega, M., Lin, K. P., Toga, A. W., Small, G. W., & Phelps, M. E. (1996). Investigation of partial volume correction methods for brain FDG PET studies. Nuclear Science, IEEE Transactions on Nuclear Medicine, 43(6) - 3322:3327.

Yoshinaga, K., Klein, R., and Tamaki, N. (2010). Generator-produced rubidium-82 positron emission tomography myocardial perfusion imaging - From basic aspects to clinical applications. Journal of Cardiology (2010) 55, 163—173.

Zaidi, H. and Koraly, K.F. (2006). Quantitative Analysis in Nuclear Medicine Imaging. Boston, Springer.

Zaidi, H., and Montandon, M.L. (2007). Scatter Compensation Techniques in PET. PET Clin, 2:219–234.

Zuluaga, M., & Cardoso, M. (2013). Multi-atlas propagation whole heart segmentation from MRI and CTA using a local normalised correlation coefficient criterion. Functional Imaging and Modeling of the Heart.